

ISSN en trámite



Geofísica Internacional

Revista Trimestral Publicada por el Instituto de Geofísica de la
Universidad Nacional Autónoma de México



México

Volume 53 Number 1
January - March
2014

— Geofísica Internacional —

Dr. Arturo Iglesias Mendoza
Director of Instituto de Geofísica

Dra. Tereza Cavazos
President of Unión Geofísica Mexicana

Editor Chief

Dr. Servando De la Cruz-Reyna
Instituto de Geofísica, UNAM
sdelacrr@geofisica.unam.mx

Technical Editor

Mtra. Andrea Rostan Robledo
Instituto de Geofísica, UNAM
arostan@igeofisica.unam.mx

Editorial Board

Donald Bruce Dingwell
Earth and Environment
Ludwig Maximilian University of Munich,
Germany

Eric Desmond Barton
Departamento de Oceanografía
Instituto de Investigaciones Marinas, Spain

Jorge Clavero
Amawta Consultores, Chile

Gerhardt Jentzsch
Institut für Geowissenschaften
Friedrich-Schiller-Universität Jena, Germany

Peter Malischewsky
Institut für Geowissenschaften
Friedrich-Schiller-Universität Jena, Germany

François Michaud
Géosciences Azur
Université Pierre et Marie Curie, France

Olga Borisovna Popovicheva
Scobeltzine Institute of Nuclear Physics
Moscow State University, Rusia

Jaime Pous
Facultad de Geología
Universidad de Barcelona, Spain

Joaquín Rui
UA Science
University of Arizona, United States

Angelos Vourlidis
Solar Physics Branch
NASA Goddard Space Flight Center, United States

Théophile Ndougsa Mbarga
Department of Physics
University of Yaounde I, Cameroon

Associate Editors
José Agustín García Reynoso
Atmospheric Science Centro de Ciencias de la
Atmósfera UNAM, Mexico

Tereza Cavazos
Atmospheric Science
Departamento de Oceanografía Física CICESE,
Mexico

Dante Jaime Morán-Zenteno
Geochemistry
Instituto de Geología, UNAM, Mexico

Margarita López
Geochemistry
Instituto de Geología UNAM, Mexico

Avto Gogichaisvili
Geomagnetism And Paleomagnetism
Instituto de Geofísica UNAM, Mexico

Jaime Urrutia-Fucugauchi
Geomagnetism And Paleomagnetism
Instituto de Geofísica, UNAM, Mexico

Felipe I. Arreguín Cortés
Hydrology
Instituto Mexicano de Tecnología del Agua IMTA,
Mexico

William Lee Bandy
Marine Geology And Geophysics
Instituto de Geofísica UNAM, Mexico

Fabian García-Nocetti
Mathematical And Computational
Modeling
Instituto de Investigaciones en Matemáticas
Aplicadas y en Sistemas UNAM, Mexico

Graciela Herrera-Zamarrón
Mathematical Modeling
Instituto de Geofísica, UNAM, Mexico

Ismael Herrera Revilla
Mathematical And Computational
Modeling
Instituto de Geofísica UNAM, Mexico

Rene Chávez Segura
Near-Surface Geophysics
Instituto de Geofísica UNAM, Mexico

Juan García-Abdeslem
Near-Surface Geophysics
División de Ciencias de la Tierra CICESE, Mexico

Alec Torres-Freyermuth
Oceanography
Instituto de Ingeniería, UNAM, Mexico

Jorge Zavala Hidalgo
Oceanography
Centro de Ciencias de la Atmósfera UNAM,
Mexico

Shri Krishna Singh
Seismology
Instituto de Geofísica, UNAM, Mexico

Xyoli Pérez-Campos
Seismology
Servicio Sismológico Nacional, UNAM, Mexico

Blanca Mendoza Ortega
Space Physics
Centro de Ciencias de la Atmósfera, UNAM,
Mexico

Inez Staciari Batista
Space Physics
Pesquisador Senior Instituto Nacional de Pesquisas
Espaciais, Brazil

Roberto Carniel
Volcanology
Laboratorio di misure e trattamento dei segnali
DPIA - Università di Udine, Italy

Miguel Moctezuma-Flores
Satellite Geophysics
Facultad de Ingeniería, UNAM, Mexico

Assistance

Elizabeth Morales Hernández,
Management
eliedit@igeofisica.unam.mx



GEOFÍSICA INTERNACIONAL, Año 53, Vol. 53, Núm. 1, enero - marzo de 2014 es una publicación trimestral, editada por la Universidad Nacional Autónoma de México, Ciudad Universitaria, Alcaldía Coyoacán, C.P. 04150, Ciudad de México, a través del Instituto de Geofísica, Circuito de la Investigación Científica s/n, Ciudad Universitaria, Alcaldía Coyoacán, C.P. 04150, Ciudad de México, Tel. (55)56 22 41 15. URL: <http://revistagi.geofisica.unam.mx>, correo electrónico: revistagi@igeofisica.unam.mx. Editora responsable: Andrea Rostan Robledo. Certificado de Reserva de Derechos al uso Exclusivo del Título: 04-2022-081610251200-102, ISSN: en trámite, otorgados por el Instituto Nacional del Derecho de Autor (INDAUTOR). Responsable de la última actualización Saúl Armendáriz Sánchez, Editor Técnico. Fecha de la última modificación: 31 de diciembre 2013, Circuito de la Investigación Científica s/n, Ciudad Universitaria, Alcaldía Coyoacán, C.P. 04150, Ciudad de México.

El contenido de los artículos es responsabilidad de los autores y no refleja el punto de vista de los árbitros, del Editor o de la UNAM. Se autoriza la reproducción total o parcial de los textos siempre y cuando se cite la fuente completa y la dirección electrónica de la publicación.



Esta obra está bajo una Licencia Creative Commons Atribución-NoComercial-SinDerivadas 4.0 Internacional.

Contents

Delineation of the northern limit of the Congo Craton based on spectral analysis and 2.5D modeling of aeromagnetic data in the Akonolinga-Mbama area, Cameroon. Théophile Ndougsa-Mbarga, Donatus Yufenyiu Layu, Joseph Quentin Yene-Atangana, Charles Tabod Tabod	5
Active segment of the 12 November 2003 Mw 5.6 earthquake at Salsipuedes oceanic basin, Gulf of California, Mexico. Leobardo López-Pineda, Luis Quintanar Robles, Carlos Isidro Huerta López, Héctor Enrique Rodríguez Lozoya	17
Bottom topography, recent sedimentation and water volume of the Cerro Prieto Dam, NE Mexico. Vsevolod Yutsis, Konstantin Krivosheya Konstantin Krivosheya, Oleg Levchenko, Jens Lowag Jens Lowag, Héctor de León Gómez, Antonio Tamez Ponce	27
Use of Neural network to predict the peak ground accelerations and pseudo spectral accelerations for Mexican Inslab and Interplate Earthquakes. Adrián Pozos-Estrada, Roberto Gómez, H.P. Hong	39
Parallel numerical simulation of two-phase flow model in porous media using distributed and shared memory architectures. Luis Miguel de la Cruz, Daniel Monsivais	59
Reducing wind noise in seismic data using Non-negative Matrix Factorization: an application to Villarrica volcano, Chile. Giuseppe Cabras, Roberto Carniel, Joshua P. Jones, Minoru Takeo	77

Volcano-sedimentary stratigraphy in the Valsequillo Basin, Central Mexico inferred from electrical resistivity soundings.

Jaime Urrutia-Fucugauchi, Alfonso Trigo-Huesca, Eloísa Téllez-García, Ligia Pérez-Cruz, Fabiola Méndez-Rivero, Valsequillo Project Team

87

A very special Fractal: Gingko of Jena.

Peter G. Malischewsky

95

Delineation of the northern limit of the Congo Craton based on spectral analysis and 2.5D modeling of aeromagnetic data in the Akonolinga-Mbama area, Cameroon

Théophile Ndougsa-Mbarga*, Donatus Yufenyiu Layu*, Joseph Quentin Yene-Atangana and Charles Tabod Tabod

Received: January 24, 2011; accepted: March 19, 2013; published on line: December 11, 2013

Resumen

Se analizaron datos aeromagnéticos de la región Akonolinga-Mbama, con la finalidad de determinar la geología de subsuperficie de la zona. La interpretación de los datos disponibles, en forma de un mapa aeromagnético residual, muestra a esta vasta zona como magnéticamente tranquila, y las zonas complejas no se correlacionan con la geología de la superficie de la región.

Dentro de esta zona magnética tranquila una zona negativa alta, anómala, alargada y circular parece significar la intrusión de una roca plutónica en las formaciones metamórficas de la región. Se utilizaron el análisis espectral y la modelación dimensional de 2 y medio ($2\frac{1}{2}$ -D) para determinar la profundidad de los cuerpos que lo causaron y analizar las rocas de origen a lo largo de tres perfiles que cruzan las zonas en estudio. Se obtuvieron modelos de las intrusiones graníticas de diversas zonas, lo cual parece significar algunas fallas poco profundas a lo largo de las zonas de contacto. Esto nos permitió delimitar el margen norte del Congo Cratón, con lo cual distinguimos las formaciones cratónicas de la faja Panafricana plegada. Parte de la faja se ha extendido sobre la parte norte del Congo Cratón en Camerún.

Palabras clave: datos aeromagnéticos, anomalía residual, análisis espectral, modelación $2\frac{1}{2}$ -D, Panafricano, Congo Cratón, faltas, intrusión, Camerún.

Abstract

Aeromagnetic data of the Akonolinga-Mbama region are analyzed in order to elucidate the subsurface geology of the area. The available data in the form of a residual aeromagnetic map is interpreted as a vast magnetically quiet region, and complex zones which do not correlate with the surface geology of the region.

Within the magnetically quiet zone, a high negative circular elongated anomaly zone seems to represent an intrusion of a plutonic rock into the metamorphic formations of the region. Spectral analysis and two-and-a-half dimensional ($2\frac{1}{2}$ -D) modeling are used to estimate the depth of the causative bodies and determine the source rocks along three profiles crossing the suspected areas. Models from various zones of granitic intrusions are obtained, thereby proposing some shallow fault lines along zones of contact. This permits us to mark out the northern margin of the Congo Craton, thus enabling us to distinguish the cratonic formations from the Pan African fold belt. Part of the belt has been thrust over the northern portion of the Congo Craton in Cameroon.

Key words: aeromagnetic data, residual anomaly, spectral analysis, $2\frac{1}{2}$ -D modeling, Pan African, Congo Craton, faults, intrusion, Cameroon.

T. Ndougsa-Mbarga*
Department of Physics
Advanced Teacher's Training College
University of Yaoundé I
P.O. Box 47 Yaoundé Cameroon
Currently Director of Geology in the Ministry of Mines
Industry & Technological Development of Cameroon

D. Y. Layu*
C. T. Tabod
Department of Physics, Faculty of Science
University of Yaoundé I
P.O. Box 812, Yaoundé, Cameroon

*Corresponding authors: tndougsa@yahoo.fr
donlayu@hotmail.com

J.Q. Yene-Atangana
Department of Earth Sciences
Faculty of Science University of Yaoundé I
P.O. Box 812, Yaoundé, Cameroon

Introduction

The Akonolinga-Mbama region is situated in the central-south area of Cameroon (Central Africa) from latitude 3°15'N to 4°30'N and longitude 12° E to 13° E. This region, with an average altitude of 700 m, occupies the southern plateau of Cameroon and is made up of a monotonous landscape, mainly of gently undulating dome shaped hills of convex slopes and few rocky domes with concave slopes.

The area of study is part of the Precambrian of central and southern Cameroon which shows many geological features of different ages and varying petrographic characteristics (Tadjou *et al.*, 2009). In the Pan-African domain, geological studies (Toteu *et al.*, 2004) reveal that the region was formed during the Pan-African event in latest Proterozoic to earliest Palaeozoic by convergence and collision between the Congo Craton to the south and the Pan-African mobile belt to the north.

Gravity and audiomagnetotellurics studies by Collignon (1968), Ndougsa *et al.* (2003), Tadjou *et al.* (2009), Manguelle-Dicoum *et al.* (1992 & 1993), Mbom Abane (1997), and Meying *et al.* (2009) have shown that the limit of the Congo

Craton is characterized by a network of faults which traverse the region of study. The exact position of the limit of the Congo Craton has not yet been traced (Ndougsa *et al.*, 2002 & 2003). The objective of this study is to use the aeromagnetic data of the Akonolinga-Mbama region to investigate the major tectonic features and the subsurface geology, and to delimit the Northern limit of the Congo Craton.

Geology and tectonic setting

The area of study (Figure 1) is part of the Pan-African-Brazilian belt made of belts which were rejuvenated during the Pan-African orogeny about 550 Ma ago (Vicat, 1998; Djouka *et al.*, 2004; Toteu *et al.*, 2004). It is largely intruded by Neoproterozoic granitoids of Pan-African age emplaced from early stage of deformation to late uplift stage of the evolution of the Central African Fold Belt (CAFB). The region is in the southern portion of the Pan-African mobile domain that shares a boundary with the Congo Craton. It is composed of granite-gneissic rocks and those of the Precambrian intermediate formation (Vicat, 1998). This intermediate formation constitutes the Yaounde group formed of the Ayos-Mbalmayo-Bengbis series which dip to the north and merge

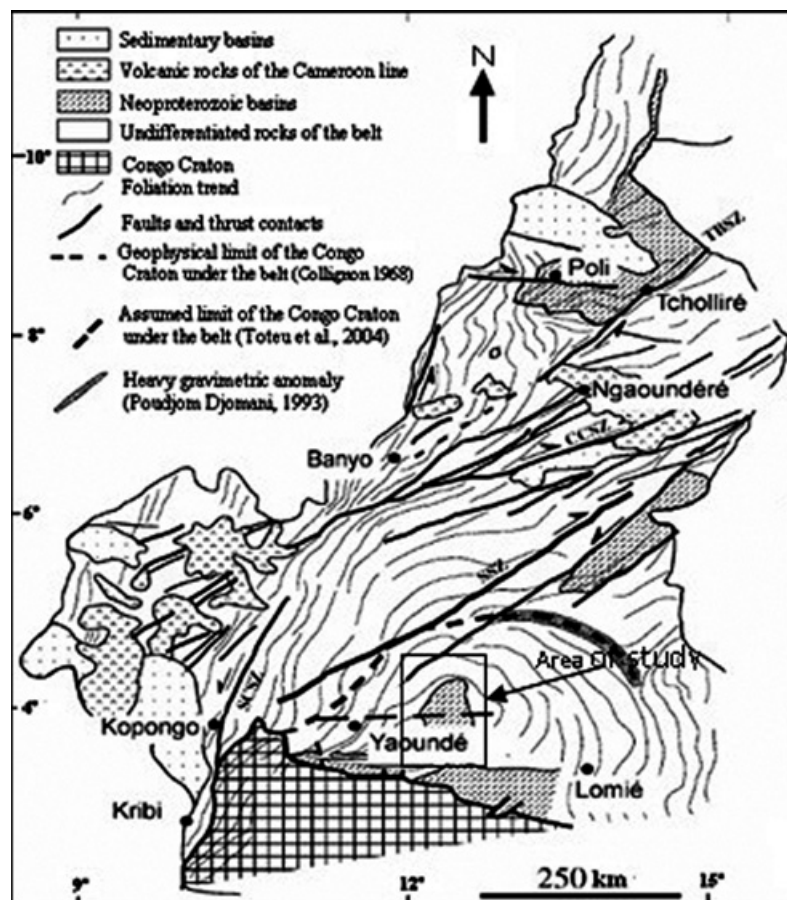


Figure 1. Geological map of Cameroon with foliation trends (After Toteu *et al.*, 2004).

with the Yaounde series without any lithological break. The Ayos-Mbalmayo-Bengbis series are mainly composed of schists and recrystallized quartzites. This schist and quartzite complex is a belt trending E-W, and covering about 1500 km (Vicat, 1998). The composition is made up of chlorite-schist, micaschist with or without garnet, gneisses and slates with numerous veins of quartzite. The Ayos-Mbalmayo-Bengbis series contains the same metasedimentary composition as the Yaoundé series, but metamorphosed and deformed at different structural levels (Olinga *et al.*, 2010).

The Yaoundé series is comprised of low to high grade garnet bearing schist, mica-schist, disthene, quartzite and gneisses metamorphosed under medium to high pressure metamorphism reaching the granulite facies (Toteu *et al.*, 2004; Vicat, 1998). The schists and gneisses are interpreted as neoproterozoic epicontinental deposits related either to an intracontinental distensive environment or a passive margin. Structurally, the Yaoundé series are made up of juxtaposed rock units which are interpreted as a large nappe that is thrust southward onto the Congo Craton (Toteu *et al.*, 2004). The Ayos-

Mbalmayo-Bengbis series (Figure 1) dips to the north and merges with the Yaoundé series without any major lithological break (Tadjou *et al.*, 2009).

The schist seems to have been formed from clay or limestone sediments. The mica-schist of this region is thought to have been formed on top of the chloride-schist. The primary minerals of the schist include muscovite, biotite, quartz and garnet, disthene, rutile and ilmenite as secondary minerals (Ndougsa *et al.*, 2003; Paterson *et al.*, 1976). The granites are of the calco-alkalinc and leucocratic type with heterogeneity in mineralogy.

As regards the tectonics, the region has a complex and uneven tectonic structure which is described to have resulted from orogenic movements of the Pan-African basement (Tadjou *et al.*, 2009). Although no clear evidence of the tectonic nature of the region is observed at the surface, it is worth noting the foliation and migmatization of the region (Figure 2). The arcuate foliation is regarded to have resulted from deformation of the underlying Congo Craton (Toteu *et al.*, 2004; Mvondo *et al.*, 2007). The schist and mica-schist are relatively folded (Olinga *et al.*, 2010).

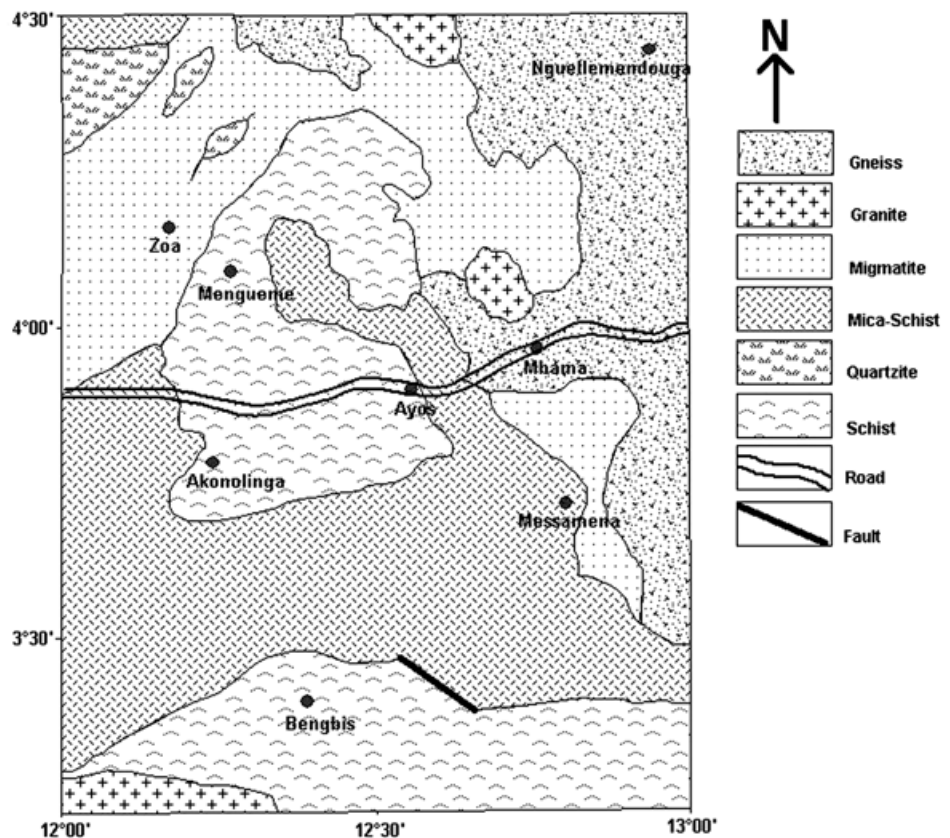


Figure 2. Simplified geological map of the area of study (Adapted from Nnange, 1991; Ndougsa *et al.*, 2003).

Aeromagnetic data

Origin of the data

The aeromagnetic data in Cameroon was collected over a total surface area of 168,365 km² (Paterson *et al.*, 1976). This area was divided into six regions of which the area of study is found within the Akonolinga region. The survey was carried out at a nominal terrain clearance of 235 m which was monitored by a radar altimeter with an accuracy of + 20 m. The line spacing of the flight was 750 m but the real distance rarely went above 1 km and the flight direction was N-S.

The data for this study was in the form of a residual magnetic anomaly map. This map was redigitized using the MAPINFO 7.5 package and was then gridded producing a new residual aeromagnetic anomaly map of contour interval 50 nT plotted (Figure 3) with the use of the Surfer 8.0 package.

Description of Residual Map

The residual aeromagnetic map (Figure 3) of this region is characterized by moderate amplitude anomalies ranging from about -300 to 200 nT and

trends in the E-W and NEE-SWW directions. Based on the features of the contours, the map can be partitioned in to a smooth magnetic (around and north of the latitude 4° N parallel) and the magnetically complex (south) anomaly zone.

We also observe zones of magnetic lows, some of which exist as circular negative elongated anomalies similar to those whose forms could indicate an induced magnetization on rocks with high magnetic susceptibility. The negative anomaly zones are along the migmatites and schist formations of the geological map.

Within the smooth magnetic anomaly zone, there exist a vast magnetically quiet zone which covers the granites, part of the schists, migmatite and gneiss of the region. Nnange (2000) suggests that the granites, schists and gneisses of the area are probably homogeneous in terms of magnetic character and were probably derived from rocks with little or no magnetite. The map shows in some areas (North) high positive anomalies. The gradient zones and traces of suspected rock intrusions within the region suggest the existence of suture zones within the Akonolinga-Mbama region (Figure 4).

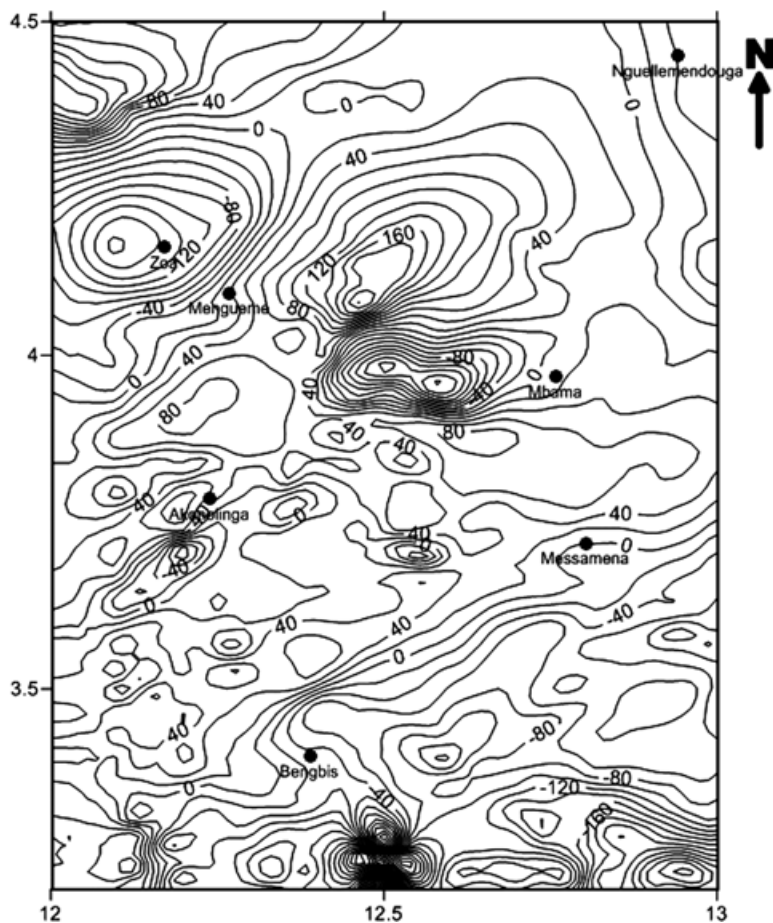
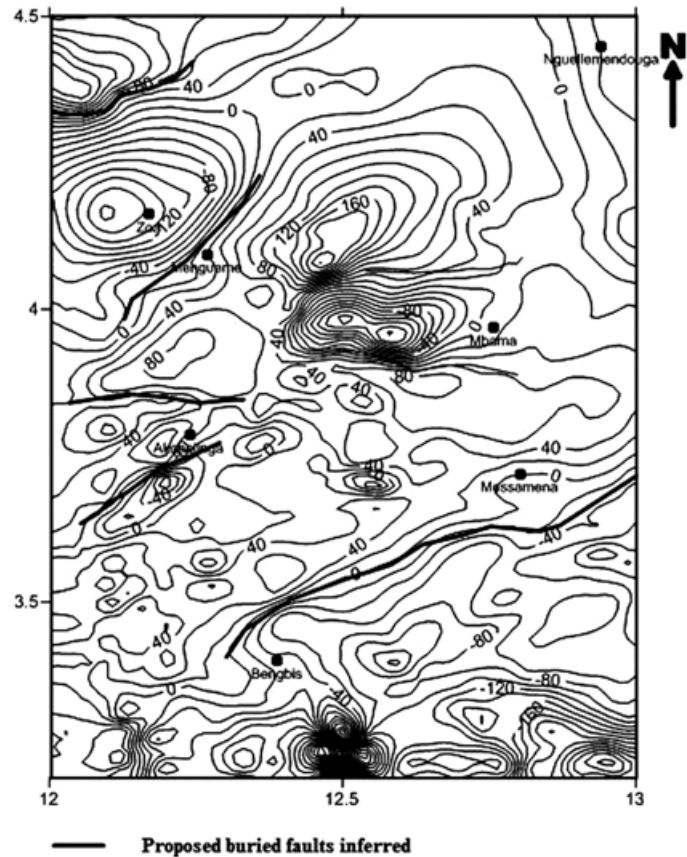


Figure 3. Aeromagnetic residual map of the study area.

Figure 4. Proposed buried faults inferred from the residual map.



Method of analysis

The data set for the quantitative analysis was obtained from profiles drawn across selected areas. The values of the anomalies and the distances obtained from the respective intersections of the profile and the contour lines constitute the principal input in the data modeling.

A spectral analysis code written based on the Spector & Grant (1970) and Bhattacharyya & Leu (1975) mathematical analyses, was used to determine the depth of the anomaly source. The mathematical analysis converts the data from the space to the frequency domain.

With the aid of a 2.5D modeling software mag2dc (Cooper, 2003), the chosen profiles were modeled to analyze the subsurface structure of the region. The mag2dc software uses the Talwani (1965) type algorithm to calculate the anomaly.

The value of the geomagnetic field, the inclination and the declination of the region, the bearing of the profile and the reference height (235 m) at which the data was collected are used as secondary input. In the present case, the inclination and declination angles of the ambient field were taken as -19.89° N and -5.88° E, respectively (2.5° N, 14° E) in the

center of the region at the date of January 1970 according to IGRF. The observed data curve and the theoretical one fitting is obtained by building a geometrical body. The depth from the spectral analysis, and physical parameters defined by the operator are compared to form a good fit. The physical parameter for this study is the magnetic susceptibility of the various rock types obtained from Telford *et al.* (1990) and Robert (1982). According to the geology of the area under study, the rocks found in the region were depicted to have their magnetic susceptibilities ranging from 0.0001 to 0.058 cgs. Hence the mean susceptibility of each of the rocks derived from the geology was used for the initialization of the modeling. Knowledge from previous geophysical analyses also served as bases for the modeling. The geometrical parameters such as the shape, the width and the height of the bodies were defined while modeling the profiles.

Results

Spectral Analysis

Three profiles P1, P2 and P3 were chosen and drawn on the residual aeromagnetic map (Figure 5). These profiles were drawn with a North-South orientation and traversing through the suspected area on the map.

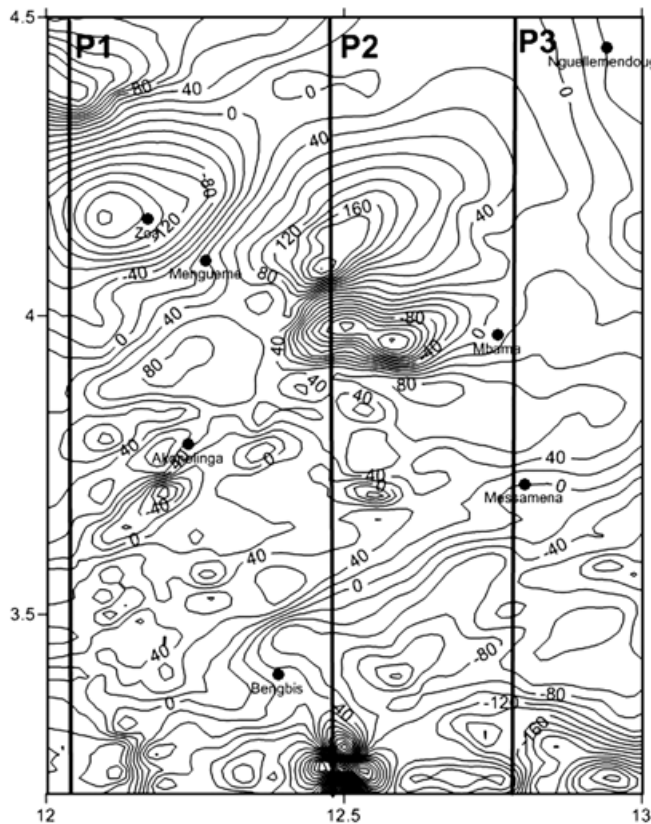


Figure 5. Aeromagnetic residual map with the modeled profiles.

Profile P1 covers a length of 111.0 km. It has its origin at latitude $3^{\circ}30' N$ and lies parallel on longitude $12^{\circ}6' E$ up to latitude $4^{\circ}30' N$. This profile runs through Zoa and Akonolinga, the nearest localities to the profile to the west. From the south, the profile cuts through the mica-schist, migmatite, quartzite and lastly the mica-schist at the north of the region.

Along the profile, we have a region of high negative anomalies that create a high gradient with the positive anomalies of the north. This gradient zone and other traced zones along the profile are the areas of interest.

Profile P2 runs from latitude $3^{\circ}15' N$ to $4^{\circ}30' N$. It lies parallel along longitude $12^{\circ}28'48'' E$ and covers a distance of 138.75 km. The profile cuts across with Bengbis and Mbang to the west, and Ayos and Ndele to the east. This profile passes through the schist, mica-schist, migmatite and gneissic formations from the south to the north of the geological map. At the south of the profile, there is a vast zone of negative anomalies which suggests a change in magnetic susceptibility. There is also a highly suspected zone of an intrusion about $4^{\circ} N$. The region with circular negative elongated anomalies creates a high gradient with the high positive anomaly zone towards the North. This profile is made up of two

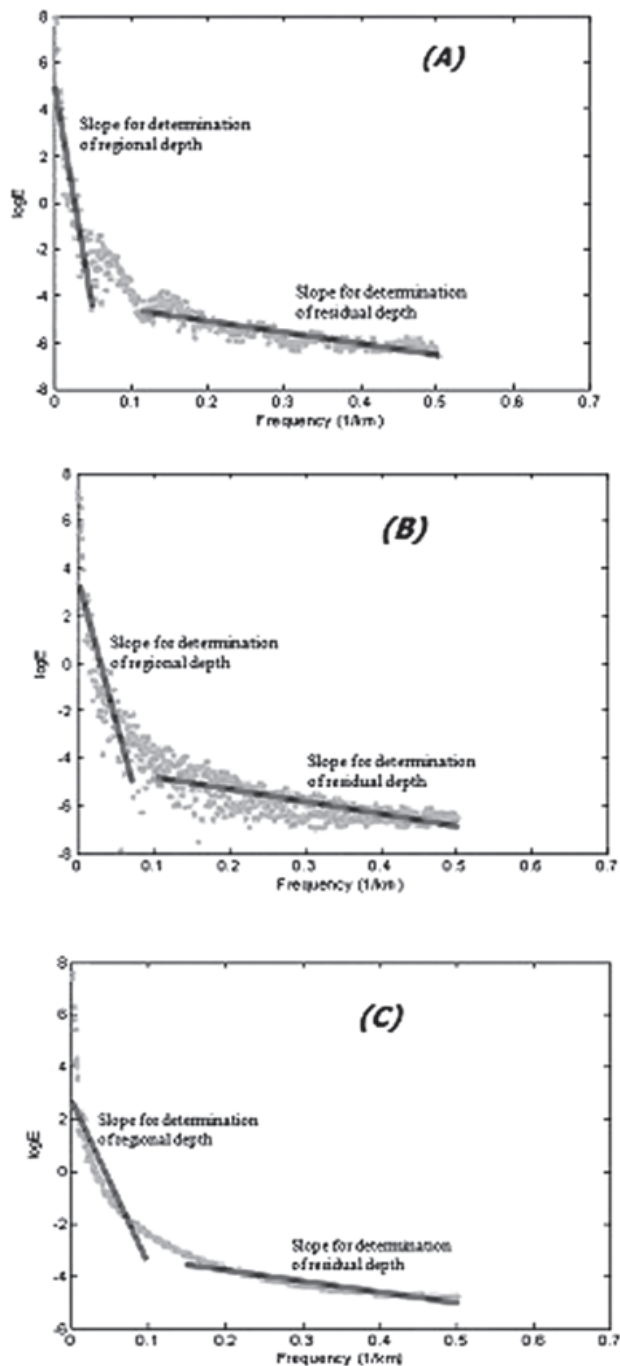
troughs and one crest with some having sharp peaks. This is as a result of varying magnetic character of the bodies along the profile.

The third profile lies along the parallel of longitude $12^{\circ}46'48'' E$ and runs from latitude $3^{\circ}15' N$ to $4^{\circ}30' N$. It covers a distance of 138.75 km and traverses between Messamena and Mbama. The profile cuts across the schist, mica-schist, migmatite and gneiss of the region. It runs from the negative anomaly zone in the South to the positive anomalies ranging from around Messamena up to the North.

The depths of the anomaly sources (Table 1) were calculated from plots of the log of the energy spectrum versus the wave number of the residual anomalies (Figure 6). The depths obtained from the slope of the curve represent the average depth of the top of the anomaly sources. The calculation of the error for the depths was also included in the computer code. The mean least square method used, integrates the fact that the error should not be more than 10% of the depth calculated (Nrange *et al.*, 2000). The regional depths represent the far away or deeper sources which are considered as anomaly sources of long wavelength. The residual anomaly depths serve as one of the constraints for the modeling that follows.

Table 1. Depths from spectral analysis.

Profile	P1	P2	P3
Residual depth (km)	0.38 ± 0.04	0.44 ± 0.04	0.31 ± 0.03
Regional depth (km)	17.72 ± 1.6	11.45 ± 1.15	7.36 ± 0.07

**Figure 6.** Spectral analysis of the profiles from the aeromagnetic map: (A) profile P1 ; (B) profile P2 ; (C) profile P3.**Table 2.** Magnetic properties of different rock types.

Rock type	Susceptibility (cgs unit)
Granite	2×10^{-3}
Schist	1.2×10^{-3}
Gneiss	1.3×10^{-3}
Quartzite	3.5×10^{-3}

2.5 D Modeling

The various profiles consist of troughs and crests. These profiles correspond to the models in figures 7, 8 and 9 respectively. The models of these profiles consist of various bodies which are responsible for the observed anomalies along the profile. The models consist of the quartzite, gneiss, schist and the granite formations which lie beneath the rock formations described by the geology. From the three models, we observe the plutonic intrusions in a region which is actually known as a highly metamorphic zone.

In regard to profile P1, the positive and negative anomalies at the north of the anomaly map are due to the quartzite rock mass whose formation is probably from the metamorphism of sandstones. These positive and negative anomalies are probably because the body can be considered as a dipole. There is also the gneiss formation which is found under the migmatite of the Zoa locality. The model is constituted of different rock units that are emplaced according to the anomaly of the area. At the south of the profile, we have the schist, gneiss and the granitic formations which are responsible for the negative anomalies within the complex region around latitudes $3^{\circ}30' N$, $3^{\circ}39' N$ and $3^{\circ}45' N$ respectively. As stated by Paterson *et al.* (1976) the schists are found beneath the mica-schist although the results from the model do not clearly differentiate if the schists are of the chlorite schist or not. Lastly, there is the granite that separates the two gneissic formations hence metamorphic-plutonic contacts. We have the granite-gneiss contacts. These contacts are found about 47 km and 53 km respectively from the southern edge of the profile. The granite formation is probably a result of the uprising

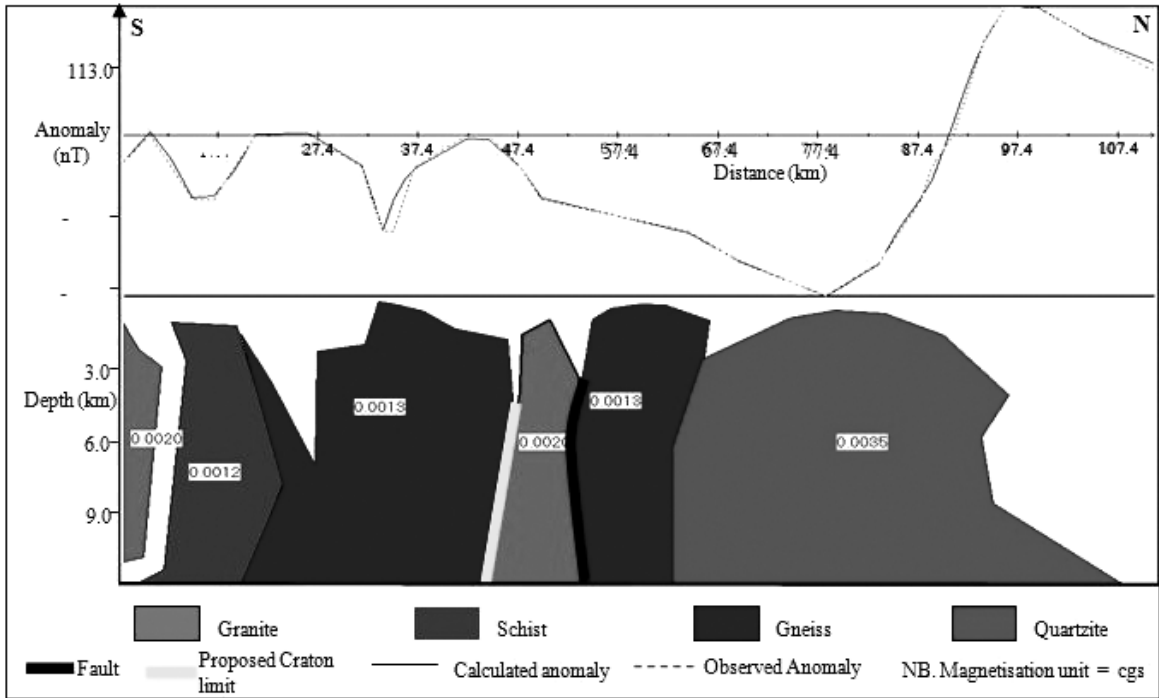


Figure 7. Profile P1 and model.

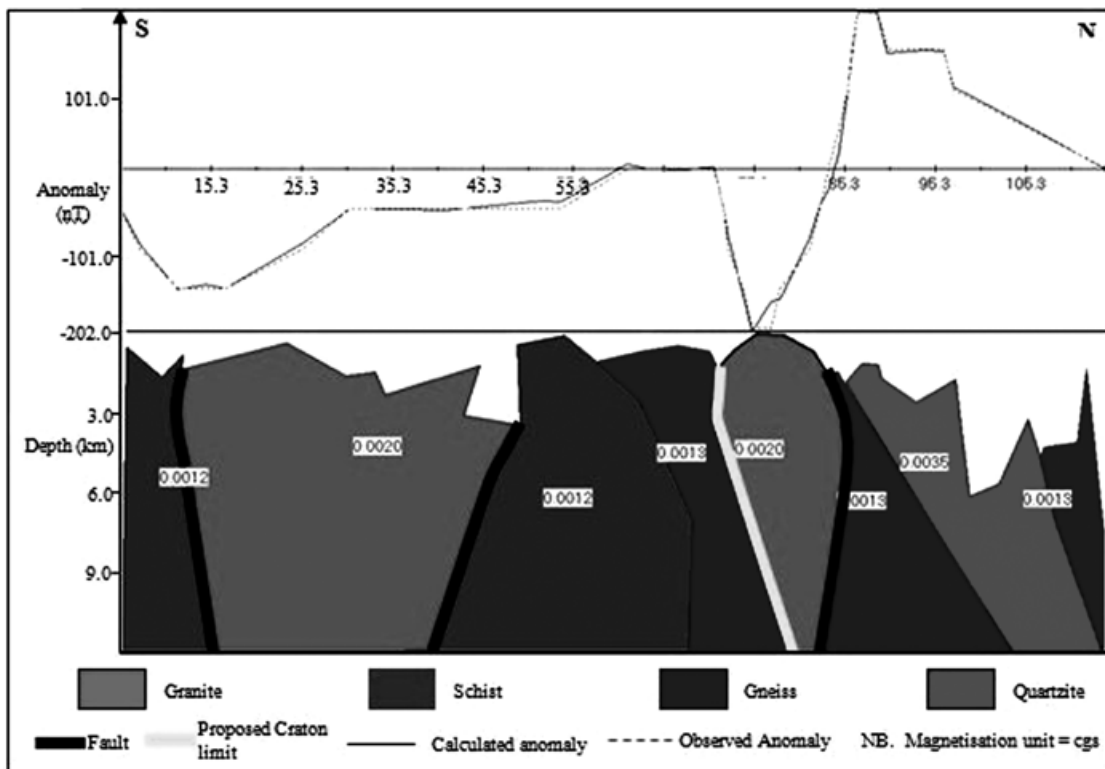


Figure 8. Profile P2 and model.

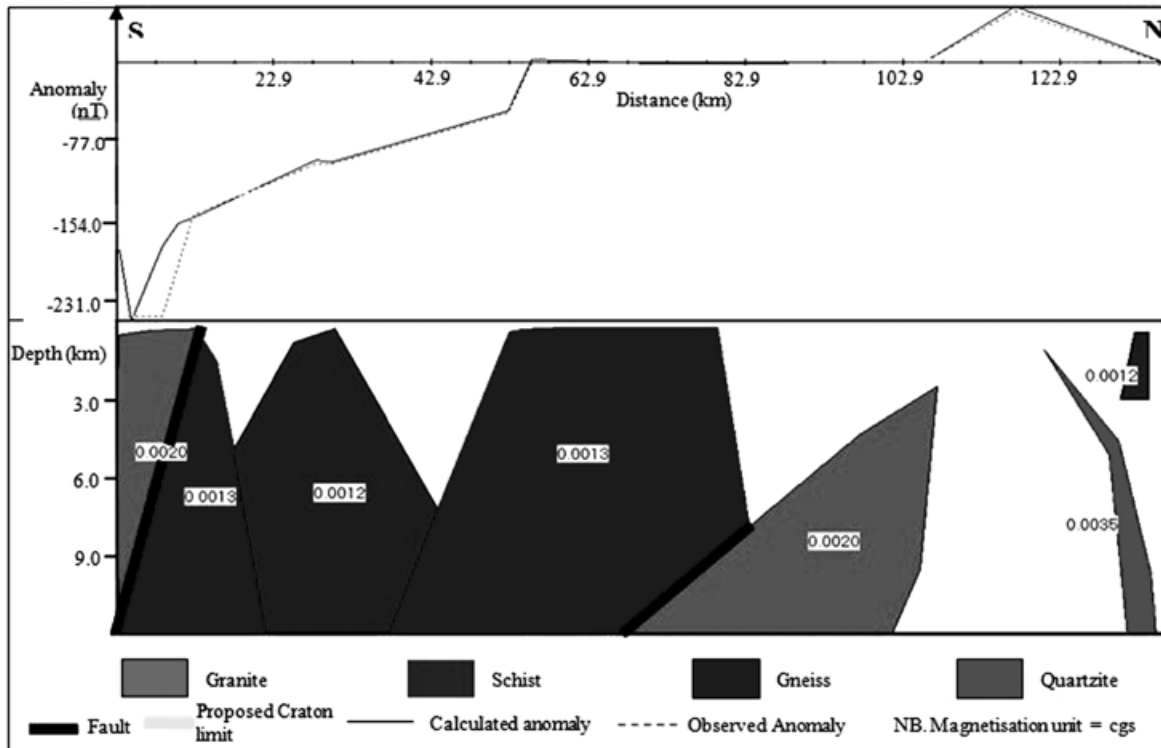


Figure 9. Profile P3 and model.

of magma along a zone of fissure resulting to a granitic intrusion. The magma probably originated from a magma chamber of which the fissure could have extended hence creating a passage for the magma. These contact zones represent buried faults. They are located between the Mengueme and Akonolinga localities. These are similar to the results obtained from the study of gravity data by Ndougsa *et al.* (2003) where faults were located along the Mengueme-Akonolinga axis.

The model of profile P2 (Figure 7) is made up of schist, gneiss, and quartzite and granite rock formations. Many are all in the interior of the crust with none reaching the surface as indicated from the spectral analysis. Along the model, we have two granite intrusions. These intrusions probably resulted from the crystallization of magma rising through the zones of weakness that must have extended up to a magma chamber deep in the lithosphere where the temperature and pressure allow the rock to exist in the molten form.

From the anomaly map, the granite formations are located along zones of negative anomalies along the profile. This includes the circular elongated negative anomalies that lie on the parallel of latitude 4° N which from the model represent a granite intrusion. This intrusion is in between two gneissic formations while the other

granite intrusion found at the south is in between the schist formations. The schists and gneisses are metamorphic rocks that were formed under different temperature and pressure conditions. The granite-gneiss contacts are located between Mengueme and Ayos and they represent zones of weakness, hence proposing faults within the regions. The granite-schist contacts also represent faults and are located on the north and south of Bengbis. These faults are shallow faults in the crust.

Profile P3's model (Figure 8) is characterized by eight bodies representing different rock formations based on their structural and physical properties. This comprises metamorphic rocks; schist, gneiss and quartzite, and a large granitic rock. The negative anomaly zone at the south of the profile is as a result of the schist, gneiss and quartzite formations. The schist is sandwiched by two gneiss rock masses. Along the profile where there is the magnetic quiet zone, we have a large mass of gneissic formation which lies beneath. This gneiss shares a boundary with the granite rock mass. This gneiss-granite contact represents a fault along the profile and it is around the parallel of latitude 4° N. This contact is situated just above the Mbama locality located on the geological map. To the north of the granite formation, there exist a quartzite and a schist rock masses.

The white patches on the three models represent undifferentiated rock units which are not the cause of the observed anomalies. They are rock units with no magnetic character.

Discussion

Forward modeling of magnetic data can have many models developed from the profiles. In order to obtain a model that reflects the subsurface structure, one has to consider certain parameters that would limit this uncertainty. As part of the constrains, the spectral analysis has been used to determine the average depths of the top of the anomaly sources. It is observed that the depths vary between 300 m and 450 m from the surface of the earth.

The three profiles drawn parallel to each other and their respective models, put to evidence a series of metamorphic and plutonic rocks. The granite formations of the profile P1 model (Figure 7, about 50 km from the southern edge), profile P2 model (Figure 8, about 75.3 km from the southern edge) and profile P3 model (Figure 9, about 95 km from the southern edge) both lie almost along the parallel of latitude 4° N. This is within the transition zone between the Congo Craton and the Pan African domain. The granitic formations probably resulted from the uprise of

magma through the contact zone between the Pan-African and cratonic domains, thus keeping the Pan African domain to the north and the Congo Craton to the south. Therefore tracing out the south contacts of these granitic formations (Figure 10) indicate the northern margin of the Congo Craton. Hence with respect to this limit we have the northern limit of the Congo Craton traced out on the geological map (Figure 11). The present results are in accordance with those put in evidence by Meying *et al.* (2009) in the Mbama, where a deep seated fault has been identified by the AMT analysis using the combination of Bostick and classical approaches (Meying *et al.*, 2009; Ndougsa *et al.*, 2011). In the regional scale, the structural facts identified by the study are in accordance with the results obtained by Ndougsa *et al.* (2002 & 2003) in the interpretation of gravity data, and the audiomagnetotelluric 1D linearized inversion & 2D forward modeling (Ndougsa *et al.*, 2011).

Conclusion

The purpose of this study was the correlation of the magnetic data with the surface geology and the tectonics, and to determine the subsurface geology of the Akonolinga-Mbama region. In this regard, the qualitative analysis of the vast varying anomalies of the region highlighted that the

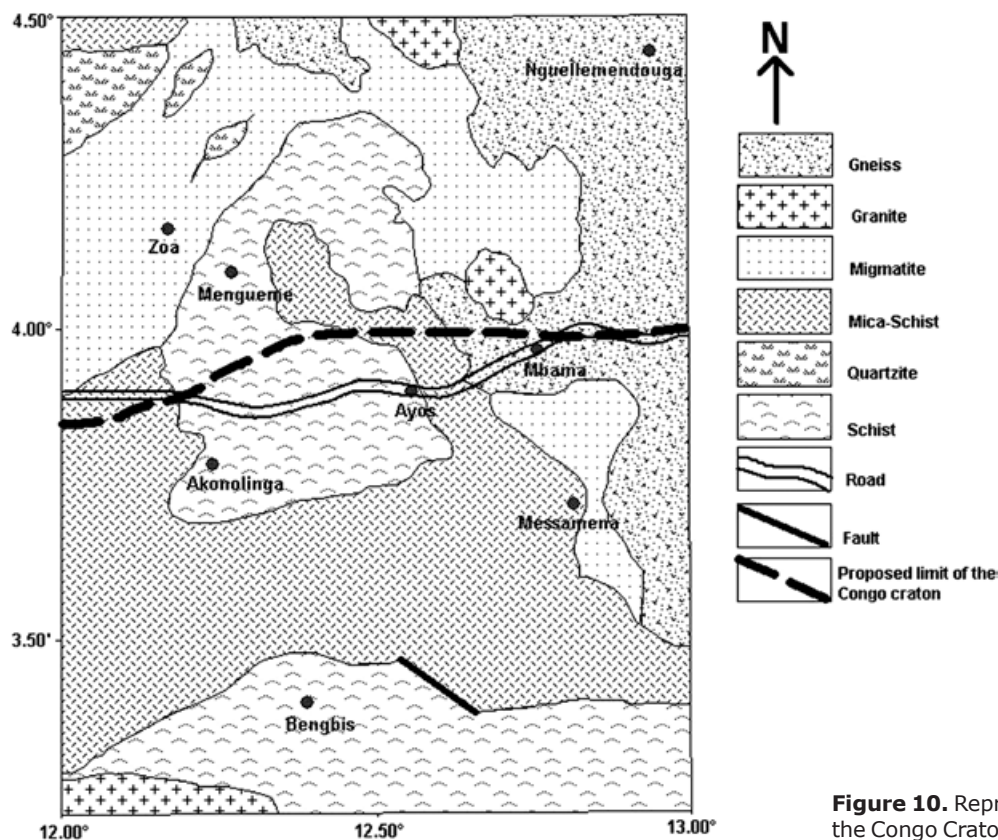


Figure 10. Representation of the limit of the Congo Craton on the geological map.

anomaly sources originate from the interior of the crust. This was also suggested by spectral analysis of the data. A series of buried faults were depicted by the gradient method and areas of interruption of leveling of anomalies. Various areas of granitic intrusions were observed from the modeling. Fault lines have been identified from qualitative analysis. Based on geological data, some of the proposed faults turned out to be variations of magnetic susceptibilities of metamorphic rocks.

The present results are in agreement with gravity studies in adjacent areas which highlight a reseau of faults oriented W-E (Ndougsa *et al.*, 2002 & 2003; Basseka *et al.*, 2011; Shandini *et al.*, 2010 & 2012), and the audiomagnetotelluric data analysis that puts in evidence a secondary fault line with SW-NE general trend (Ndougsa *et al.*, 2011 & 2012).

From the results in this work, the geophysical limit of the Congo Craton (Figure 11) is located around the parallel of latitude 4° N which is slightly extended to the North relative to the known limit of the Craton that appears on the surface of the Earth (Figure 2). We find that, part of the Pan African domain lies on top of the Congo Craton.

Acknowledgments

We are grateful to Professor R. J. Gordon Cooper, School of Earth Sciences, and chairman of the Geophysics group at the University of Witwatersrand for letting us use his 2.5D magnetic modeling and inversion program.

Bibliography

- Basseka C.A., Shandini Y.N., Tadjou J.M., 2011, Subsurface Structural Mapping Using Gravity Data of the northern edge of the Congo Craton, South Cameroon. *Geofizika*, 28, 2, 231-244.
- Bhattacharyya B.K., Lei-Kuang Leu, 1975, Spectral analysis of gravity and magnetic anomalies due to two-dimensional structures. *Geophysics*, 40, 993-1013.
- Collignon F., 1968, Gravimétrie de reconnaissance de la République Fédérale du Cameroun. ORSTOM (Office de la Recherche Scientifique et Technique d'Outre-Mer, Paris, France), 35 p.
- Cooper G.R.J., 2003, Mag2dc 2.10. An interactive 2.5D Magnetic modelling and inversion program for Microsoft windows, School of Geosciences University of the Witwatersrand, Johannesburg 2050 South Africa.
- Djouka F.M.L., Schüssler U., Tchouankoue J.P., 2004, Geochemistry and petrogenesis of neoproterozoic granitoids within the Central African Fold Belt in the Bafoussam area, Western Cameroon (Central Africa). University of Wuerzburg, Germany, 4 p.
- Manguelle-Dicoum E., Bokossah A.S., Kwende-Mbanwi T.E., 1992, Geophysical Evidence for a major Precambrian shist-granite boundary in southern Cameroon. *Tectonophysics*, 205, 437-446.
- Mbom Abane S. 1997, Investigation géophysique en bordure du craton du Congo (région d'Abong-Mbang/ Akonolinga) et implication structurale. Thèse de Doctoral d'Etat en Science, Université de Yaoundé 1, 180p.
- Meying A., Ndougsa-Mbarga T., Manguelle-Dicoum E., 2009, Evidence of fractures from the image of the subsurface in the Akonolinga-Ayos area (Cameroon) by combining the Classical and the Bostick approaches in the interpretation of audio-magnetotelluric data. *J. Geology and Mining Research*, 1, 8, 159-171.
- Mvondo H., Owona S., Mvondo-Ondoa J., Essono J., 2007, Tectonic evolution of the Yaoundé segment of the Neoproterozoic Central African Orogenic Belt in southern Cameroon. *Can. J. Earth Sci.*, 44, 433-444.
- Ndougsa-Mbarga T., Feumoé A.N.S., Manguelle-Dicoum E., Fairhead J.D., 2012, Aeromagnetic Data Interpretation to Locate Buried Faults in South-East Cameroon. *Geophysica*, 47, 1-2, 49-63.
- Ndougsa-Mbarga T., Meying A., Bisso D., Sharma K.K., Layu D.Y., Manguelle-Dicoum E., 2011, Audiomagnetotelluric (AMT) soundings based on the Bostick approach and evidence of tectonic features along the northern edge of the Congo Craton, in the Messamena/Abong-Mbang. *J. Ind. Geophys. Union*, 15, 3, 145-159.
- Ndougsa-Mbarga T., Manguelle-Dicoum E., Tabod C.T., Mbom Abane S., 2003, Modélisation d'anomalies gravimétriques dans la région de Mengueme-Akonolinga (Cameroun). *Sci. Technol. Dev.*, 10, 1, 64-74.
- Ndougsa-Mbarga T., Manguelle-Dicoum E., Mbom-Abane S., Tabod C.T., 2002, Deep crustal structures along the north eastern margin of the Congo Craton in the Abong-Mbang/Bertoua region (Cameroon) based on gravity data. In: *Electronics Memories of the 2nd Cuban Geophysical Congress and the IV Latin American Geophysical Conference*, 2002, Cuba, CD Rom 15p.

- Nnange J.M., Ngako V., Fairhead J.D., Ebinger C.J., 2000, Depths to density discontinuities beneath the Adamawa Plateau region, Central Africa, from spectral analysis of new existing gravity data. *Journal of African Earth Sciences*, 30, 887-901.
- Olinga J.B., Mpesse J.E., Minyem D., Ngako V., Ndougsa-Mbarga T., Ekodeck G.E., 2010, The Awaé - Ayos strike-slip shear zones (Southern-Cameroon): Geometry, kinematics and significance in the late Pan-African tectonics. *N. Jb. Geol. Paläont. Abh.*, 257, 1, 1-11.
- Paterson Grant, Watson Ltd, 1976, Etudes aeromagnetiques sur certaines Régions de la République Unie du Cameroun. ACIDI, Toronto, Canada, 190p.
- Robert S.C., 1982, Handbook of Physical Properties of Rocks. Vol. II, CRC Press, Inc.
- Shandini N.Y., Tadjou J.M., 2012, Interpreting gravity anomalies in South Cameroon, Central Africa. *Earth Sci. Res.*, 16, 1, 5-9.
- Shandini N.Y., Tadjou J.M., Tabod C.T., Fairhead J.D., 2010, Gravity data interpretation in the northern edge of the Congo Craton, South-Cameroon. *Anuario do Instituto de Geociências*, 33, 1, 73-82.
- Spector A., Grant F.S., 1970, Statistical models for interpretation aeromagnetic data. *Geophysics*, 35, 293-302.
- Tadjou J.M., Nouayou R., Kamguia J., Kande H.L., Manguelle-Dicoum E., 2009, Gravity analysis of the boundary between the Congo Craton and the Pan-African belt of Cameroon. *Austrian Journal of Earth Sciences*, 102, 71-79.
- Talwani M., 1965, Computation with the help of a digital computer of magnetic anomalies caused by bodies of arbitrary shape. *Geophysics*, 30, 797-817.
- Telford W.M., Geldart L.P., Sheriff R.E., Keys D.A., 1990, Applied Geophysics 4th edition, Cambridge University Press, Cambridge, G.B., 860p.
- Toteu S.F., Penaye J., Poudjom D.Y., 2004, Geodynamic evolution of the Pan-African belt in the central Africa with special reference to Cameroon. *Can. Journ. Earth Sci.*, 41, 73-85.
- Vicat J.P., 1998, Esquisse géologique du Cameroun. Collection GEOCAM, Presses Universitaires Yaoundé, pp. 3-11.

Active segment of the 12 November 2003 Mw 5.6 earthquake at Salsipuedes oceanic basin, Gulf of California. Mexico

Leobardo López-Pineda*, Luis Quintanar Robles, Carlos Isidro Huerta López and Héctor Enrique Rodríguez Lozoya

Received: May 05, 2011; accepted: August 06, 2013; published on line: December 11, 2013

Resumen

Analizamos el registro de ocho estaciones autónomas con sismógrafos de banda ancha de la red conjunta entre la Universidad de Utrecht, Instituto Tecnológico de California y Centro de Investigación Científica y de Educación Superior de Ensenada, del sismo Mw. 5.6, que ocurrió el 12 de noviembre de 2003, en la cuenca oceánica *Salsipuedes* en la parte media del Golfo de California, a 2 km al oeste de la isla Ángel de la Guarda. Este evento se localizó en las coordenadas geográficas 29.16°N y 113.37°O a 30 kilómetros al noreste de Bahía de los Ángeles, además un precursor y cientos de réplicas se registraron en las 48 horas siguientes de su tiempo origen. Con la localización de 29 sismos identificamos el segmento activo, perpendicular a la principal falla transformante NW-SE del *Canal de Ballenas* que representa el límite transtensional entre las placas del Pacífico y Norte América. La dirección de la falla activa descrita es congruente con el mecanismo de falla normal propuesto por el NEIC dependiente del United States Geological Survey, cuyos valores indican un rumbo de 39°, echado de 34° y deslizamiento de -44°.

Con el análisis de la magnitud de duración de 456 réplicas, calculamos un valor de $b=1.14\pm 0.28$. Además determinamos un momento sísmico de $(3.5 \pm 3.3) \times 10^{17} \text{Nm}$, el radio de la fuente fue de $3.7 \pm 2.63 \text{ km}$ y la caída de esfuerzos estática fue de $3.94 \pm 1.15 \text{ MPa}$ ($39.4 \pm 11.5 \text{ bar}$).

Palabras clave: parámetros de fuente, sismotectónica, Golfo de California.

Abstract

We analyzed records of eight seismic stations of the autonomous broadband seismograph network of a joint project between Utrecht University (the Netherlands), California Institute of Technology, and *Centro de Investigación Científica y de Estudios Superiores de Ensenada* (CICESE). These stations recorded the Mw 5.6 earthquake that occurred on 12 November 2003 at *Salsipuedes* basin in the middle of the Gulf of California 2 km west of the island *Angel de la Guarda*. This event was located at 29.16° N and 113.37° W, 30 km northeast of *Bahia de los Angeles*. A foreshock and hundreds of aftershocks were recorded in the 48 hours after its origin time. With the location of 29 earthquakes we identified the active segment, perpendicular to the main transform fault NW-SE of *Canal de Ballenas*, representing the transtensional boundary between the Pacific and North American plates. The direction of the active fault described is consistent with the normal fault mechanism reported by the National Earthquake Information Center (strike=39°, dip=34°, slip=-44°).

From the duration magnitude of 456 aftershocks, we calculated a b -value of 1.14 ± 0.28 ; furthermore, we calculated a seismic moment of $(3.5 \pm 3.3) \times 10^{17} \text{Nm}$, a source radius of $3.7 \pm 2.63 \text{ km}$, and a static stress drop of $3.94 \pm 1.15 \text{ MPa}$ ($39.4 \pm 11.5 \text{ bar}$).

Key words: source parameters, seismotectonics, Gulf of California.

L. López-Pineda*
Programa de Ingeniero en Geociencias
Unidad Académica Hermosillo
Universidad Estatal de Sonora
Sonora, México
*Corresponding author: leobardo.lopezpineda@gmail.com

L. Quintanar Robles
Instituto de Geofísica
Universidad Nacional Autónoma de México
Ciudad Universitaria
Delegación Coyoacán, 04510
México D.F, México

C.I. Huerta López
Centro de Investigación Científica
y Educación Superior de Ensenada
Carretera Ensenada-Tijuana Núm. 3918
Zona Playitas, Ensenada 22860
Baja California, México

H.E. Rodríguez Lozoya
Facultad de Arquitectura
Facultad de Ingeniería Civil
Universidad Autónoma de Sinaloa
Sinaloa, México

Introduction

Since the Miocene, the Gulf of California has been continuously affected by a slow rifting with NW-SE displacement between the North American and the Pacific plates. This process generates a high seismicity rate, volcanism, seafloor spreading, thinning of the continental crust and geothermal processes (Lomnitz *et al.*, 1970).

The *Centro de Investigación Científica y de Educación Superior de Ensenada* (CICESE), in a joint project with Utrecht University (the Netherlands) and the California Institute of Technology (Trampert *et al.*, 2003) deployed 22 broadband digital seismic stations of continuous recording, more than one year prior the occurrence of the studied earthquake, as part of the Network of Autonomously Recording Seismographs, (NARS-Baja) array.

The stations were deployed all along the 1200 km of the *Baja California* peninsula, Sonora, and Sinaloa states around the Gulf of California. The purpose of this network was to study local and regional seismicity and the crust and upper-mantle structure.

In this study, we relocated the 12 November 2003 Mw 5.6 earthquake. We examined the source parameters of the mainshock using the local seismic network. We also estimated source displacement spectra, $M_o(f)$ and, through the analysis of seismicity we identified the alignment of rupture and estimated the b -value.

Tectonics and seismicity

In the middle of the Gulf of California the *Salsipuedes* basin is bounded by the *Baja*

California peninsula to the west and the *Angel de la Guarda* Island to the east. Frequent earthquake swarms are well documented to occur in the northern end of this zone (Rebollar *et al.*, 2001). Eventhough there is a transform fault connecting the *Salsipuedes* with *Tiburón* and *Delfin* basins (at the southeast and northwest ends, respectively), serious doubts arise to the plate boundary position due to the complexity of the structures interpreted, and by the bathymetric information showing faults at both sides of the island. In addition, Vaquier and Whiteman (1973) in an experiment conducted between 1970-1971 determined 4 mm/year of relative displacement between *Angel de la Guarda* Island and the peninsula of *Baja California*. Kasser *et al.* (1987) using laser geodimeter measurements between stations located on elevated points of *Baja California* and Sonora, estimated a right lateral shear motion direction (N46°W and 8 mm/year) in the *Salsipuedes* basin. Lonsdale (1989) indicated the existence of grabens and horsts structures at the Gulf of California, nearby to *Angel de la Guarda* Island with azimuth of 312°, which is the same direction of the transform fault. From 1973 until 2003, the reported seismicity includes few earthquakes of magnitude greater than 5; all of them with right-lateral strike slip fault mechanism (Goff *et al.*, (1987), GCMT catalog, www.globalcmt.org). In Table 1 relevant information of the earthquakes mentioned above is provided. Among them in 1975, an $M_s=6.5$ earthquake is of particular interest because it was associated with the structure of *Salsipuedes* basin, as well as its aftershocks (Munguía *et al.*, 1977).

Data recording and earthquake location

On 12 November 2003, an earthquake occurred in the *Salsipuedes* basin and was recorded by

Table 1. Earthquakes with magnitude greater than 5 that have occurred in the neighbourhood of *Salsipuedes* basin and *Canal de Ballenas*.

Zone	Date	Latitude °	Longitude °	Seismic Moment Nm	Magnitude Mw
Canal de Ballenas north	1973/10/13 ¹	29.58	-113.64		5.2
	1975/07/08 ³	29.49	-113.40	1.6X10 ¹⁸	6.5
	1980/08/30 ²	29.7	-113.73	2.23X10 ¹⁷	5.5
	1991/02/14 ²	30.12	-113.70	1.64X10 ¹⁷	5.4
Canal de Ballenas south	1977/11/14 ¹	29.27	-112.97		5.6
Salsipuedes basin	1977/11/21 ²	29.07	-113.10	1.23X10 ¹⁸	6.0
	1980/09/21 ²	29.34	-113.73	2.49X10 ¹⁷	5.5
	1982/02/07 ²	29.03	-113.03	2.86X10 ¹⁷	5.6
	1993/03/05 ²	29.25	-113.43	4.15X10 ¹⁷	5.7
	1997/11/26 ²	29.38	-113.80	1.4X10 ¹⁷	5.4
	2003/11/12 ⁴	29.0	-113.24	(3.5±3.3)X10 ¹⁷	5.6±0.2

¹ NEIC. ² Global CMT catalog. ³ Goff *et al.* (1987). ⁴ This study.

the NARS-Baja network as well as its associated foreshock, and 456 aftershocks occurred during the following two days.

The NARS-Baja seismic stations, NE74, NE75, NE80, NE81, and NE82, consisted of a Streckeisen STS-2 broadband sensor with a generator constant of 1500 V*s/m and a bandwidth response between corners 0.0083 Hz (120 sec) and 50 Hz, a Global Positioning System (GPS), and a laptop for data acquisition and timing (Trampert *et al.*, 2003). The RESBAN station network consists of a Guralp CMG-40T or CMG-3ESP broadband sensor. All seismic stations recorded continuously with a rate of 20 samples per second (See Figure 1).

Using the closest stations of the NARS-Baja network (NE74, NE75, NE80, NE81, NE82), and the ones of RESBAN network (BAHB, IAGU, PLIB) to the epicenter, we relocate the mainshock using the HYPOCENTER code (Lienert *et al.*, 1988; Lienert and Havskov, 1995) and a velocity model that includes a thin continental crust with a Moho depth in the range from 20 to 24 km. This model was used by Rebollar *et al.* (2001) and it is displayed in Table 3. The records with the best signal-to-noise ratio correspond to the stations shown in Figure 2. The mainshock was located at 29.16°N and 113.37°W. This event had a Mw 4.4 foreshock, with epicentral location at 29.17°N and 113.356°W. Table 2 and

Figure 3 show the location of the mainshock, the foreshock and 27 aftershocks at the rupture area and post-event seismic activity. You can see the rupture area marked by a white star and a set of aftershocks that identify it, also showed the post-event seismicity, and associated with an existing structure in the oceanic floor. Note the perfect partnership between the structures and seismicity.

We constructed a vertical section perpendicular to the strike of the fault and plot the position of the mainshock, foreshock and aftershocks with respect to depth; this vertical section is shown in Figure 4. We note that the seismogenic zone reaches a depth of 12 km, suggesting a brittle crust of similar thickness.

b-value

The statistical Gutenberg-Richter (1942) *b*-value was estimated for the aftershock sequence in order to identify a seismotectonic pattern of the *Salsipuedes* basin. The duration magnitude (M_d) of 476 aftershocks recorded at seismic station BAHB, was calculated using the equation (1):

$$M_d = 2.24 \log T - 0.85, \quad (1)$$

where T is the duration of the signal. This relationship has been used by Rebollar and Reichle (1987), López-Pineda and Rebollar (2005).

Figure 1. Location of broadband seismic stations (filled triangles) and the 12 November 2003 Mw 5.6 earthquake (white star). The location of the centroid proposed by Global CMT Project and CMT GS are indicated by red circles. Dashed line indicate section AA' to which the seismicity was projected. The relative motion of tectonic plates is indicated with large arrows.

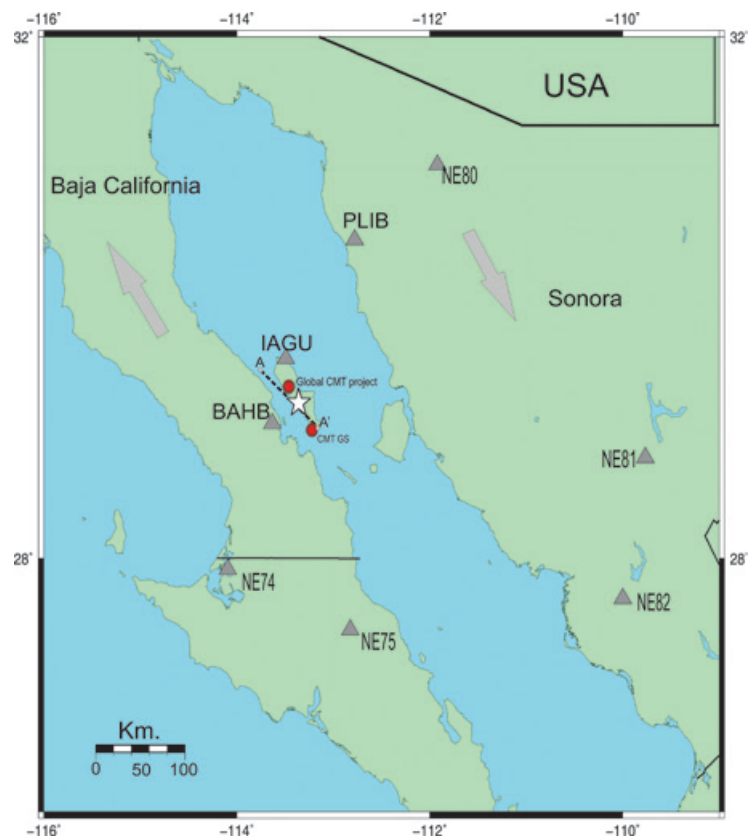


Table 2. Location: ¹foreshock, ² mainshock, and aftershocks using HYPOCENTER code.

Date	Hour	Latitude°	Longitude°	Depth (km)	Error Lon °	Error Lat °	Error Depth (km)
20031112 ¹	04:47	29.171	-113.357	8.2	0.7	0.5	4.3
20031112 ²	04:54	29.160	-113.370	3.6	0.2	0.1	1.2
20031112	05:16	29.167	-113.363	8.2	0.3	0.2	0.1
20031112	06:03	29.174	-113.356	6.8	0.0	0.0	0.0
20031112	06:45	29.120	-113.405	5.5	0.0	0.0	0.0
20031112	06:51	29.160	-113.370	8.1	0.2	0.1	0.0
20031112	07:40	29.227	-113.467	12.5	0.2	0.1	0.1
20031112	07:43	29.162	-113.483	11.6	0.3	0.1	0.1
20031112	07:50	29.124	-113.403	4.5	0.0	0.0	0.0
20031112	07:57	29.123	-113.403	4.0	0.0	0.0	0.0
20031112	08:08	29.113	-113.413	5.8	0.0	0.0	0.0
20031112	08:16	29.132	-113.395	8.2	0.6	0.4	0.0
20031112	08:24	29.137	-113.039	8.0	0.6	0.4	0.0
20031112	08:31	29.160	-113.370	4.1	0.0	0.0	0.0
20031112	08:41	29.125	-113.397	1.9	0.0	0.0	0.0
20031112	08:59	29.114	-113.408	8.1	0.1	0.1	0.0
20031112	09:56	29.083	-113.402	0.0	0.1	0.1	0.0
20031112	10:01	29.108	-113.417	6.0	0.1	0.1	0.0
20031112	11:32	29.118	-113.408	4.6	0.0	0.0	0.0
20031112	11:51	29.159	-113.375	8.2	0.1	0.1	0.0
20031112	12:51	29.092	-113.408	0.0	0.1	0.1	0.1
20031112	13:01	29.105	-113.410	0.0	0.1	0.1	0.0
20031112	14:04	29.113	-113.413	0.0	0.1	0.1	0.0
20031112	15:07	29.151	-113.367	1.4	0.0	0.0	0.0
20031112	16:26	29.162	-113.368	8.3	0.0	0.0	0.0
20031112	16:49	29.164	-113.365	3.0	0.0	0.0	0.0
20031112	18:48	29.162	-113.367	8.1	0.1	0.1	0.1
20031112	19:04	29.161	-113.368	3.8	0.0	0.0	0.0
20031112	19:16	29.095	-113.427	0.0	0.0	0.0	0.0

Table 3. Crustal velocity model used to locate the 12 November 2003 earthquake Mw 5.6 and its associated foreshocks and aftershock (Rebollar *et al.*, 2001).

Layer Thickness (km)	P-wave velocity (km/sec)	S-wave velocity (km/sec)	Density (g/cm ³)	Q_α	Q_β
4.0	4.0	2.6	2.3	400	200
4.0	5.7	3.3	2.5	2000	2000
16.0	6.7	3.8	3.0	2000	2000
0.0	7.8	4.0	3.4	2000	2000

Duration magnitudes of the located earthquakes range from 2.3 to 3.5. The b -value from the Gutenberg-Richter relationship was calculated and the estimated b -value was 1.14 ± 0.28 using a least-squares approach (Figure 5).

This b -value contrasts with that obtained for Loreto earthquake of 12 March 2003 using 333 aftershocks. López-Pineda and Rebollar (2005) obtained a b -value of 0.68. This difference suggests larger heterogeneous concentration of

stresses at *Salsipuedes* basin than *Carmen* basin (Scholz, 1968).

Regarding the moment tensor solution, there are two proposed mechanisms for the earthquake fault of 12 November 2003 Mw 5.55 ± 0.05 ; these solutions are shown in Table 4. As it is noted in Figure 3, the seismicity location agrees with a trend perpendicular to the main transform NW-SE fault. A strike of 39° is therefore more consistent with the tectonics of the area.

Figure 2. Normalized velocity seismograms recorded by the BAHB, PLIB, NE80, NE81, and NE82 seismic stations in their Z, N, and E components.

Source spectrum and stress drop

We estimated the average displacement spectra, $\dot{M}_0(f)$, of the mainshock from the analysis of the S-wave group recorded at horizontal components of 5 stations within a hypocentral distance of 475 km. Following Singh *et al.* (1999), the Fourier acceleration spectral amplitude of the intense part of the ground motion at a station, under far-field, point-source approximation, may be written as

$$A(f, R) = Cf^2 \dot{M}_0(f)G(R)e^{-\pi fR/\beta Q(f)}, \quad (2)$$

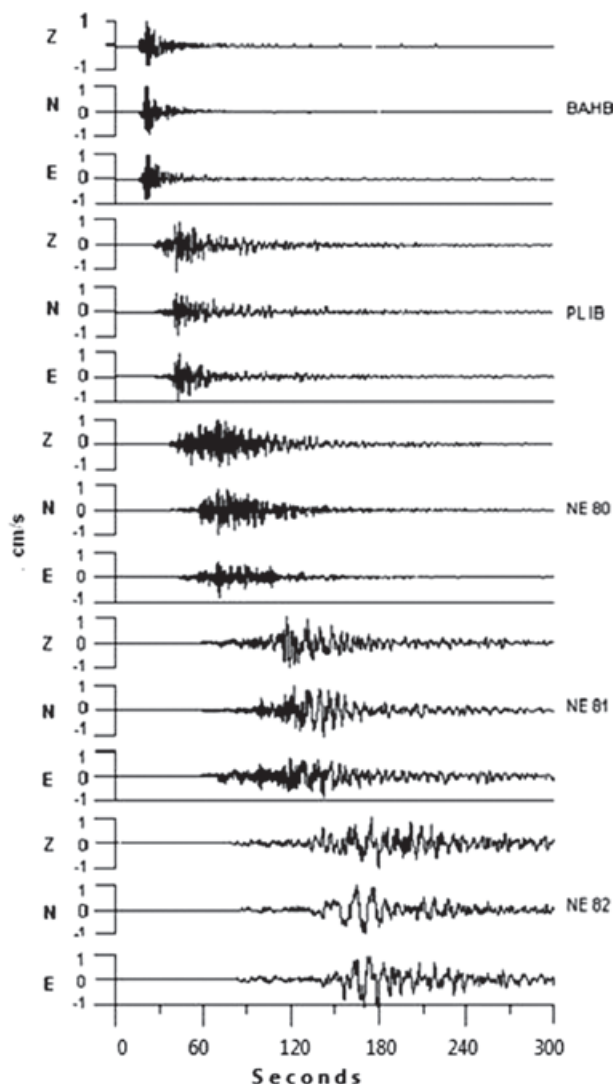
where

$$C = FPR_{\theta\phi}(2\pi)^2/(4\pi\rho\beta^3), \quad (3)$$

In the equations above, $\dot{M}_0(f)$ is the moment rate spectrum so that $\dot{M}_0(f) \rightarrow M_0$ as $f \rightarrow 0$, R = hypocentral distance, $R_{\theta\phi}$ = average radiation pattern (0.55), F = free surface amplification (2.0), P takes into account the partitioning of energy in the two horizontal components ($\frac{1}{\sqrt{2}}$), β = shear-wave velocity at the source (3.00 km/s), ρ = density in the focal region (2.65 kg/m³), and $Q(f)$ = quality factor, which includes both anelastic absorption and scattering. The appropriate geometrical spreading term, $G(R)$, is R^{-1} for $R \leq R_0$ and $(RR_0)^{-1/2}$ for $R > R_0$. The form of $G(R)$ implies dominance of body waves for $R \leq R_0$ and of surface waves for $R > R_0$. For this earthquake, we took $Q(f) = 213f^{0.72}$ (Rebollar *et al.*, 1995) and $R_0 = 100$ km. Taking logarithms of equation 2 we obtain

$$\log[A(f, R)] = \log C + \log[G(R)] + \log\left[f^2 \dot{M}_0(f)\right] - \frac{1.36fR}{\beta Q(f)}. \quad (4)$$

We solved equation (4) in the least-squares sense to obtain $\log[f^2 \dot{M}_0(f)]$ and so $\dot{M}_0(f)$.



The source displacement spectra of the mainshock for the 5 stations are shown in Figure 6. We interpret these spectra within the framework of a ω^2 -source model and obtain an estimation of the seismic moment (M_0) and corner frequency (f_c). The stress drop ($\Delta\sigma$) is computed using the Brune (1970) model. The source spectra can be fit by M_0 , f_c and $\Delta\sigma$ values indicated in these figures.

The Brune model consists in a circular fault plane with finite radius on which a shear stress pulse is applied instantaneously on the whole fault

Table 4. Earthquake location and fault geometry calculated by CMT GS, <http://earthquake.usgs.gov/earthquakes/eqarchives/sopar/> and Global CMT Project, www.globalcmt.org.

Source	Lat.	Long.	Depth	Mw	Plane 1			Plane 2		
					Strike	Dip	Rake	Strike	Dip	Rake
NEIC	29.11	-113.35	7	5.6	168	67	-116	39	34	-44
GCMT	29.34	-113.45	15	5.5	168	55	-109	19	39	-65

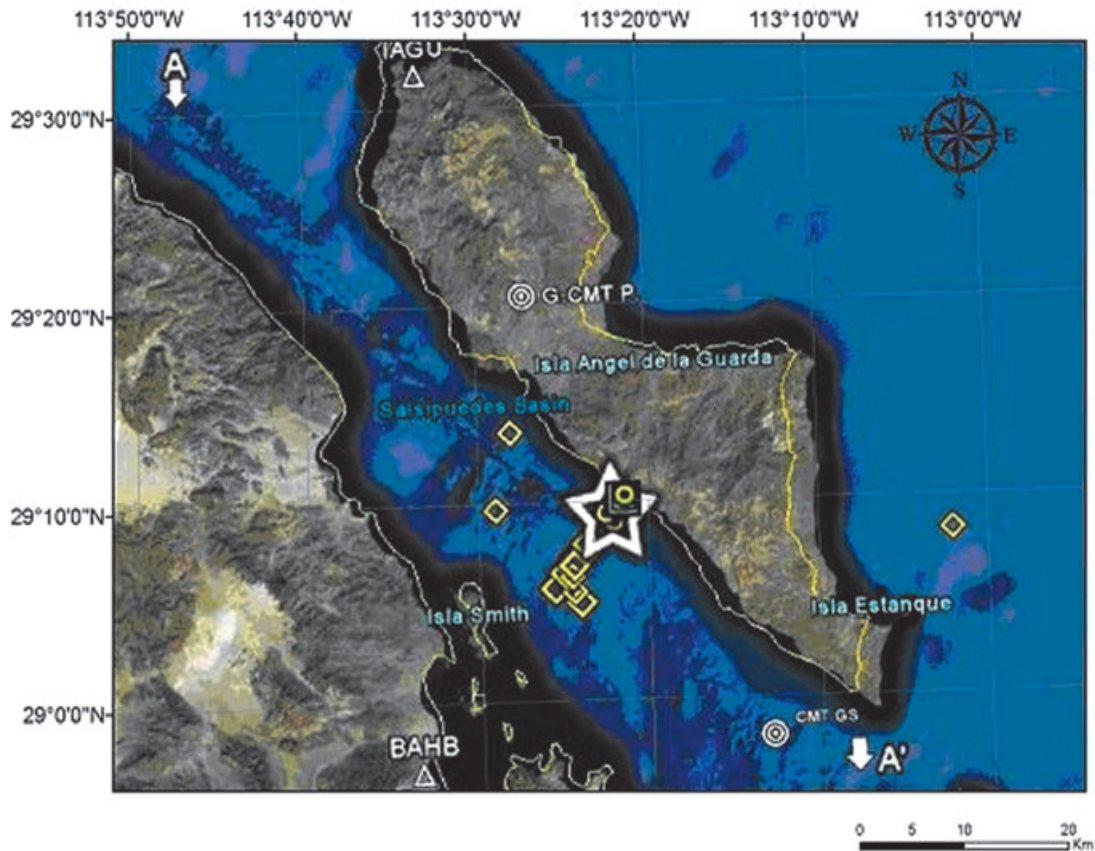


Figure 3. Seismicity of the study area, the star shows the location of the 12 November 2003 Mw 5.6 earthquake at *Salsipuedes* basin, the square shows the foreshock. The size of the star indicates the extent of aftershock area (open circles). The diamonds indicate the post-event activity which covers a pre-existing alignment (Observed structures on the ocean floor). White open triangles indicate stations and concentric white circles denote the location of the centroid according to GCMT and CMT GS.

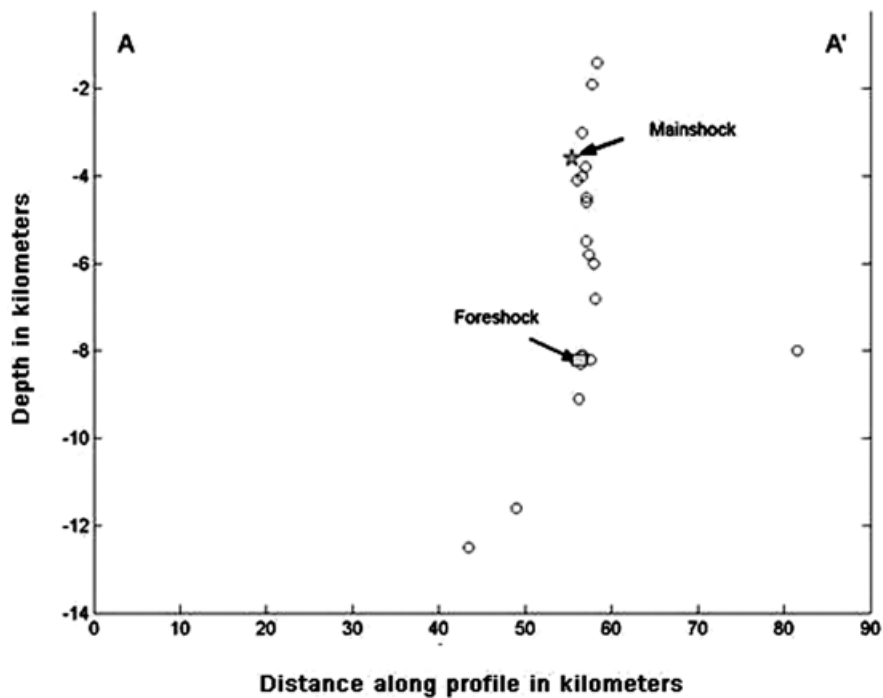
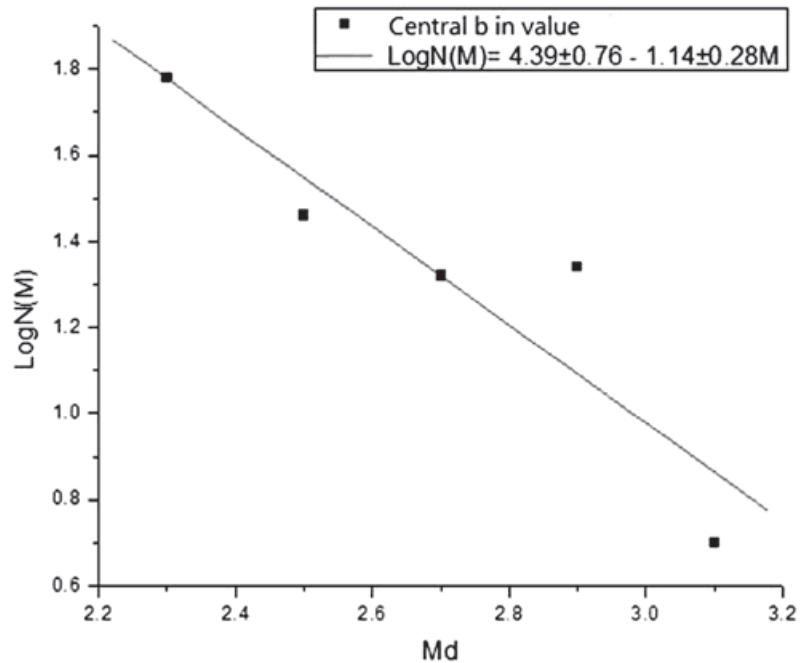


Figure 4. Vertical section of the recorded seismicity projected along the line AA' shown in Figure 1. The foreshock and mainshock are indicated by a square and a star respectively.

Figure 5. Frequency-magnitude plot of 476 aftershocks of the 12 November 2003 earthquake in Salsipuedes basin. A *b*-value of 1.14 ± 0.28 was calculated for duration magnitudes in the range at $2.3 \leq M \leq 3.1$ using a least-squares fit.



area and there is no fracture propagation. This model is commonly used to obtain fault dimensions from spectra of S waves for earthquakes of small-to-moderate size ($M < 6$), for which the circular fault is a good approximation. Under this hypothesis, the source radius is given by:

$$r = 0.3724\beta/f_c \tag{5}$$

The moment magnitude was calculated by Equation (6), proposed by Hanks and Kanamori (1979)

$$M_w = \frac{2}{3} \log M_0 - 10.7 \tag{6}$$

Taking the average value for these parameters, we obtain finally $M_0 = (3.5 \pm 3.3) \times 10^{17} \text{Nm}$, $f_c = 0.36 \pm 0.15 \text{ Hz}$, $r = 3.7 \pm 2.6 \text{ km}$ and $\Delta\sigma = 3.9 \pm 1.15 \text{ MPa}$ ($39 \pm 11.5 \text{ bar}$).

Discussion and Conclusions

According to results of seismic reflection studies conducted in the upper part of the Gulf of California by Lonsdale (1989) and González-Fernández *et al.* (2005), the *Salsipuedes* basin is in its early stage of development. In this region the basins are aligned in an en echelon trend linking the pull-apart basin by NW-SE transform faults. *Canal de Ballenas* transform fault connects the *Salsipuedes* basin at SE with the *Delfin* basin at the NW. In this zone, six earthquakes with magnitude larger than 5 have occurred during the last thirty years. The focal mechanisms of

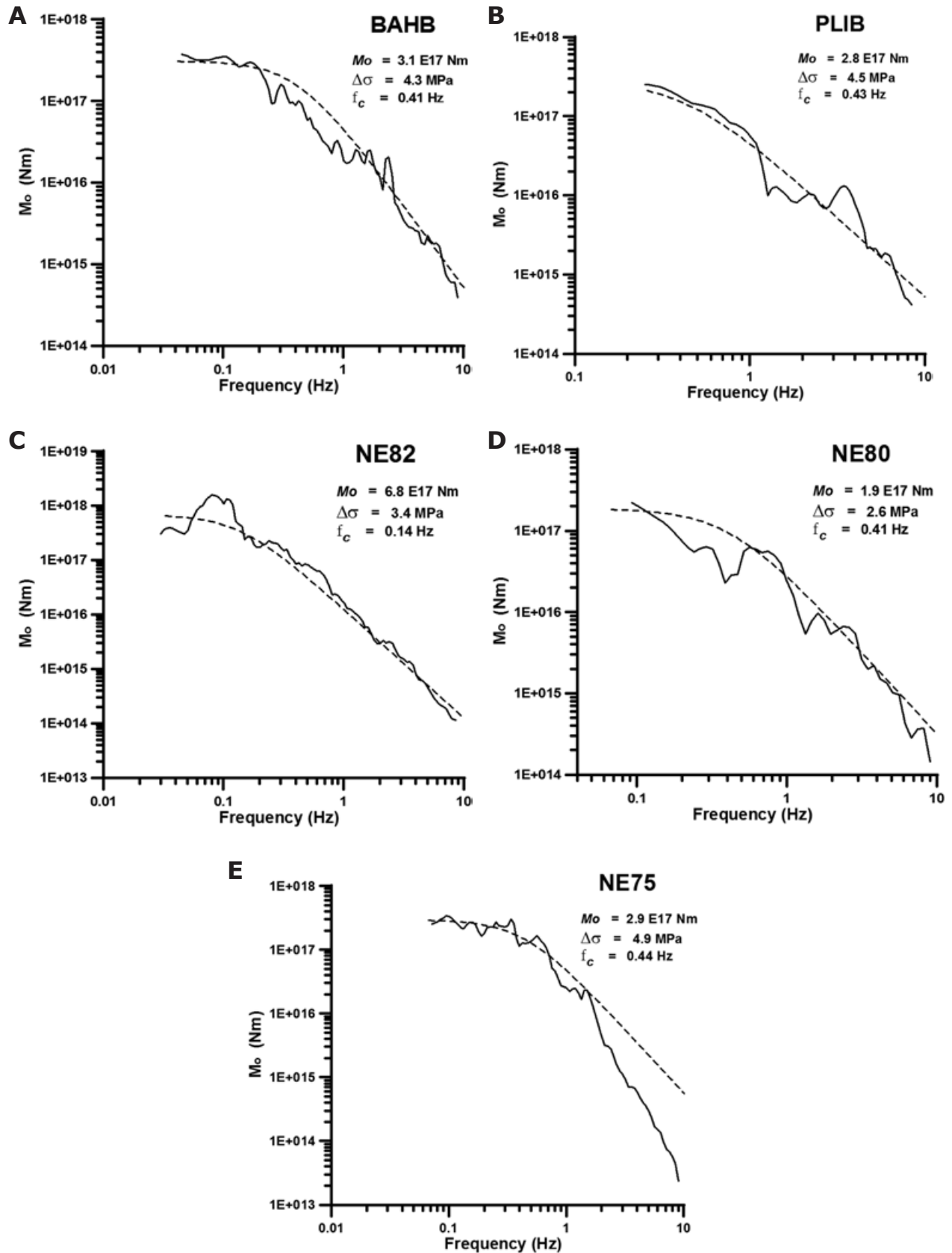
the great majority of these earthquakes were strike-slip. The earthquake studied here is the first one with a dip-slip mechanism in this part of the Gulf of California, which was located off the west coast of *Angel de la Guarda* Island. Other earthquakes with normal faulting mechanisms have been reported by Rebollar *et al.* (1995) at *Bahia de las Animas* (30 km south of the epicenter of study) and Reichle and Reid (1977) following a seismic swarm pattern at *Delfin* basin, (60 km northwest of the epicenter of study). Castro *et al.* (2011) associates this type of faulting in the Gulf of California to spreading centers.

The distribution of earthquakes with magnitude larger than 5 during the last thirty years suggests a seismic activity migration from north to south.

Table 5. Calculated source parameters. *r* is the source radii, M_0 is the seismic moment calculated from the displacement spectra, $\Delta\sigma$ is the static stress drop calculated with the displacement spectra.

Δ	<i>r</i> (km)	<i>f_c</i> Hz	M_0 (Nm)	$\Delta\sigma$ MPa
BAHB	2.72	0.41	3.1×10^{17}	4.3
PLI	2.60	0.43	2.8×10^{17}	4.5
NE80	2.72	0.41	1.9×10^{17}	2.6
NE75	2.54	0.44	2.9×10^{17}	4.9
NE82	7.98	0.14	6.8×10^{17}	3.4

Figure 6. S-wave average source displacement spectra of horizontal components at A) BAHB, B) PLIB, C) NE82, D) NE80, E) NE75 seismic stations. Continuous line is the observed spectrum and dashed line is the theoretical, assuming a w^2 source model.



Considering that the elastic energy stored in rocks in the form of deformation stress is released when the rocks reach their rupture, part of the energy propagates as vibrational energy producing seismic waves and another part of the energy remains in the rock as residual energy, this energy is transmitted to other parts of the same stress axis increasing the stress level of the adjacent regions (Husseini *et al.*, 1975). So the seismic energy released by fracturing and sliding at the northern edge of the *Canal de Ballenas* transform fault, triggered off significant seismicity at the southern edge of the transform. Examples of these sequences are: (i) the 1973-1975-1977 earthquakes, (ii) the 1980-1982 earthquakes, and (iii) the 1997-2003 earthquakes. All of these shocks were presumably seismically associated (see their latitudes shown in Table 1).

The earthquake studied here represents an example of active extensional faults at north of Gulf of California. Eventhough Sumy *et al.* (2013) propose that much of the extension across the plate boundary is accommodated aseismically, this activity shows that, at least in this zone, normal faulting plays an important role.

A Mw 4.4 foreshock occurred seven minutes before the 12 November 2003 Mw 5.6 earthquake. Both events were located on a dip slip fault perpendicular to the main *Canal de Ballenas* transform fault according their locations indicated on Figure 3.

The *b* value represent properties of the seismic medium in some respect, like stress or material conditions in the focal region Scholz (1968) and we expect an inverse correlation between the *b* value and the level of stresses accumulated in the seismic region. Others like Mogi (1962) have associated high *b*-values with the material heterogeneity. Through a comparative analysis of *b*-values estimations at north of Gulf of California between 1.5 (Reichle and Reid, 1977; Rebollar and Reichle, 1987), 0.68 for *Loreto's* earthquake of 12 March 2003 at *Carmen* basin (López-Pineda and Rebollar, 2005) and the *b* value of 1.14 ± 0.28 for this *Salsipuedes* basin earthquake at the middle of Gulf of California, we can infer that there is a transition of stress distribution from north, where the stresses are more heterogeneous, to south where concentration of stresses are more homogeneous, as well as in the central region of the Gulf of California.

From spectral analysis and assuming a Brune model of circular fault, we obtain the following source parameters:

$$M_0 = (3.5 \pm 3.3) \times 10^{17} \text{ Nm}$$

$$\text{Corner frequency } f_c = 0.36 \pm 0.15 \text{ Hz}$$

$$r = 3.7 \pm 2.6 \text{ km}$$

$$\Delta\sigma = 3.9 \pm 1.15 \text{ MPa } (39 \pm 11.5 \text{ bar.})$$

In agreement with the magnitude of 5.6 previously reported by NEIC; the calculated static stress drop is typical of this tectonic region ranging between 2 and 49 bars (López-Pineda and Rebollar, 2005) and the rupture radius is consistent with the magnitude of a moderate earthquake.

Acknowledgements

The greatest thanks to Dr. Cecilio Javier Rebollar Bustamante, deceased on September 2006, who was director of doctoral theses of two of the authors (LLP. and HERRL); this work is part of LLP's thesis. For health reasons and a long process of struggle against cancer Dr Rebollar could not publish it. Moreover we thank Arturo Perez Vertti and Arie van Wettum for the field work that they performed during the deployment of the seismic stations. We also thank Juan A. Mendoza and Omar Lugo Castillo for help in handling the digital data. Finally we wish to thank Dr. Xyoli Pérez-Campos her suggestions for improving the manuscript of this paper. The Consejo Nacional de Ciencia y Tecnología (CONACYT) sponsored partially this Project (Proyecto 37038-T). L.L.P was supported by Programa al Mejoramiento de Profesores (Promep).

Bibliography

- Brune J.N., 1970, Tectonic stress and the spectra of seismic shear waves from earthquakes. *J. Geophys. Res.*, 75, 4997–5009.
- Castro R.R, Perez-Vertti A., Mendez I., Mendoza A., Inzunza L., 2011, Location of Moderate-Sized Earthquakes Recorded by the NARS-Baja Array in the Gulf of California Region Between 2002 and 2006. *Pure Appl. Geophys.* 168:1279-1292
- Goff J.A., Bergman E.A., Solomon S.C., 1987, Earthquake source mechanism and transform fault tectonics in the Gulf of California. *J. Geophys. Res.*, 92, 10485–10510.
- González-Fernández A., Dañoibeitia J.J., Delgado-Argote L.A., Michaud F., Córdoba D., Bartolomé R., 2005, Mode of extension and rifting history of upper Tiburón and upper Delfin basins, northern Gulf of California. *J. Geophys. Res.*, 110, B01313, 17.
- Gutenberg B., Richter C.F., 1942, Earthquake magnitude, intensity, energy and acceleration. *Bull. Seismol. Soc. Am.*, 32, 163-191.

- Hanks T.C., Kanamori H., 1979, A moment magnitude scale, *J. Geophys. Res.*, 84, 2348-50.
- Husseini M., Jovanovich D., Randall M., Freud L., 1975, The fracture energy of the earthquakes. *Geophys. J.R. Astro. Soc.*, 43, 367-385 pp.
- Kasser M., Ruegg J.C., Lesage Ph., Ortlieb L., Pagarete J., Duch N., Guerrero J., Roldan J., 1987, Geodetic measurements of plate motions across the central Gulf of California, 1982-1986. *J. Geophys. Res. Lett.*, 14, 5-8.
- Lienert B.R., Berg E., Frazer L.N., 1988, HYPOCENTER: an earthquake location method using centered, scaled, and adaptively least squares. *Bull. Seismol. Soc. Am.*, 76, 771-783.
- Lienert B.R., Havskov J., 1995, A computer program for locating earthquakes both locally and globally. *Seismol. Res. Lett.*, 66, 26-36.
- Lomnitz C., Mooser F., Allen C.R., Brune J.N., Thatcher W., 1970, Seismicity and tectonics of the northern Gulf of California region; preliminary results. *Geofísica Internacional*, 10, 37-48.
- Lonsdale P.L., 1989, Geology and tectonics history of the Gulf of California, in: *The Geology of North America: The Eastern Pacific Ocean and Hawaii*, Vol. N, The Geological Society of America.
- López-Pineda L., Rebolgar C.J., 2005, Source characteristics of the (M_w 6.2) Loreto earthquake of 12 March 2003 that occurred in a transform fault in the middle of the Gulf of California, México. *Bull. Seismol. Soc. Am.*, 95, 419-430.
- Mogi K., 1962, Magnitude-frequency relationship for elastic shocks accompanying fractures of various materials and some related problems in earthquakes. *Bull. Earthquake Res. Inst. Univ. Tokyo.*, 40, 831-883.
- Munguía L., Reichle M., Reyes A., Simons R., Brune J., 1977, Aftershocks of the 8 July 1975 Canal de las Ballenas, Gulf of California, Earthquake; *Geophys. Res. Lett.*, 4, 507-509.
- Rebolgar C.J., Reichle M.S., 1987, Analysis of the seismicity detected in 1982-1984 in the Northern Peninsular ranges of Baja California, *Bull. Seismol. Soc. Am.*, 77, 173-183.
- Rebolgar C.J., Castillo-Román J., Uribe A., 1995, Parámetros de fuente de la actividad sísmica que ocurrió en Marzo de 1993 en la Bahía de las Animas. Baja California. Unión Geofísica Mexicana, In: *Monografía 2. La Sismología en México: 10 años después del temblor de Michoacán del 19 de Septiembre de 1985 (Ms 8.1)*.
- Rebolgar C.J., Quintanar L., Castro R., Day S., Madrid J., Brune J.N., Astiz L., Vernon F., 2001, Source characteristics of a 5.5 magnitude earthquake that occurred in the transform fault system of the Delfin Basin in the Gulf of California. *Bull. Seismol. Soc. Am.*, 91, 781-791.
- Reichle M., Reid I., 1977, Detailed study of earthquake swarms from the Gulf of California. *Bull. Seismol. Soc. Am.*, 67, 159-171.
- Sholz C.H., 1968, The frequency-magnitude relation of microfracturing in rock and its relation to earthquakes. *Bull. Seismol. Soc. Am.*, 58, 399-415.
- Singh S.K., Ordaz M., Pacheco J.F., Quaas R., Alcántara L., Alcocer S., Gutiérrez C., Meli R., Ovando E., 1999, A Preliminary Report on the Tehuacán, México Earthquake of June 15, 1999 (M_w=7.0); *Seismological Research Letters*, 70, 5, September/October 1999, pp. 489-504.
- Sumy D.F., Gaherty J.B., Kim W.Y., Diehl T., Collins J.A., 2013, The Mechanisms of Earthquakes and Faulting in the Southern Gulf of California. *Bull. Seismol. Soc. Am.*, 103, 487-506.
- Trampert J., Paulssen H., van Wettum A., Ritsema J., Clayton R., Castro R., Rebolgar C.J., Perez-Vertti A., 2003, New array monitors seismic activity near the Gulf of California in Mexico. *Eos*, 84, 4, 29-32.
- Vacquier V., Whiteman R.E., 1973, Measurements of faults displacement by optical parallax. *J. Geophys. Res.*, 78, 858-865.

Bottom topography, recent sedimentation and water volume of the Cerro Prieto Dam, NE Mexico

Vsevolod Yutsis*, Konstantin Krivosheya, Oleg Levchenko, Jens Lowag, Héctor de León Gómez and Antonio Tamez Ponce

Received: July 07, 2012; accepted: April 16, 2013; published on line: December 11, 2013

Resumen

La presa Cerro Prieto, relativamente una pequeña reserva de agua en el noreste de México, es uno de los principales recursos de agua potable para Monterrey, ciudad con una población cerca de cuatro millones de habitantes. Se llevó a cabo un estudio de sísmica de alta resolución en esta reserva de agua con un equipo SES-2000 que utiliza un efecto acústico paramétrico no lineal. La interpretación de los datos de acústica de alta resolución muestra que el espesor de los sedimentos recientes alcanza 3.5-4.0 m debido a la sedimentación del embalse. Esto demuestra una alta velocidad de sedimentación reciente (de 1-2 hasta 14 cm por año). Con base a los resultados de este estudio, se ha preparado un mapa batimétrico y un modelo de espesores de sedimentos. Se reveló una diferencia significativa (5-12%) entre el valor de la capacidad de volumen calculado por la Comisión Nacional del Agua (CNA) y los resultados acústicos. La diferencia entre dichos datos indica pérdidas de almacenamiento de 12-17 hasta 30 millones de metros cúbicos. Los resultados obtenidos de un estudio como éste, son útiles para mejorar un sistema de gestión de los recursos hídricos.

Palabras clave: acústica no lineal, NE de México, reserva de agua, topografía del fondo, capacidad de agua, sedimentación reciente.

Abstract

The Cerro Prieto dam, a relatively small water reservoir in NE Mexico, is one of the main resources of potable water for Monterrey, a city with a population of about four million inhabitants. A high resolution seismic study using non-linear parametric sub-bottom echo-sounder SES-2000 was carried out in this water reservoir. High resolution acoustic data interpretation shows that the thickness of recent sediments due to siltation of the reservoir reaches 3.5-4.0 m. It shows a high recent sedimentation rate (1-2 up to 14 cm/year). Based on the echo-sounder data, the first bathymetric map and a digital model of recent sediment thickness were designed. A significant (5-12%) difference between the volume capacity value used by National Commission of Water (CNA) and acoustic survey results was revealed. Differences between the CNA and acoustic data indicate storage losses from 12-17 up to 30 million cubic meters. The results obtained through study such as this one, could be useful to improve a water resources management.

Key words: non-linear acoustic method, NE Mexico, water reservoir, bottom topography, water capacity, recent sedimentation.

V. Yutsis*
K. Krivosheya
Universidad Autónoma de Nuevo León
Facultad de Ciencias de la Tierra
Carretera a Cerro Prieto km 8
Linares, 67700, N.L., México
**Corresponding author: vyutsis@hotmail.com*

V. Yutsis
Instituto Potosino de Investigación Científica y
Tecnológica, A.C.
División de Geociencias Aplicadas
Camino a la Presa San José 2055
Lomas 4ª. Sección, 78216
San Luis Potosí, S.L.P., México

O. Levchenko
P.P. Shirshov Institute of Oceanology
Russian Academy of Science, 36
Nahimovsky prospect
Moscow, 117997, Russia

J. Lowag
Innomar Technologie GmbH
Schutower Ringstrasse 4, 18069
Rostock, Germany

H. de León Gómez
Universidad Autónoma de Nuevo León
Facultad de Ingeniería Civil
Avenida Universidad s/n
Cd. Universitaria, San Nicolás de los Garza
66451, Nuevo León, México

A. Tamez Ponce
Posgrado de la Facultad de Ciencias de la Tierra
Universidad Autónoma de Nuevo León
Carretera a Cerro Prieto km 8
Linares, 67700, N.L., Mexico

Introduction

The role of bathymetry and recent sedimentation in water reservoir management is very important (Bowen, 1982), especially in the case of semi-arid countries (Annandale, 1987; Martínez *et al.*, 2010; Schleiss, 2008). Due to its physiography, the State of Nuevo León in North-East Mexico is characterized by semi-arid climate, undeveloped drainage, mostly low precipitation, and high evapotranspiration rates, as well as rapid demographic growth. Due to these characteristics, domestic water supply shortages have been occurring since 1979, making this a major problem for the state government. Monterrey, the most important industrialized city in the state with a population of about four million inhabitants (INEGI, 2009), faces a serious water supply scarcity (Navár, 2001; Navár, 2004). At present, ground water sources (Campo de Pozos de Mina, Sistema Santa Catarina, Sistema Santiago I, and Campo de Pozos Monterrey) and superficial waters (La Boca, Cerro Prieto and El Cuchillo dams) form the main water supply. The overall water supply demand for Monterrey city is calculated as a daily amount of 370 liters per capita, with an additional 17 m³/s required for domestic, industrial and city usage. Yet the actual supply is about 11 m³/s, i.e. city demand is short of about 6 m³/s (De León-Gómez, 1993; De León-Gómez *et al.*, 2004; De León-Gómez *et al.*, 2006).

The Cerro Prieto dam was built in a two years period (1980-1982) by the Secretaria de Agricultura y Recursos Hidráulicos (SARH) now known as National Commission of Water (Comision Nacional del Agua, CNA). The dam is located 130 km southeast of Monterrey and 20 km northeast of Linares. Cerro Prieto dam belongs to the regional system of water supply known as Linares-Monterrey. The storage capacity of the dam was calculated as almost 400 million m³ (De León-Gómez, 1993). The main objectives for the construction of this dam were to supply 4.1 m³/s of water for city of Monterrey, to irrigate 673 hectares, and to control peak discharge during hurricane seasons. The hydrological basin has an area of 1708 km² and is influenced by the southeastern part of the Monterrey Salient (Sierra Madre Oriental) and the northeastern part by the "Planicie Costera del Golfo Norte" (Coastal Plane, see Figure 1). The main sources are the Pabillo and Camacho rivers.

Concerns exist about the future of many Mexican reservoirs which are prone to soil erosion and subsequent siltation produce losses in storage capacity. Additionally, the number of studies of these problems is poor. Lake Cerro Prieto shares this problem with most impoundments in Nuevo León State.

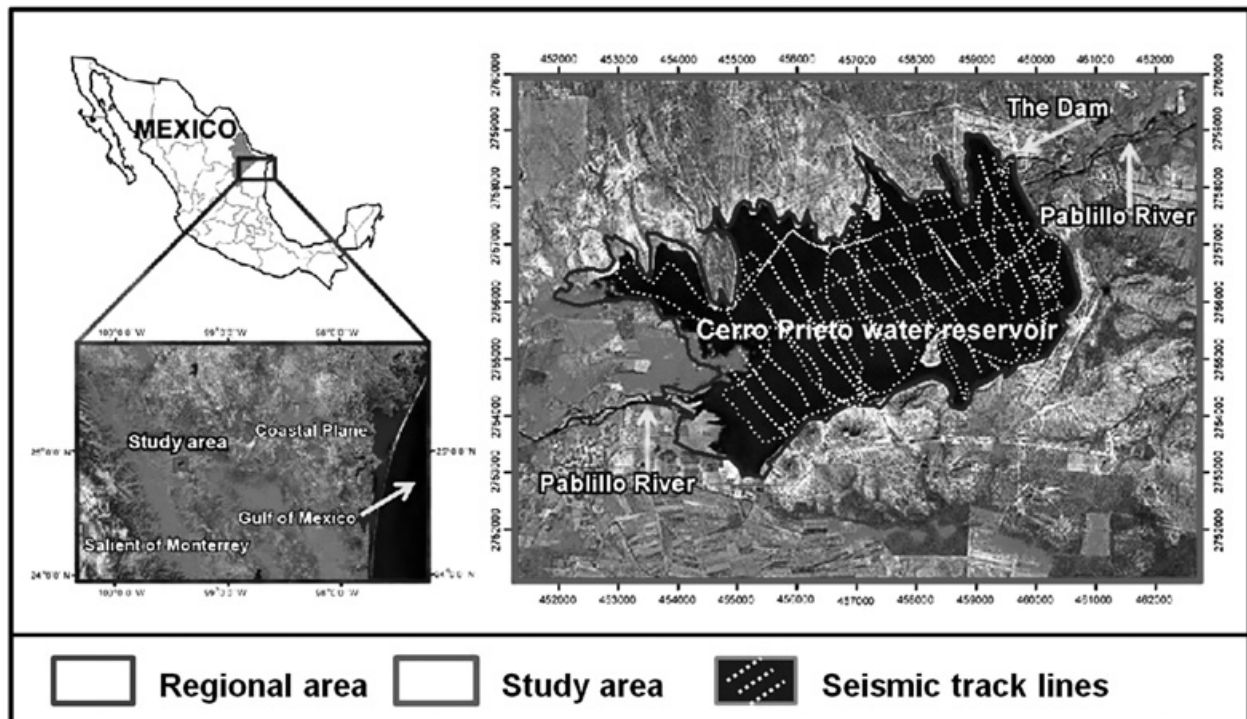


Figure 1. Overview map and location of the Cerro Prieto water reservoir area (river Pabillo valley) and the position of the acoustic lines.

The first step of the integral geological study of the Cerro Prieto water reservoir was geophysical prospecting including gravity, magnetic, electrical and shallow (onshore) seismic methods (Izaguirre Valdez, 2008; Yutsis *et al.*, 2009). It was oriented to recognition of sedimentary and upper basement structures of the Cerro Prieto area. As a follow-up to the earlier study, new research has been focused on the question whether recent sediments of artificial basins are significant and whether the volume of recent sediments affects the reservoir volume? If so, what are the consequences for water supply?

The objective of this study is to conduct a detailed bathymetric and geo-acoustic survey of the artificial reservoir in order to: (1) obtain an accurate map of Lake Bathymetry (depth) and reservoir volume values, and (2) study the distribution, thickness and volume of recent sediments in the reservoir.

Various ways could be used for this purpose. They are time-lapse bathymetry survey or some traditional tools like coring (Helsel and Hirsch, 2002; Anderson, 1986; Jones, 1999) and/or geophysical studies (Bièvre, 2005; Kirsh, 2006; Mainali, 2007; Rubin *et al.*, 2006; Sharma, 2002). The present study applies a geo-acoustic tool (a non-linear parametric sub-bottom echo-sounder) combined with typical techniques of geophysical survey. It is shown that high resolution seismic profiling is useful to quantify sedimentation rates and reservoir storage loss effectively. Especially it should be useful for initial studies of reservoirs where no previous bathymetry or bottom topography maps exist.

Data collection

Sedimentation of artificial reservoirs tends to be low. For example, a sedimentation rate of 1-2 cm/year causes a total accumulation of about 20-40 cm for 20 years of the reservoir operation. In order to be effective, new techniques for the estimation of sedimentation (such as acoustic equipment) should be able to provide a high vertical resolution.

Non-linear parametric acoustics equipment

In this study, we used the SES-2000 parametric (non-linear) dual frequency echo-sounder. The instrument simultaneously transmits two signals of slightly different high frequencies; their interaction creates a new low frequency signal. It has a large bandwidth and a short signal length, which allows good use in very shallow water and results a high (~15 - 20 cm) vertical resolution (Missiaen *et al.*, 2008) at acceptable sub-bottom penetration up to 10 m or more. Some favorable near sub-bottom seismic and geological conditions permit to achieve a vertical resolution up to 10 cm.

Parametric (non-linear) sound generation allows designing acoustical systems with small transducer dimensions and narrow sound beams at low frequencies. An Innomar SES-2000 parametric transducer has an active area of 20 by 20 cm and provides a beam width of less than four degrees (at 3dB), valid for all adjustable low frequencies between 5kHz and 15 kHz (Wunderlich and Müller, 2003). The transmit directivity of the parametric sound beam does not show any significant side lobe characteristic, which reduces ambiguities during the interpretation of individual reflectors. Short transmit signals of single sinusoidal cycles without any ringing and high ping rates of up to 50 pings per second are further advantages. They contribute to a high spatial resolution of this acoustical system and permit to apply it in a shallow basin.

Innomar's software tool ISE provides near real-time processing of the collected SES data. The operation procedure can be tuned on-line. A value of the sound velocity in water is used to convert sound travel time to the depth. The depth values are screened online.

Some advantage of the SES-2000 parametric (non-linear) dual frequency echo-sounder is the survey of small water reservoirs, which often requires the collection of sub-bottom data from small boats in water depths of down to one meter and to resolve thin layers of recent sedimentation due to damming. Furthermore, the determination of near surface structures, e.g. shallow fault zones, is of interest at the same time and can be achieved with the application of such a mobile parametric profiler system (Wunderlich and Wendt, 2001; Vasudavan *et al.*, 2007; Wunderlich, 2007).

Data acquisition methodology

The aquatic survey of the Cerro Prieto water reservoir was conducted on-board of a small motor boat (5 m). The SES-2000 transducer was mounted on the front side of the boat 0.75 m down from the water level using a light metal pipe, and all electronic equipment was installed on the deck. Accurate positioning of the boat was reached using Global Positioning System (GPS). Average speed was 8-10 km/h.

A total of 32 acoustic profiles have been acquired. The track map is shown at the Figure 1. Line separation is about 300 m. Twenty six profiles were made at near right angles to the axis of the basin. Five lines were oriented along the river Pablillo valley and finally one profile was made circular, skirting the shoreline. Some lines have been repeated to provide the quality control. Difference in depth measurement for different data sets does not exceed $\pm 2-5$ cm.

A sound velocity profile in the lake was not taken. Acoustic depth measurements were calibrated by direct depth measurements (at some points) at different parts of the lake.

Results and discussion

As it is mentioned above the water depth and sediment layer thickness are calculated from sound pulse travel times. The water sound velocity mean value of 1450 m/s was used (Kinsler *et al.*, 1991). Velocity uncertainty is evaluated of 0.5-1%. Calibration of acoustic bottom depth for some points allows us to obtain the depth accuracy $\pm 10-20$ cm. This is limited mainly by weather conditions. The same velocity value was used for sub-bottom sediments. It is supposed velocity uncertainty of 3-4%. For mean value of sediment thickness 50 cm the velocity uncertainty of 4% corresponds to ± 2 cm of thickness uncertainty. Uncertainties of sediment velocity of 3-4% for 3-4 m sediment layer thickness could cause $\pm 12-15$ cm variations.

Integral model based on CNA data of water balance and lake surface area allows evaluating storage loss due to uncertainties of water sound velocity (maximum $\pm 8 \times 10^6$ m³ for 4% and

$\pm 2 \times 10^6$ m³ for 1 %). For this study estimated sound velocity uncertainty is about 0.5%, which corresponds to maximum volume loss $\pm (1-1.5) \times 10^6$ m³. The value ± 5 cm of sediment thickness uncertainty corresponds to $\pm (0.6-1.4) \times 10^6$ m³ of uncertainty of sediment volume.

Acoustical reflectors on the depth sections have been picked and digitized. Digital data sets of the bottom depth and the depth of the base of recent sediments (the acoustic basement depth) were used to generate the bathymetric model, the model of sediment thickness and to calculate water storage volume.

Bathymetry and bottom morphology

Acoustical sections provide detailed information of bottom morphology and sub-bottom sediments. Figure 2 and Figure 3 show typical echo-plot samples. Figure 2 shows a fragment of the circular profile, which is located in the western part of the lake. This is a relatively shallow part of the water reservoir. The depth of the bottom is not more than 4-6 meters. In general, the bottom is relatively smooth (Figure 2c), but in places the detailed topography is somewhat complex and irregular (Figures 2a, 2b).

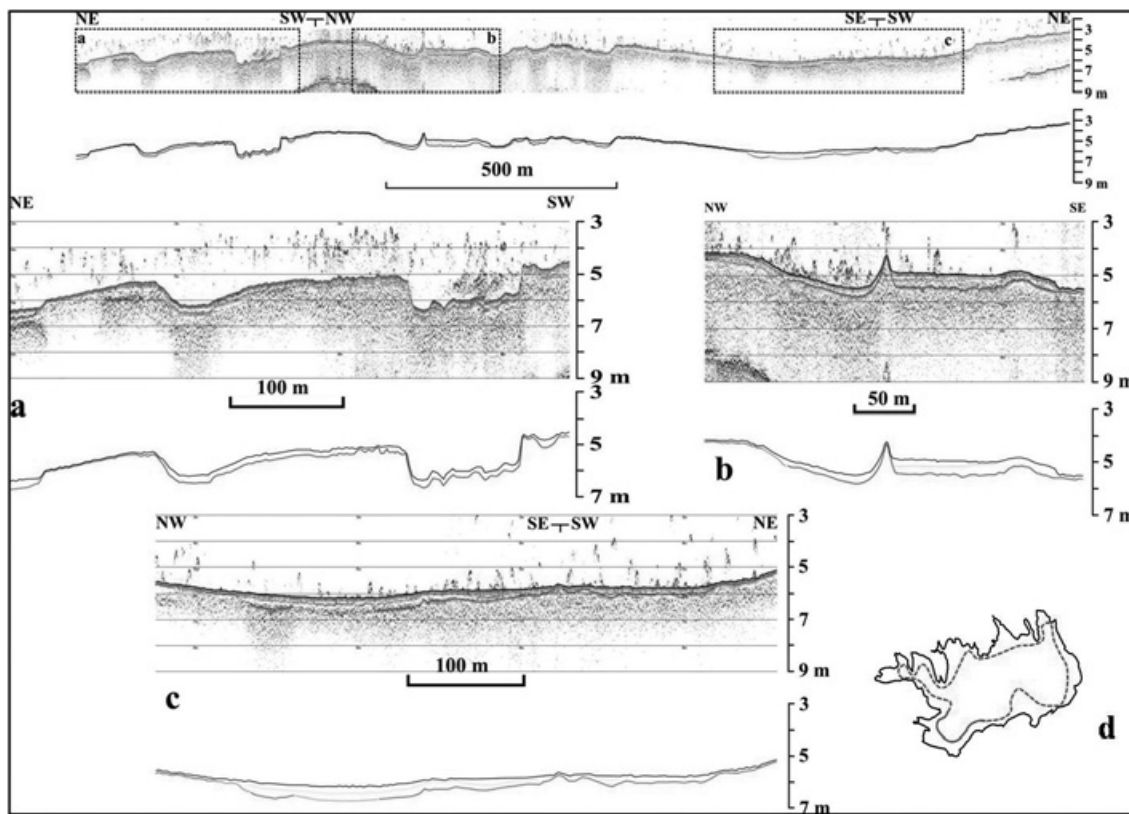


Figure 2. Example of dual frequency echo-sounder (acoustic) data. Fragment of the circular profile at the western shallow part of the Cerro Prieto water reservoir: (a) irregular (erosional) bottom relief and recent sediments thickness from zero to 25-30 cm; (b) sharp peak of the relief; (c) smooth topography and recent sediments thickness up to 0.75 cm; (d) the fragment (solid) and complete circular line (dashed).

Figure 3 shows an acoustic line, which is situated in the eastern deep part of the Cerro Prieto Lake crossing the ancient river Pablillo valley in NW-SE direction. The water depth here is calculated as 18-24 m (Figure 3a). In this area the bottom is mainly smooth. A small trough extending in WSW-ENE direction is shown at Figure 3b. The trough bottom depth is more than 28 m, and width ranges 40-60 m (Figure 3b).

It is observed significant difference (up to 5-7 m) between acoustical depths and a previous topographic map. It is supposed that the original topography (land surface) has been changed and the river Pablillo valley has been deepened during construction of the dam (De León, 1993, Figure 4). The previous topographic map by Instituto Nacional de Estadística y Geografía (INEGI) (INEGI, 1980) demonstrates the smoothed topography features of the area. They are the undulating surface of the river Pablillo valley at the elevation between 252-310 m (Figure 6). The bathymetric survey with the SES-2000 parametric echo-sounder has resulted in a modification of some important aspects of this map and, also, in the construction of the first bathymetric map of the Cerro Prieto water reservoir (Figure 7).

The irregular bottom topography of the reservoir is revealed. Taking into account that the water surface was at the altitude of 282 m above sea level during acoustic study, the depth of the reservoir ranges from 0.0-1.0 to 28 m (Figures 6, 7). Figure 7 shows the general topography of the Cerro Prieto Lake bottom based on survey results in combination (co-kriging) with the Digital Elevation Model (The Consortium for Spatial Information, 1980).

It is possible to recognize two different areas in the lake basin. The western shallow-water area is largely occupied by a flat bottom (depth 0.5-10 m), except for a bottom elevation trending in the northeastern direction. The elevation has a relative height of about 2-3 m from the bottom of the lake. The western area is divided into NE and SW regions. To the southeast of the elevation, a smooth floor tends to be gently inclined from its peripheral parts towards the east. The North of the western area is characterized by relatively low relief (up to -12 -13 m) and tends to be deeper toward southeast (Figure 7).

A chain of islands is located in the central part of the water reservoir. The large island called

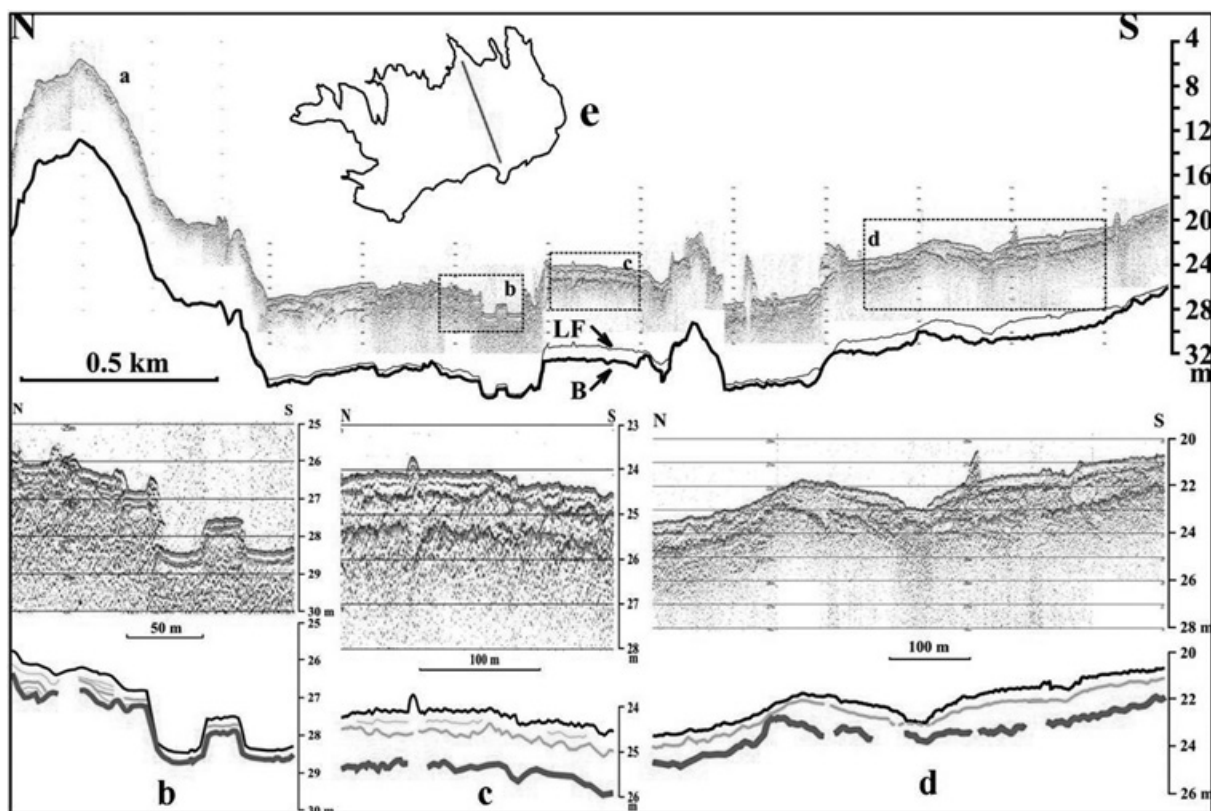


Figure 3. Example of the acoustic profile situated in the eastern deep area of the Cerro Prieto water reservoir: (a) irregular bottom topography and variation of sediment thickness; (b) small depression (trough) in the central part of the line; (c) smooth bottom topography and layered sediments of 1.5 meters thickness; and (d) smooth bottom and wavy sub-bottom topography. LF – Lake Floor; B – acoustic basement; (e) position of the acoustic line.

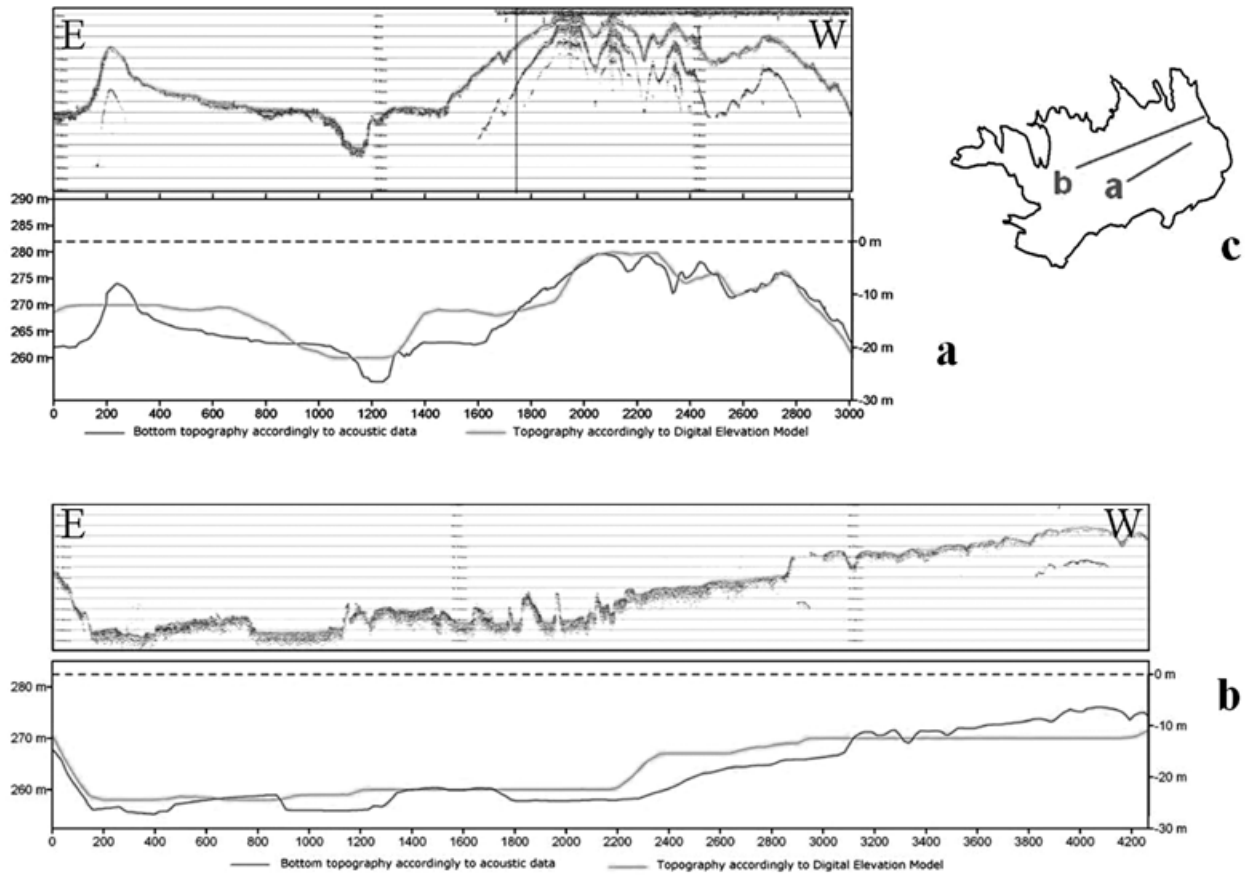


Figure 4. Comparison between the depths of the bottom, calculated from the acoustic data, and surface topography, extracted from the Digital Elevation Model (DEM). The difference reaches 5-7 m.; (c) position of the acoustic lines. Horizontal scale is shown in meters (m).

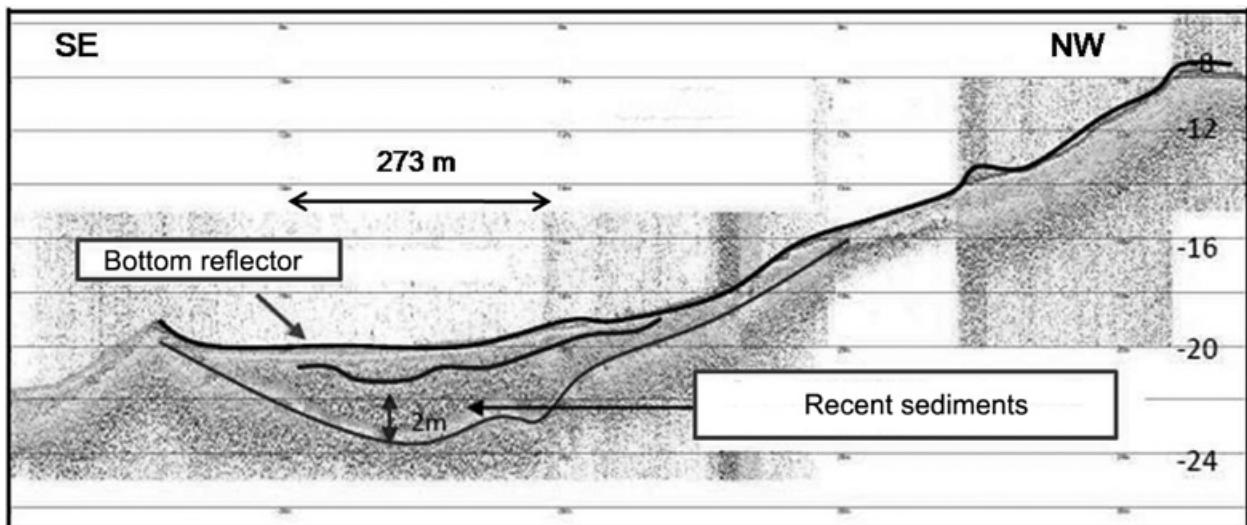


Figure 5. Example of echo-sound record which shows thickness of recent sediments about 4 m.

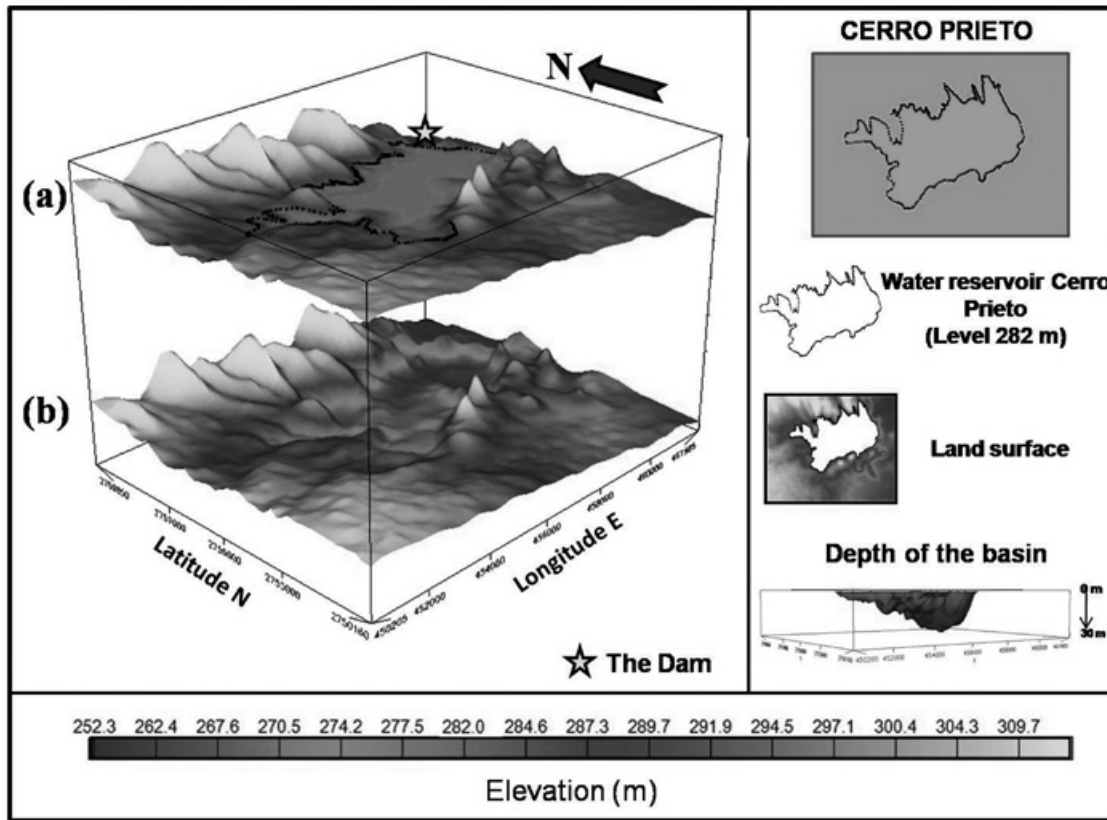


Figure 6. Block-diagram of the Cerro Prieto water reservoir and adjacent areas (river Pablillo valley).

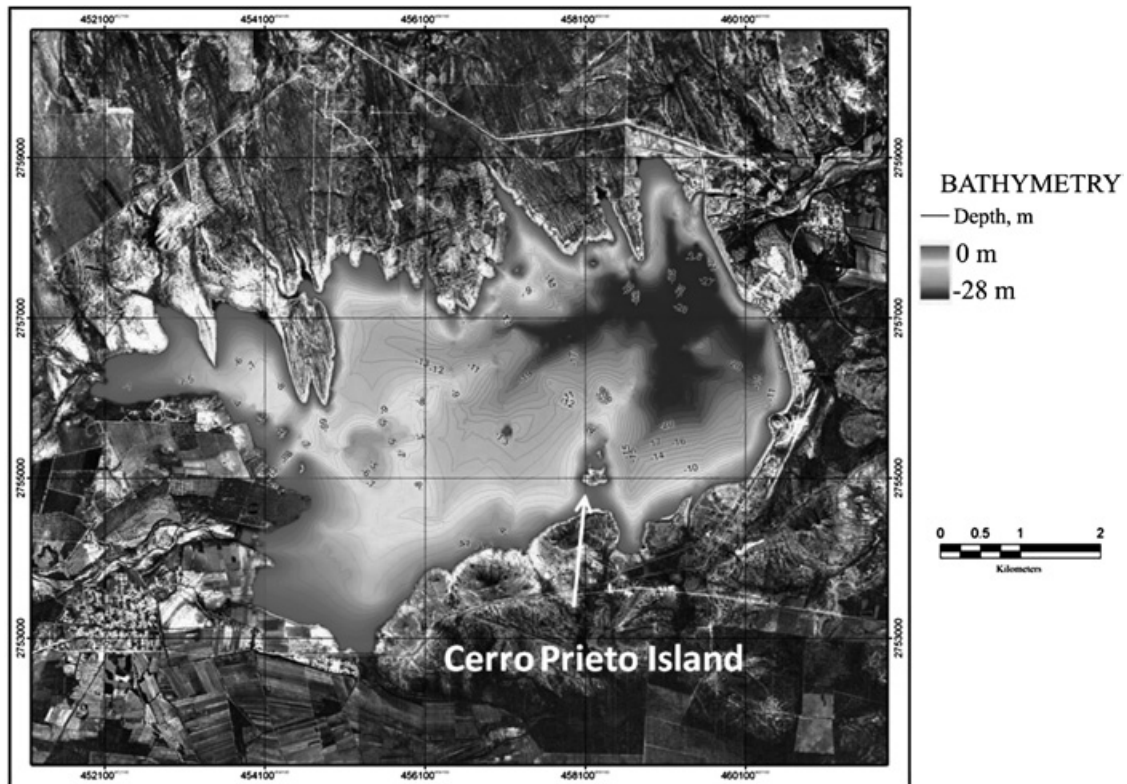


Figure 7. Bathymetric map of the Cerro Prieto water reservoir (water level at the dam is 282 m above sea level). Seismic track lines are shown at the Figure 1.

the Cerro Prieto Island, and rises up to 25-30 m above the surrounding bottom floor near the south coast (Figures 7). Another one situated to the west-northwest and has a single pointed peak. An area of four small islands occurs to the north of the Cerro Prieto Island, topographic high which divides the water reservoir into western and eastern areas.

The eastern deep-water area is situated to the northeast of the Cerro Prieto Island (Figure 7). It is characterized by irregular topography. The bottom depth is generally more than 15-20 m and attains a maximum depth of approximately 28-30 m (Figure 7). So the deepest part of this area occupies the easternmost region which is situated near the dam and artificial dykes. At the southeastern part of the lake the basin bottom lies at a depth of between 22-24 m, interrupted by small bottom hills in some places.

Recent sedimentation

Recent sediments of the Cerro Prieto water reservoir have been deposited on the floor of river Pablillo valley for about 28 years. In case of recent non-consolidated sediments (case of Cerro Prieto dam) we have some kind of pulp, or suspension of fine particles (silt, mud), and it is supposed that

usually the silt has a velocity the same (or slightly less) as the water.

The interpretation of the SES profile at the western shallow-water area (Figure 2) shows two reflectors. We identify a strong sub-bottom reflector distributed almost throughout the whole lake as the most likely base of recent sediments. We also identify a few hypothetical bright seismic sub-bottom facies, which we attribute to recent "lake" sediments, quaternary river "pre-lake" sediments (alluvium), and cretaceous bed rocks. The uniform thinness of the upper acoustic unit for the whole basin is more relevant for new "lake" sediments than for alluvium. The quaternary river sediment thickness demonstrates essential variability around the water reservoir. In the western part of the lake the thickness of this layer is usually less than 1 meter. Most of the profiles here show a sediment thickness of 30-50 cm or, even, an absence of sediments. At the eastern deep part of the Cerro Prieto Lake thickness of recent sediments is 1.0 – 1.5 m (Figures 3c, 3d). The maximum thickness values are from 3.5 up to 4.0 m (Figures 5, 8). It may be partly caused by a sub-water slumping process or redistribution of sediments (Figure 5). And it means the maximum sedimentation rate could be over 14 cm/year.

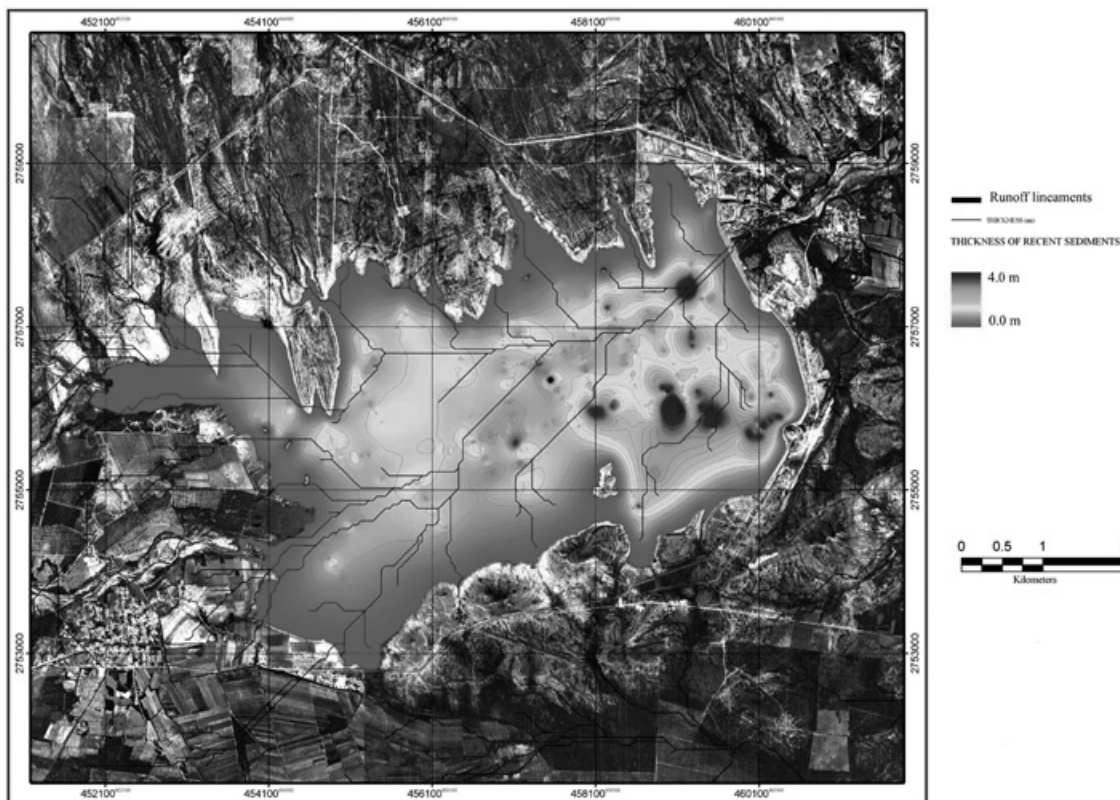


Figure 8. Thickness of the recent sediments and GIS-designed digital model of runoff lineaments.

Recent sediment thicknesses obtained from the interpretation of non-linear acoustic have been mapped (Figure 8). Sediment thickness within the lake basin varies from zero to over 3.5 m. There are five centers of sediment accumulation localized in the eastern deep area. The greatest thicknesses occur in narrow bottom valleys (troughs) in the central and eastern parts of the lake (Figures 7, 8).

The sediments in the basin are generally confined to the southeastern part of the lake. The western area is relatively shallow and the sediments are thin (0-0.5 m). It means that average rate of the siltation is up to 1-2 cm/year.

The river Pablillo is the main source of water and sediments for the basin. So, it seems rather strange that the western part of the lake near river mouth does not show a large amount of sediments. We hypothesize that sediments are mainly fine grained (silt), deposited slowly and distributed by water currents uniformly through the basin.

The total volume of this accumulated material estimated by the acoustic data is approximately 8.8 ± 0.5 million cubic meters. It is possible to suppose that some recent sedimentary layers (bodies) are not reflected on the acoustic records. This means that the volume of the acoustically visible sediments could be less than the real (total) volume of sediments.

Water storage

Analysis of the storage volume was conducted using three data sets: the Digital Elevation Model of Cerro Prieto and surrounding area (The Consortium for Spatial Information, 1980), a register of the water balance of Cerro Prieto dam, and new data of the high resolution acoustic survey.

According to CNA reports the maximum water storage of the Cerro Prieto water reservoir is 393 million of cubic meters, which corresponds to a water level of 285 meters above sea level (a.s.l.) (see Table 1, volume CNA). However, this level was reached only three times after the dam's construction. Hurricanes Gilbert (1988), Keith (2000), and Emily (2005) contributed to reach the full capacity storage of the dam.

Table 1 shows summary data of the water storage of the lake and the surface area of the reservoir for different water levels, calculated according to the Digital Elevation Model (DEM) and SES echo-sounding data. The procedure comprises a standard hydrological modeling (implemented in Arc/Info) that is a cell-based modeling of water depth and storage volumes (Stout *et al.*, 1985). In both procedures the Digital Elevation Model for Linares and surrounding areas from INEGI (Instituto Nacional de Estadística, Geografía, e Informática) was used. Grid node spacing was 30 x 30 m.

Table 1. Water volume (storage capacity) and area of the water reservoir according to echo-sounding data (SES), Digital Elevation Model (DEM) and National Commission of Water (CNA).

H, m	Volume DEM, x10 ⁶ m ³	Area DEM, km ²	Volume CNA, x10 ⁶ m ³	Area CNA, km ²	Volume SES, x10 ⁶ m ³	Area SES, km ²
285	278.743	26.95	393.000	-	360.000*	-
284	252.249	26.06	344.375	31.60	320.000*	-
283	226.664	25.16	313.529	29.50	292.000*	-
282	202.033	24.15	285.789	27.50	268.348	21.15
281	178.503	22.99	259.474	25.67	244.858	21.15
280	156.396	21.24	233.500	23.93	221.379	21.15
279	139.065	16.61	210.000	22.20	198.022	21.09
278	123.513	15.01	188.800	20.67	175.143	20.74
277	109.240	13.88	169.231	19.23	153.311	19.53
276	96.197	12.68	150.714	17.76	133.619	17.52
275	83.875	12.01	133.833	16.42	116.045	15.84
274	72.181	11.39	117.857	14.97	100.748	13.66
273	61.115	10.77	103.571	13.67	87.367	12.30
272	50.647	10.18	92.571	12.73	75.316	11.20

360.000* values simulated

The volume capacity values (Figure 9) derived from the analysis of the bathymetric map (Figure 7) indicate a predicted total storage capacity of 360 million m³ (Table 1), whereas the storage capacity generated from DEM shows only 279 million m³. This discrepancy could be explained by the fact that the Digital Elevation Model was developed in the early 80-ies before the dam construction and excavations of the basin material as reported by De León (1993) (Figure 4).

The volume of water, mentioned in the report of CNA, is approximately (12-17) ±2 million m³ larger than the amount calculated from the SES data for operation levels 280-275 meters respectively (Table1). This can be explained by recent sedimentation.

There is a difference between the loss in storage capacity and calculated sediment volume (8.8 ± 2 million cubic meters). It is possible supposed that calculated sediments could be underestimated. Nevertheless, the observed difference in calculated sediment volume (8.8 million m³) and loss in observed storage capacity (12-17 million m³) changes the average sedimentation rate a little (from 1.5 up to 2 cm/year).

The trend line of water volume (simulation) shows that sediment accumulation between 1982 and 2009 in the Cerro Prieto Lake could result a loss up to 30 million m³ of storage capacity (Table 1, Figure 9) for maximum operation level (285 m a.s.l.). And 17 million m³ for low operational level (275 m) is more critical. It corresponds to storage loss 19% of total volume or 11-12 days water supply (four million inhabitants x 370 l/day).

Conclusions

This study discusses the advantage of geophysical data to evaluate the current state of water reservoir (distribution of recent sediments and real storage capacity).

Analysis of the non-linear echo-sounding data provides the volume of the reservoir at different levels of water table and the volume of sediments as well as distribution of the sediments through the basin.

A high rate of recent sedimentation (1-2 up to 14 cm/year) at the artificial water reservoir is revealed. Interpretation of the SES echo-sounding data shows that the thickness of sediments due to siltation of the reservoir reaches 2.5-4.0 m. The total volume of this accumulated material estimated by the acoustic data is evaluated about 9 million cubic meters.

The volume of water, calculated from the acoustic data for common operating levels is approximately 12-17 million cubic meters smaller than the values of operational management data. This is about 5-12 % of total storage capacity. A significant reduction in the size and volume of the reservoir is obvious. This factor could have been taken into account in the calculations of the volume of water for this reservoir.

Acknowledgements

The authors would like to thank Universidad Autónoma de Nuevo León (UANL), Mexico, for funding support of the project PAICYT CT-1705-07 and Innomar Technologie GmbH, Germany, who

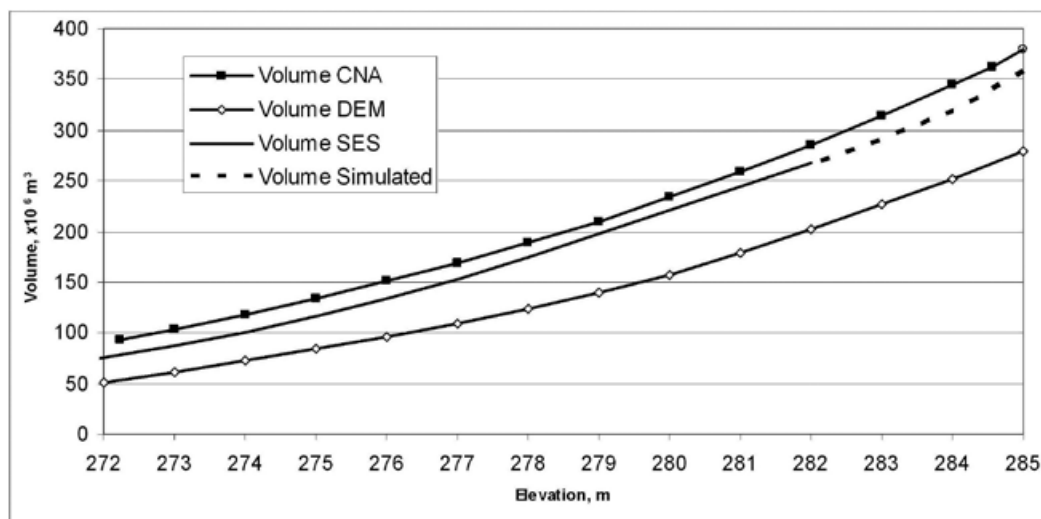


Figure 9. Different values of water capacity derived from three data sets: echo-sounding data (SES), Digital Elevation Model (DEM) and National Commission of Water (CNA).

kindly provided the SES-2000 compact equipment. We are indebted to Pedro Garza of National Commission of Water (Rio Bravo Division, Monterrey) for providing access to water balance data. Authors thank Dirk Masuch Oesterreich (UANL) for his assessment of GIS calculations. We also would like to thank Dr. John M. Sharp, Jr. (The University of Texas at Austin), Dr. Vadim Galkine (Canada) and Dr. Wouter Buytaert (Imperial College, Great Britain) for their constructive comments and suggestions, which helped to improve this paper. Comments and suggestions from two anonymous reviewers and the editor are greatly appreciated.

Bibliography

- Anderson R.N., 1986, Marine geology. Wiley & Son, 328 pp.
- Annandale G.W., 1987, Reservoir sedimentation. Elsevier, Amsterdam, 221 pp.
- Bièvre G., Norgeot Ch., 2005, On the use of geophysical methods for characterization of earth dams: A case study on the Canal du Centre (France). *Bulletin des Laboratoires des Ponts et Chaussées*, 254, 85-107.
- Bowen R., 1982, Surface water. Wiley Interscience Publ., New York & Toronto, 290 pp.
- Instituto Nacional de Estadística y Geografía (INEGI), 2009, Anuario estadístico de los Estados Unidos Mexicanos, <http://www.inegi.org.mx>. Cited 20 Sept 2010
- The Consortium for Spatial Information, 1980, Digital Elevation Model. <http://www.csi.cgiar.org>. Cited 12 Apr 2007.
- De la Garza-González S. I., 2000, Estudio geológico/hidrogeológico en la región citrícola (Linares-Hualahuises) Nuevo León, México. Tesis de licenciatura. Facultad de Ciencias de la Tierra, UANL, 131 pp.
- De León-Gómez, H., 1993, Die Unterlaufigkeit der Talsperre José López Portillo/Cerro Prieto auf einer Kalkstein-Mergelstein-Wechselfolge bei Linares, Nuevo León, Mexiko. Mitteilungen zur Ingenieurgeologie und Hydrogeologie 53, Aachen, 181 pp.
- De León-Gómez H., Schetelig K., Werner J., Azzam R., Masuch D., Medina-Barrera F., Rangel-Rodríguez M. M., Navarro-De León I., Salinas-Ramírez J. O., 1998, Water supply limit in the northeast Mexico, objective and scope. (SIREYES/95/053).- *Zbl. Geol. Paläont., Stuttgart*; Teil I, H 3-6, 511-518.
- De León-Gómez H., Medina Barrera F., Lizárraga Mendiola L., 2006, Elaboración de la matriz de geindicadores ambientales en la presa José López Portillo (Cerro Prieto), fuente superficial de abastecimiento de agua potable de Monterrey, N. L., México. *Ciencia UANL*, IX (1), 65-72.
- Helsel D.R., Hirsch R.M., 2002. Statistical Methods in Water Resources. In: Techniques of Water-Resources Investigations Book 4, Hydrologic Analysis and Interpretation, U.S. Geological Survey, Chapter A3. U.S. Geological Survey, 522 pp, <http://pubs.usgs.gov/twri/twri4a3/>, accessed March 2011.
- Izaguirre Valdez F.M., 2008, Estudio hidrogeofísico de la presa José López Portillo (Cerro Prieto), Noreste de México. Tesis de licenciatura, Universidad Autónoma de Nuevo León, Facultad de Ciencias de la Tierra, 192 pp.
- Jones E.J.W., 2004, Marine geophysics. Wiley & Son, 466 pp.
- Kinsler L.E., Frey A.R., Coppens A.B., Sanders J.V., 1991, Fundamentals of acoustics, Wiley and Son, 518 pp.
- Kirsch R., 2006, Groundwater geophysics. A tool for hydrogeology. Springer, Heidelberg, 493 pp.
- Mainali G., 2007, Monitoring of Tailings Dams with Geophysical Methods. Division of Ore Geology and Applied Geophysics, Luleå University of Technology, SE-97187 Luleå, Sweden, 93 pp.
- Marín-Córdova S., Campos-Enríquez O., Herrera-Moro-Castillo M., 2004, *Geofísica Internacional*, 43, 3, 435-443.
- Martinez S.E., Escolero O., Wolf L., 2010, Total Urban Water Cycle Models in Semiarid Environments — Quantitative Scenario Analysis at the Area of San Luis Potosi, Mexico. *Water Resources Management, DOI 10.1007/s11269-010-9697-6*.
- Missiaen T., Slob E., Donselaar M.E., 2008, Comparing different shallow geophysical methods in a tidal estuary, Verdrongen Land van Saeftinge, Western Scheldt, the Netherlands. *Netherlands Journal of Geosciences — Geologie en Mijnbouw*, 87, 2, 151-164.
- Navár J., 2001, Water supply and demand scenarios in the San Juan watershed. *Geofísica Internacional*, 40, 2, 121-134.

- Navár J., 2004, Water supply and demand in the lower Río Bravo/Río Grande basin: The irrigated agriculture scenario. *Geofísica Internacional*, 43, 3, 495-506.
- Rubin Y., Hubbard S.S., 2005, Hydrogeophysics. Springer, Heidelberg, 523 pp.
- Schleiss A., 2008, Reservoir sedimentation and sustainable development, in KHR ISI International Workshop "Erosion, Transport and Deposition of Sediments", 28 April 2008, Bern.
- Sharma P.V., 2002, Environmental and engineering geophysics, Cambridge University Press, 475 pp.
- Stout L.A., Harrington Jr. J.A., Grimshaw H.J., Shapiro G.L., 1985, Bathymetric changes in Overholser reservoir. *Proceedings of the Oklahoma Academy of Sciences*, 65, 69-72.
- Yutsis V.V., Jenchen U., de León-Gómez H., Izaguirre Valdez F., 2009, Paleogeographic development of the surroundings of Cerro Prieto water reservoir, Pablillo basin, NE Mexico, and geophysical modeling of the reservoir's subsurface. *Neues Jahrbuch für Geologie und Paläontologie*, 253, 1, 41-59.
- Vasudevan M., Sivakholundu K.M., 2007, Application of Parametric Acoustics for Shallow-Water Near-Surface Geophysical Investigations, in Abstracts of the OCEANS 2006 Asia-Pacific.
- Wunderlich J., 2007, Mobile parametric sub-bottom profiler systems for shallow and medium depth applications. *J. of the Acoustical Society of America*, 122, 5, 2983.
- Wunderlich J., Müller S., 2003, High-resolution sub-bottom profiling using parametric acoustics. *International Ocean Systems*, 7, 4, 6-11.
- Wunderlich J., Wendt G., 2001, Advantages of Parametric Acoustics for the Detection of the Dredging Level in Areas with Siltation, in Proc. of the 7th Workshop on Dredging and Surveying, Scheveningen: 67-75.

Use of Neural network to predict the peak ground accelerations and pseudo spectral accelerations for Mexican Inslab and Interplate Earthquakes

Adrián Pozos-Estrada*, Roberto Gómez and H.P. Hong

Received: September 09, 2012; accepted: June 11, 2013; published on line: December 11, 2013

Resumen

El uso de redes neuronales artificiales es explorado para predecir aceleraciones máximas del terreno y pseudoaceleraciones para sismos de tipo intraslab e interplaca. Un total de 277 y 418 registros sísmicos de dos componentes para sismos de intraslab e interplaca, respectivamente, son usados para entrenar los modelos de las redes neuronales artificiales con alimentación hacia adelante y con un algoritmo de aprendizaje de retroalimentación. Se consideran redes neuronales artificiales con una y dos capas ocultas. Con fines de comparación, valores de aceleración máxima del terreno y pseudoaceleración predichos con los modelos de las redes neuronales son comparados con los estimados mediante relaciones de atenuación o relaciones de movimiento fuerte. La comparación indica que los valores predichos, en general, siguen la tendencia de los valores obtenidos con las relaciones de movimiento fuerte. Sin embargo, se debe llevar a cabo una verificación extensa de los modelos entrenados antes que estos puedan emplearse en análisis de peligro y riesgo sísmico ya que, en ocasiones, los valores predichos no reflejan el comportamiento observado de los registros.

Palabras clave: red neuronal artificial, sismos de subducción, aceleración máxima del terreno, pseudoaceleración, México.

Abstract

The use of Artificial Neural Networks (ANN) is explored to predict peak ground accelerations (PGA) and pseudospectral acceleration (SA) for Mexican inslab and interplate earthquakes. A total of 277 and 418 seismic records with two horizontal components for inslab and interplate earthquakes, respectively, are used to train the ANN models by using an ANN with a feed-forward architecture with a back-propagation learning algorithm. Both ANN with single and two hidden layers are considered. For comparison purposes, the PGA and SA values predicted by the trained ANN models are compared with those estimated with attenuation relations or ground motion prediction equations (GMPEs). The comparison indicates that the predicted PGA and SA values by the trained ANN models, in general, follow the trends predicted by the GMPEs. However, an extensive verification of the trained models must be conducted before they can be used for seismic hazard and risk analysis since, on occasion, the PGA and SA values predicted by the trained ANN models depart from the behaviour observed from the actual records.

Key words: artificial neural network, subduction earthquakes, peak ground acceleration, pseudospectral acceleration, Mexico.

A. Pozos-Estrada*
Instituto de Ingeniería
Universidad Nacional Autónoma de México
Ciudad Universitaria
Delegación Coyoacán, 04510
México D.F., México
*Corresponding author: APozosE@iingen.unam.mx

R. Gómez
Instituto de Ingeniería
Universidad Nacional Autónoma de México
Ciudad Universitaria
Delegación Coyoacán, 04510
México D.F., México
E-mail: RGomezM@iingen.unam.mx

H.P. Hong
The University of Western Ontario
Department of Civil and Environmental Engineering
London, ON N6A 5B9
Canada
E-mail: hongh@eng.uwo.ca

Introduction

Artificial neural networks (ANNs) have been used in seismic engineering due to their flexibility to deal with highly nonlinear problems (Fausett, 1994). ANNs have been used to predict ground motion measures such as the peak ground displacement (PGD), peak ground velocity (PGV), or peak ground acceleration (PGA), and spectral acceleration (SA) (Günaydin and Günaydin, 2008; Kamatchi *et al.*, 2010). ANNs have also been used for generating artificial earthquakes and response spectra, and spectrum compatible accelerograms (Ghaboussi and Li, 1998; Lee and Han, 2002). More recently, Hong *et al.* (2012) showed that the prediction of the PGA and SA by using ANNs with a single hidden layer may not be robust, although it could be considered as an alternative to the commonly used attenuation relations or ground motion prediction equations (GMPEs). Estimation of PGAs for Mexican subduction earthquakes using the ANNs has been explored by García *et al.* (2007). However, the application of ANNs to predict SA for Mexican earthquakes has not been reported in the literature.

The main objective of this study is to investigate the applicability of ANNs to estimate PGA and SA for ground motion records caused by Mexican subduction earthquakes. Two sets of records of Mexican subduction earthquakes obtained at firm soil sites (*i.e.*, site class B according to the NEHRP (BSSC, 2004)) are used in training and qualifying ANNs. Training of the ANN models was carried out using a feed-forward architecture with

a back-propagation learning algorithm. Only single and two hidden layers are considered to minimize potential overfitting. The parameters considered in the input layer are: moment magnitude (M_w), closest distance to the fault (R_c) and focal depth (H), while the logarithm of the ground motion measures is used to represent the outcome from the output layer. The predicted PGA and SA values are compared with those estimated from GMPEs to assess the adequacy of the trained ANN models.

ANN Modeling

Description of the ANN modeling

The ANN modeling involves the selection of the number of neurons in the input as well as the hidden and output layers. In this study, the number of neurons in the input layer is considered to be 3, representing M_w , R_c and H as defined earlier. Single and two hidden layers (denoted by 1HL and 2HL, respectively) with multiple hidden neurons are used to approximate the mapping between the input and output layers. The output layer consists of a single neuron that represents the logarithm of the ground motion measures (PGA or SA) for a considered earthquake type and natural vibration period.

An illustration of an ANN model with multiple hidden layers and neurons is depicted in Figure 1, where neurons are weighted and transformed into output values. By considering two hidden layers, the mathematical expression of the output neuron in the output layer, y_{output} is given by,

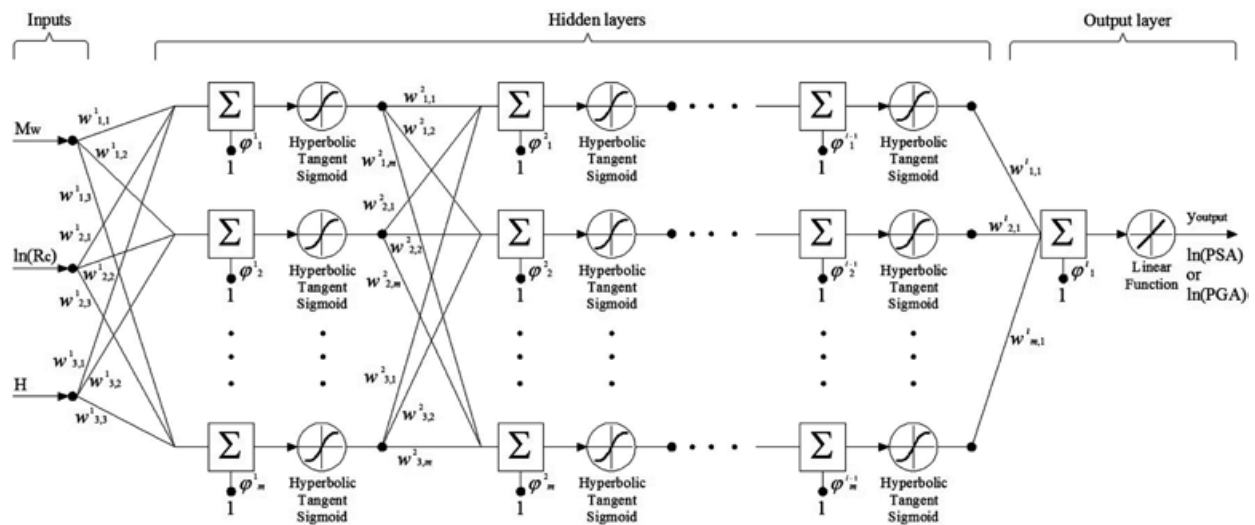


Figure 1. Sketch of an ANN model with multiple hidden layers and neurons.

$$y_{output} = f_3 \left(\sum_{k=1}^m [w_3]_{k,1} f_2 \left(\sum_{j=1}^m ([w_2]_{j,k} f_1 \left(\sum_{i=1}^n ([w_1]_{i,j} x_i + (\varphi_1)_j \right) + (\varphi_2)_k \right) \right) + (\varphi_3)_1 \right), \quad (1)$$

where n is the total number of neurons in the input layer; x_i is the i -th neuron in the input layer; $[w_1]_{i,j}$, $[w_2]_{j,k}$ and $[w_3]_{k,1}$ are the weights that optimize the mapping between the input and the first hidden layer, between the first and second hidden layer and between the second hidden layer and output layer, respectively; $(\varphi_1)_j$, $(\varphi_2)_k$ and $(\varphi_3)_1$ are the biases associated with the hidden and output layers; $f_1(\cdot)$, $f_2(\cdot)$ and $f_3(\cdot)$ are activation (or transfer) functions between the input and the first hidden layer, the first and the second hidden layer and between the second hidden layer and the output layer, respectively; and m is the total number of neurons in the hidden layers.

Two types of activation functions, namely, the tan-sigmoid function and the linear function are commonly used. These functions are expressed as,

$$f(x) = (e^x - e^{-x}) / (e^x + e^{-x}), \quad (2a)$$

and

$$f(x) = x, \quad (2b)$$

The former is often used as the transfer function between the input and hidden layers, while the latter is used as the transfer function between the hidden layers and the output layer. Following García *et al.* (2007), in the present study, Eq. (2a) is used as the transfer function between the input and hidden layer(s) and Eq. (2b) is used as the transfer function between the hidden layer(s) and the output layer.

Training ANN

The training of an ANN consists in the minimization of a predefined error function, in terms of observed and predicted output values, by varying the weights and biases. One of the algorithms used to train the ANN is the back-propagation (Fausset, 1994), where the error is propagated backward by adjusting the weights from the output to the input layer. The training can be summarized as follows:

1. Provide the ANN model with sample inputs and known outputs;
2. Evaluate an error function in terms of the difference between the predicted and observed output;
3. Minimize the error function by adjusting the weights and biases of all the layers from the output to the input layer.

For the numerical analysis to be presented in this study, the error function was defined as the mean square error (MSE). The minimization of the MSE (Step 3)) was carried out using the Levenberg-Marquardt algorithm (Marquardt, 1963; Press *et al.*, 1992) that is incorporated into the back-propagation algorithm and implemented in Matlab (Hagan and Menhaj, 1994).

Strong ground motion database and GMPEs

The strong ground motion database employed to develop the ANNs model consists of 695 strong ground motion records, each one with two horizontal components at firm soil sites (class B according to NEHNP -BSSC, 2004) compiled by García *et al.* (2005, 2009). There are 277 inslab records and 418 interplate records for the events shown in Figure 2 and listed in Table 1. There are 16 intermediate-depth normal-faulting inslab events with M_w within 5.2 to 7.4 and 40 interplate events with M_w ranging from 5.0 to 8.0. The distribution of M_w and H with respect to R_c is presented in Figure 3. A baseline correction and a high-pass filter with cut-off frequencies of 0.05 Hz for events with $M_w > 6.5$ and 0.1 Hz for the rest events were applied to all the records. The selection criteria of the records can be found in García *et al.* (2005, 2009). The same strong ground motion database was also employed by Hong *et al.* (2009) to develop GMPEs based on the geometric mean (i.e., for a random orientation). As these GMPEs will be used to compare with those predicted by the ANN model, the adopted functional forms and the obtained regression coefficients in Hong *et al.* (2009) are summarized below.

The functional form of the GMPEs for inslab earthquakes is the one given by García *et al.* (2005), which can be written as,

$$\log_{10} Y = c_1 + c_2 M_w + c_3 R - c_4 \log_{10} R + c_5 H + \varepsilon, \quad (3)$$

where Y (cm/s²) represents the PGA or SA values, c_i , $i = 1, \dots, 5$, are the model parameters, M_w is the moment magnitude, $R = \sqrt{R_{cld}^2 + \Delta_0^2}$, R_{cld} (km) is the closest distance to the fault surface for events with $M_w > 6.5$, or the hypocentral distance

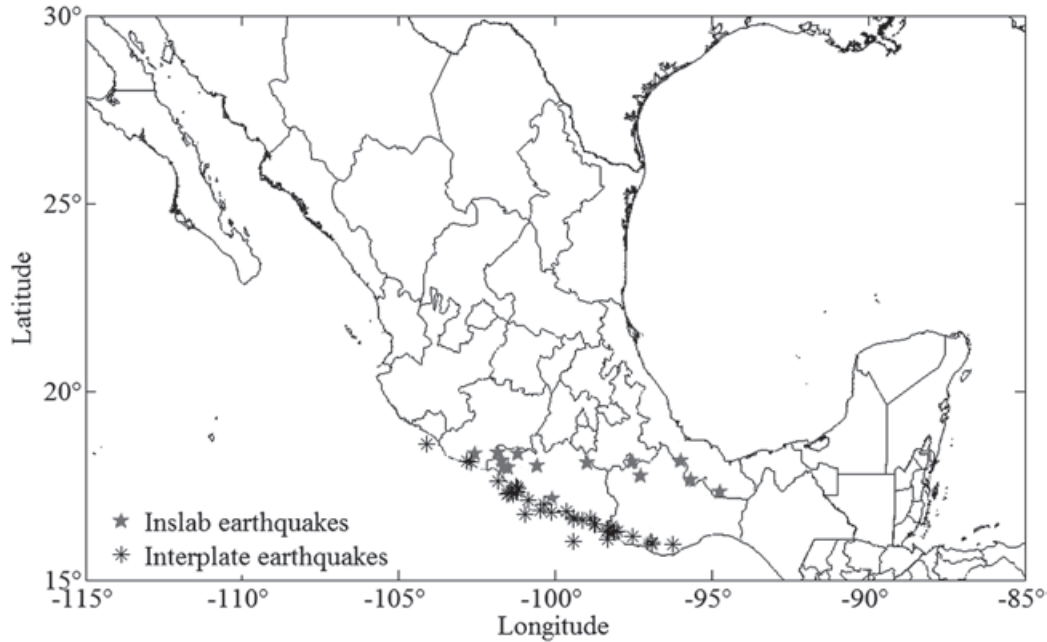


Figure 2. Location of events for the considered records.

Table 1. Inslab and interplate events used in training the ANN models.

Inslab earthquake				Interplate earthquake			
Event No.	No. of Rec.	Date (dd/mm/yy)	Mw	Event No.	No. of Rec.	Date (dd/mm/yy)	Mw
1	6	23/02/94	5.8	1	10	19/09/85	8
2	21	23/05/94	6.2	2	8	21/09/85	7.6
3	16	10/12/94	6.4	3	9	08/02/88	5.8
4	22	11/01/97	7.1	4	6	10/03/89	5.4
5	18	22/05/97	6.5	5	10	25/04/89	6.9
6	15	20/04/98	5.9	6	5	02/05/89	5.5
7	30	15/06/99	6.9	7	8	13/01/90	5.3
8	16	21/06/99	6.3	8	6	11/05/90	5.5
9	26	30/09/99	7.4	9	9	31/05/90	5.9
10	14	29/12/99	5.9	10	6	15/05/93	5.5
11	21	21/07/00	5.9	11	12	24/10/93	6.6
12	21	05/03/01	5.3	12	15	14/09/95	7.3
13	23	06/03/01	5.2	13	10	13/03/96	5.1
14	13	30/01/02	5.9	14	9	27/03/96	5.4
15	9	17/01/04	5.4	15	17	15/07/96	6.6
16	6	20/04/04	5.6	16	10	18/07/96	5.4
				17	12	21/01/97	5.4
				18	7	16/12/97	5.9
				19	12	09/05/98	5.2
				20	10	16/05/98	5.2
				21	15	05/07/98	5.3
				22	12	11/07/98	5.4
				23	14	12/07/98	5.5
				24	10	04/09/01	5.2
				25	11	10/11/01	5.4
				26	10	07/06/02	5.2
				27	12	07/06/02	5.5
				28	12	19/06/02	5.3
				29	7	05/08/02	5.4
				30	10	27/08/02	5.0
				31	6	30/08/02	5.2
				32	15	25/09/02	5.3
				33	10	08/11/02	5.2
				34	8	10/12/02	5.4
				35	15	10/01/03	5.2
				36	8	22/01/03	7.5
				37	15	01/01/04	6.0
				38	11	01/01/04	5.6
				39	8	06/02/04	5.1
				40	18	14/06/04	5.9

for the rest, $\Delta = 0.0075 \times 10^{0.507M_w}$ is a near-source saturation term defined by Atkinson and Boore (2003), H (km) is the focal depth, and ε is a zero mean error term with standard deviation σ , in which $\sigma = (\sigma_r^2 + \sigma_\varepsilon^2)^{0.5}$, and σ_r and σ_ε denote the

standard deviation due to intra- and inter-event variability, respectively. If the geometric mean for Y is considered, $\sigma = (\sigma_r^2 + \sigma_\varepsilon^2 + \sigma_c^2)^{0.5}$ and the standard deviation σ_c accounts for the random orientation variability.

Table 2. Coefficients for the geometric mean and the horizontal components H1 and H2 for the records of inslab earthquakes (c_4 equals 1).

T_n (s)	c_1	c_2	c_3	c_5	σ
Geometric mean					
0.20	-0.020	0.595	-0.0036	0.0068	0.31
0.50	-0.907	0.687	-0.0024	0.0034	0.29
1.00	-1.931	0.781	-0.0016	0.0029	0.31
1.50	-2.468	0.831	-0.0014	0.0017	0.31
PGA	-0.109	0.569	-0.0039	0.0070	0.31
Horizontal component 1 (H1)					
0.20	-0.015	0.595	-0.0036	0.0065	0.31
0.50	-0.895	0.688	-0.0023	0.0028	0.29
1.00	-1.987	0.793	-0.0017	0.0029	0.29
1.50	-2.531	0.84	-0.0014	0.0019	0.28
PGA	-0.091	0.569	-0.0038	0.0065	0.31
Horizontal component 2 (H2)					
0.20	-0.034	0.596	-0.0037	0.0071	0.29
0.50	-0.913	0.683	-0.0024	0.004	0.27
1.00	-1.886	0.768	-0.0015	0.003	0.30
1.50	-2.441	0.825	-0.0014	0.0018	0.30
PGA	-0.13	0.568	-0.0039	0.0076	0.29

For the records of interplate earthquakes, the functional form of the GMPE is the one employed by García (2006), which is expressed as,

$$\log_{10} Y = c_1 + c_2 M_w + c_3 R - c_4 \log_{10} (R + c_5 10^{c_6 M_w}) + c_7 H + \varepsilon, \quad (4)$$

where $c_i, i = 1, \dots, 7$, are the model parameters, R (km) is the closest distance to the fault surface for events with $M_w > 6.0$, or the hypocentral distance for the rest, and Y, M_w, H and ε were defined previously. Note that in the above equation c_4 is considered to be given by the following equation (García 2006),

$$c_4 = 1.82 - 0.16 M_w. \quad (5)$$

Using the adopted GMPEs, the records for the events detailed in Table 1, and the regression analysis algorithm given by Joyner and Boore (1993), Hong *et al.* (2009) obtained the model coefficients for a range of natural vibration periods based on the geometric mean. For an easy reference, the model coefficients for a few selected values of the natural vibration period, T_n , are presented in Tables 2 and 3. Moreover, for comparison purposes, the regression analysis in this study is carried out by considering either the first horizontal component (H1), or the second horizontal component (H2). The obtained model

Table 3. Coefficients for the geometric mean and the horizontal components H1 and H2 for the records of interplate earthquakes (c_4 is defined in Equation 5).

T_n (s)	c_1	c_2	c_3	c_5	c_6	c_7	σ
Geometric mean							
0.20	2.609	0.144	-0.0034	0.009	0.475	-0.00410	0.39
0.50	1.542	0.238	-0.0015	0.003	0.515	-0.00300	0.40
1.00	0.734	0.301	-0.0005	0.002	0.509	-0.00500	0.41
1.50	0.214	0.336	-0.0002	0.002	0.495	-0.00490	0.40
PGA	2.545	0.108	-0.0037	0.0075	0.474	-0.00240	0.37
Horizontal component 1 (H1)							
0.20	2.658	0.129	-0.0036	0.009	0.475	-0.00105	0.40
0.50	1.653	0.211	-0.0017	0.003	0.515	-0.00001	0.40
1.00	0.862	0.265	-0.0004	0.002	0.509	-0.00283	0.40
1.50	0.343	0.298	-0.0002	0.002	0.495	-0.00195	0.40
PGA	2.608	0.088	-0.0038	0.0075	0.474	0.00073	0.40
Horizontal component 2 (H2)							
0.20	2.639	0.146	-0.0036	0.009	0.475	-0.00405	0.36
0.50	1.571	0.247	-0.0018	0.003	0.515	-0.00364	0.38
1.00	0.716	0.321	-0.0010	0.002	0.509	-0.00458	0.32
1.50	0.182	0.357	-0.0007	0.002	0.495	-0.00427	0.33
PGA	2.500	0.123	-0.0038	0.0075	0.474	-0.00330	0.34

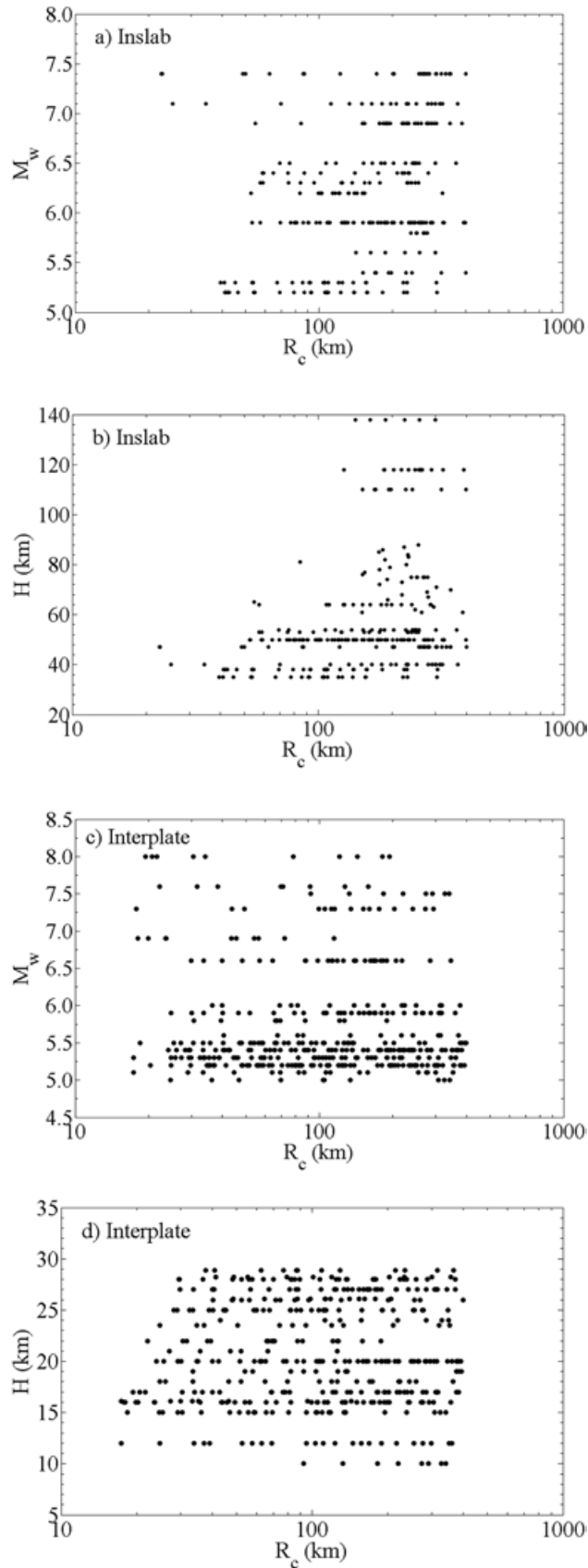


Figure 3. Distribution of M_w and H with respect to R_c : (a) and (b) for inslab events; (c) and (d) for interplate events.

coefficients are also shown in Tables 2 and 3. As the H1 and H2 components represent the seismic excitation for a random orientation (with respect to the source), the developed model coefficients shown in Tables 2 and 3 will be used to predict PGA or SA for a random orientation.

Comparison of the results shown in the tables indicates that the estimated model coefficients based on either only H1 or H2 components differ only slightly from those based on both components (i.e., geometric mean), as expected. Also, the average of the model coefficients obtained from H1 alone and from H2 alone is almost identical to those obtained based on the geometric mean. This fact simply confirms the robustness of the algorithm given by Joyner and Boore (1993) for developing the GMPEs. It also indicates that the number of records used for the purpose of regression analysis is adequate.

Prediction of strong ground motion measures using ANN

Effect of the number of hidden layers and neurons on the training ANN and on predicted values

The selection of the number of hidden layers and neurons is of importance in developing or training an ANN. This selection depends on the nature of the problem to be investigated, and a trial and error process is often followed to determine the adopted structure of the ANN model (Shahin *et al.*, 2004). In selecting the ANN model, potential overfitting due to the use of an excessive number of hidden layers and/or neurons needs to be avoided, as this will lead to a lack of learning and the inability to predict the outcomes for scenarios not used in training. To avoid the possible overfitting, several preliminary ANN models were tested by considering combinations of the single and two hidden layers and up to 50 hidden neurons in each hidden layer. Furthermore, a total of 80% randomly selected records were used to train the model, while the remaining 20% of records were used for validating the trained model.

To investigate the effect of the record selection on the trained ANN model, a total of 300 trials were carried out. For each trial, a new set of PGA and SA values from 80% randomly selected records were used. For the analysis, only one component (H1 or H2) from each record is considered; both 1HL and 2HL models are employed for the training. As the results obtained for the H1 and H2 components from the records exhibit similar trend and the results for inslab and for interplate records are similar as well, we only illustrate the estimated MSE in Figure 4 for the H1 component from the inslab records.

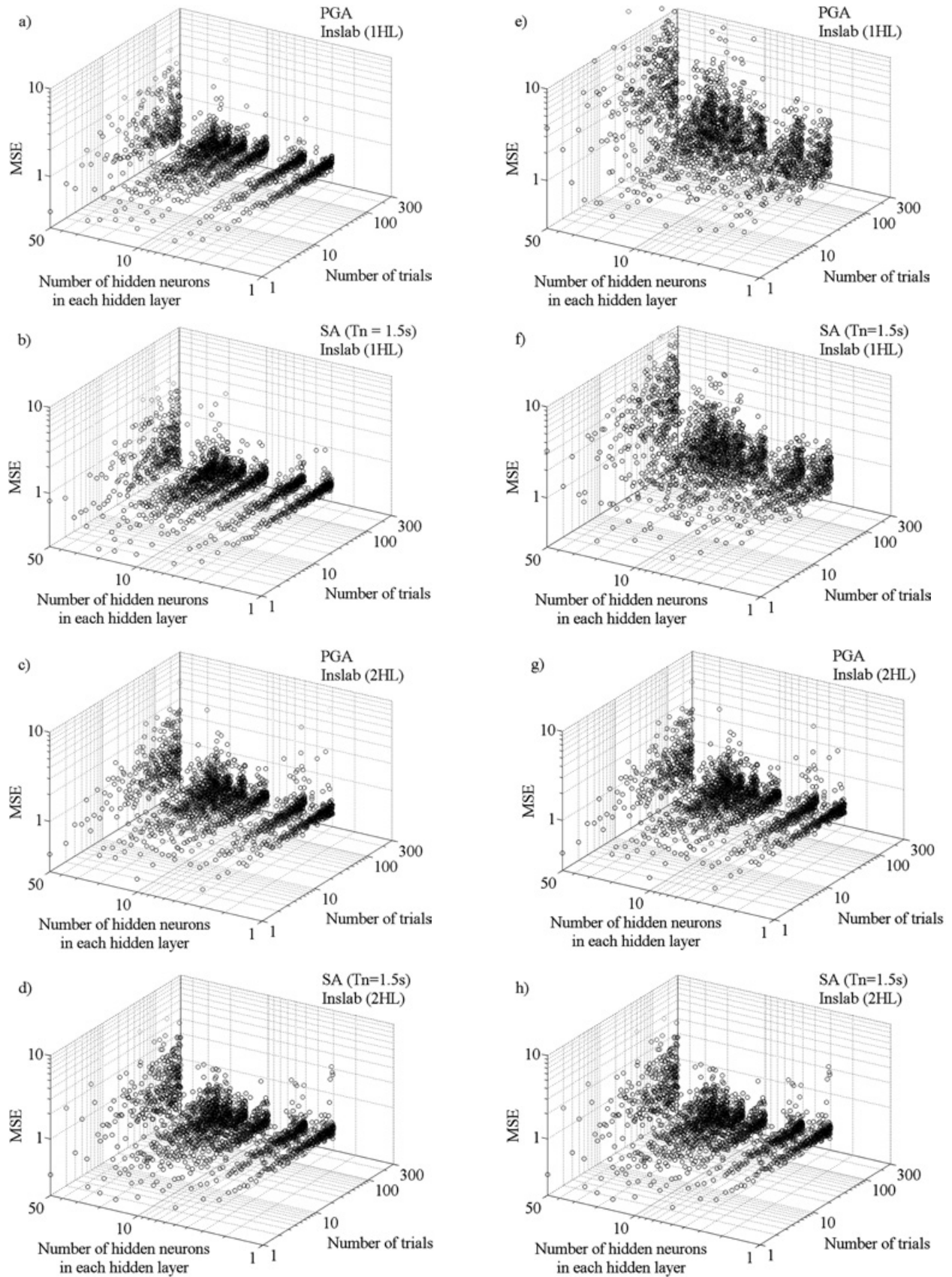


Figure 4. Variation of MSE with the number of trials and the number of neurons per hidden layer for PGA and SA ($T_n = 1.5s$) for inslab earthquakes: a) to d) training process; e) to h) validation process.

Figure 4, which presents the results for PGA and SA at $T_n = 1.5$ s, shows scatter in the MSE. As expected, the scatter (but not necessarily the standard deviation) of the MSE increases as the number of trials increases. The average MSE estimated based on 300 trials, which is considered to be sufficient large, is illustrated in Figure 5 for the training stage. The results presented in this figure indicate that the lowest average MSE is obtained for n_n around 10, and that the average MSE is relatively consistent for the number of hidden neurons, n_n , up to 25. As the average MSE for $n_n = 50$ is much larger than that for $n_n < 50$, the use of $n_n > 25$ is not recommended.

By using the remaining 20% records to test the trained ANN models, the average of MSE for 300 trials was also calculated and presented in Figure 6. Comparison of Figures 5 and 6 indicates that average values of MSE for the trained ANN models shown in Figure 6 are slightly greater than those presented in Figure 5. This can be explained by noting that the trained ANN models are tested with input parameters that are different than those used during the training process. Figure 6 also shows that the use of the model with $n_n = 50$ leads to the greatest average MSE among the considered n_n values.

During the analysis, it was observed that the optimum number of neurons and hidden layers – those leading to the lowest MSE for the trained model – depend on the selected records. In all cases, the optimum number of neurons is within 3 to 20; in about 50% of time the 1HL model outperforms the 2HL model, and vice versa. To further

inspect the differences of using the 1HL and 2HL ANN models, the mean of the ratio of the MSE of the trained 1HL model to that of the trained 2HL model shown in Figure 4 was calculated. The values are presented in Table 4. The table indicates again that there is no clear preference among the 1HL and 2HL models, although the 1HL model for inslab earthquakes may be considered to perform better than the 2HL model. Based on these observations, the use of 10 neurons and the ANN model with 1HL and with 2HL will be considered in the next section.

Comparison of predictions using trained ANN

The training of the ANN models with 1HL and with 2HL was carried out by considering 10 neurons in each layer. For the analysis, the use of all H1 components and all H2 components are considered. As the results based on H1 or H2 components are almost the same, only the results for H1 are presented. Also, analysis was carried out by using only the geometric mean since this quantity is commonly used to develop GMPEs. For this case, the obtained weights and biases for the trained models are presented in the Appendix.

A comparison of the predicted PGA and SA by using the trained models to those obtained from the actual records is shown in Figures 7 and 8 for the H1 components and the geometric mean, respectively. It can be observed from the figures that there is a good agreement between the predicted and observed values, and that the correlation coefficient, ρ , is greater than 0.77 in all cases. The trained ANN models for inslab

Table 4. Comparison of the mean of the ratio of the MSE of ANN models with 1HL to that with 2HL by considering the H1 components.

Earthquake Type	Number of neurons	PGA	SA ($T_n=0.2s$)	SA ($T_n=0.5s$)	SA ($T_n=1.0s$)	SA ($T_n=1.5s$)
Inslab	3	0.88	0.86	0.88	0.88	0.91
	5	1.12	1.19	1.19	1.19	1.15
	10	1.00	1.00	1.06	1.10	1.09
	15	0.98	1.06	1.11	1.05	1.08
	20	0.86	0.93	0.95	0.91	0.93
	25	0.86	0.83	0.77	0.84	0.87
	50	0.54	0.50	0.48	0.50	0.45
Interplate	3	0.91	0.93	0.98	0.95	0.93
	5	1.15	1.11	1.07	1.11	1.11
	10	1.02	1.03	1.09	1.08	1.05
	15	1.05	1.08	0.98	1.03	1.11
	20	0.98	1.00	1.04	1.02	1.10
	25	1.01	0.99	0.97	0.88	0.94
	50	0.47	0.48	0.54	0.47	0.49

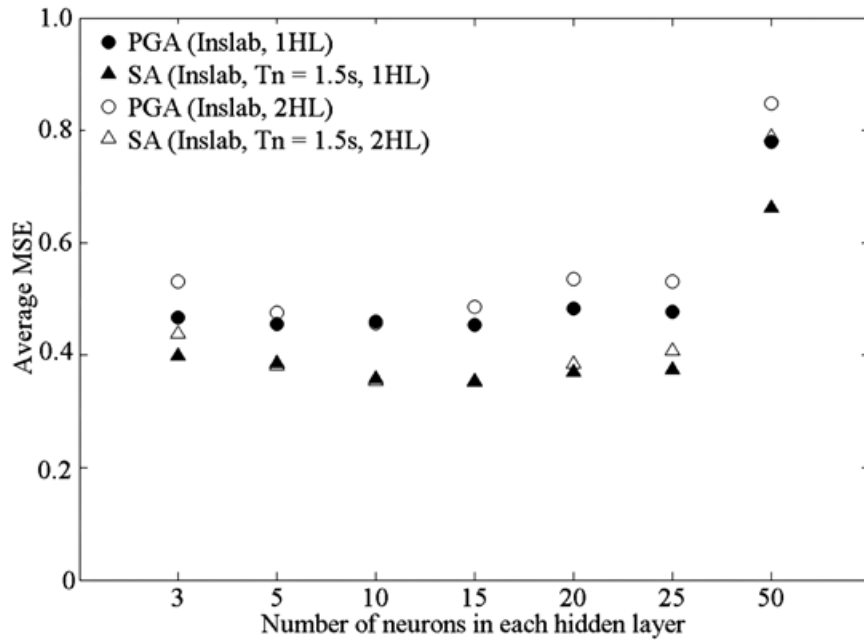


Figure 5. Average mean square error for the trained ANN models by using the samples employed for training.

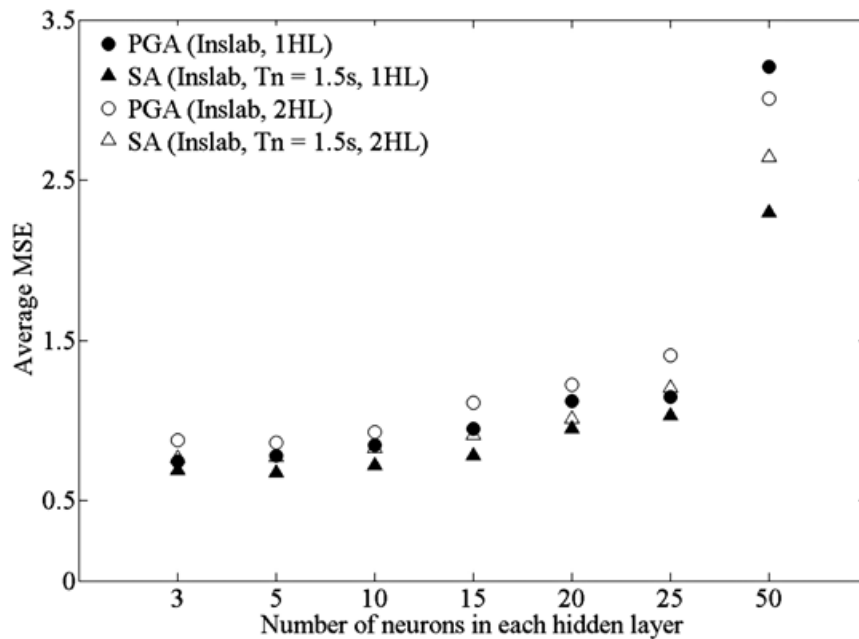


Figure 6. Average mean square error for the trained ANN models by using the samples that are not employed for training.

earthquakes provide better estimates than those for interplate earthquakes if H1 is considered; if the geometric mean is considered, both ANN models provide similar estimates. The scatter shown in the figures appears to be independent of the logarithm of PGA or logarithm of SA. A more detailed statistical investigation considering that the residual - η defined as the difference between the logarithmic of the actual PGA (or SA) and the logarithmic of the predicted PGA (or SA) - as a function of the predicted PGA (or SA) is beyond the scope of this study.

To provide a probabilistic characterization of the residual, η is shown in Figure 9 for a few selected cases presented in Figures 7 and 8. Inspection of the plots and use of a Kolmogorov-Smirnov test (Benjamin and Cornell, 1970) indicate that η can be modeled as a normal variable. The mean and the standard deviation of η for the cases presented in Figure 9 are summarized in Table 5, where the statistics of η , shown for the geometric mean case, were calculated by taking into account that the trained model will be used to predict ground motion measures for a random orientation, rather than the geometric mean (see Section 3).

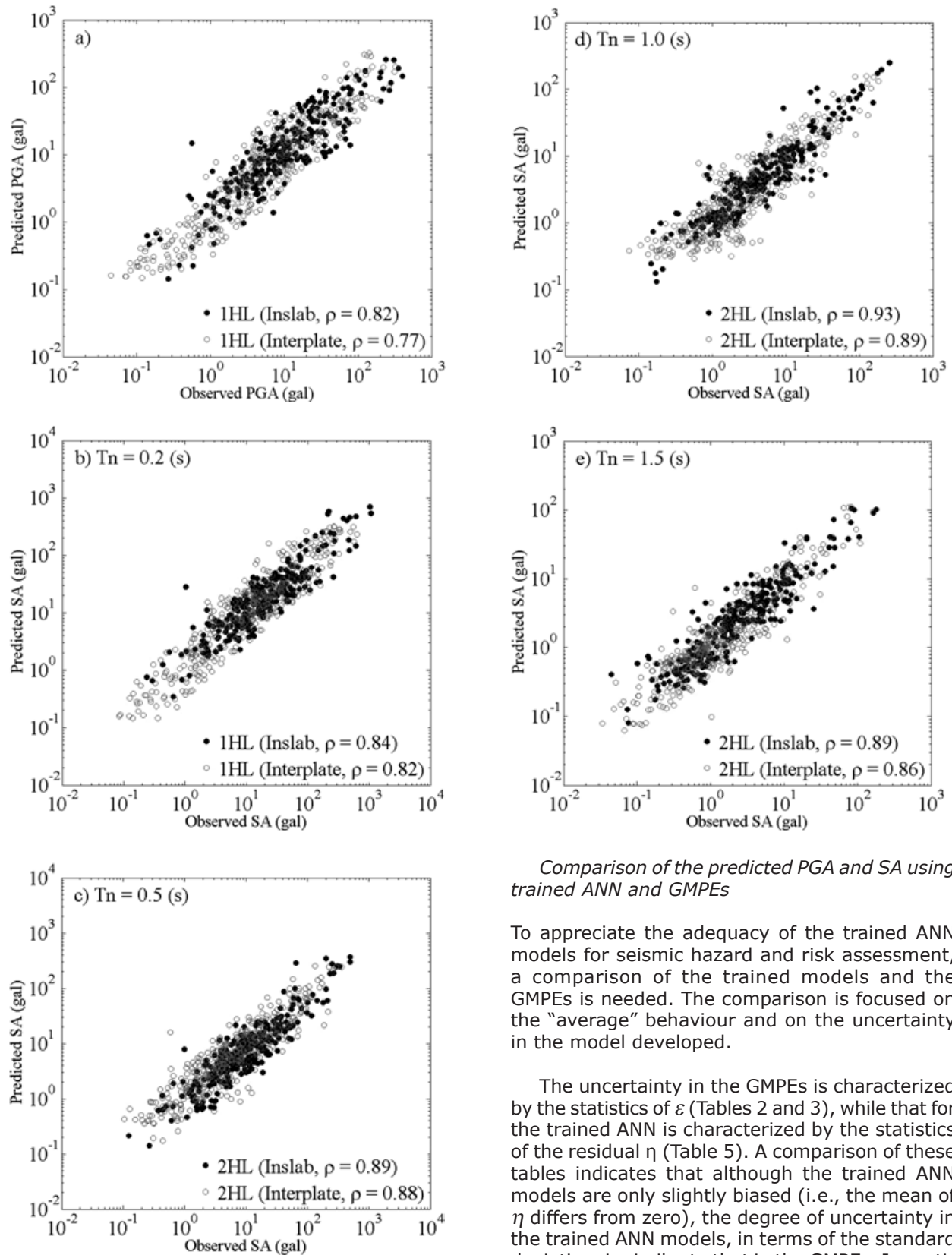


Figure 7. Comparison of predicted and observed PGA and SA H1 component values for in slab and interplate earthquakes (ρ in the plots denotes correlation coefficient).

Comparison of the predicted PGA and SA using trained ANN and GMPEs

To appreciate the adequacy of the trained ANN models for seismic hazard and risk assessment, a comparison of the trained models and the GMPEs is needed. The comparison is focused on the “average” behaviour and on the uncertainty in the model developed.

The uncertainty in the GMPEs is characterized by the statistics of ε (Tables 2 and 3), while that for the trained ANN is characterized by the statistics of the residual η (Table 5). A comparison of these tables indicates that although the trained ANN models are only slightly biased (i.e., the mean of η differs from zero), the degree of uncertainty in the trained ANN models, in terms of the standard deviation, is similar to that in the GMPEs. In particular, the statistics of η and ε are very consistent for the case when the geometric mean was used to develop the GMPEs and to train the ANN models. Since η and ε shown in Eqs. (3) and (4) represent

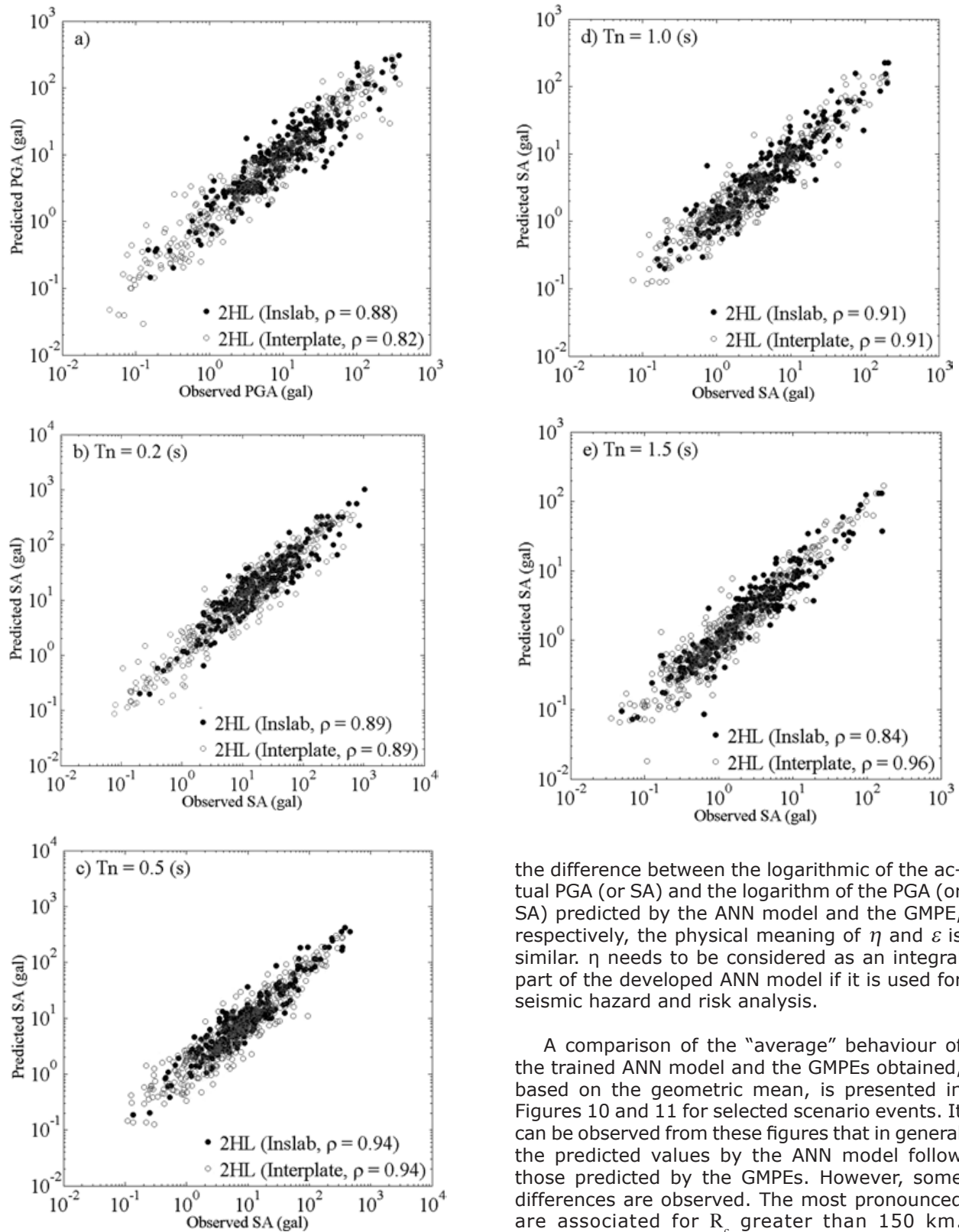


Figure 8. Comparison of predicted and observed geometric mean of PGA and SA for inslab and interplate earthquakes (ρ in the plots denotes correlation coefficient).

the difference between the logarithmic of the actual PGA (or SA) and the logarithm of the PGA (or SA) predicted by the ANN model and the GMPE, respectively, the physical meaning of η and ε is similar. η needs to be considered as an integral part of the developed ANN model if it is used for seismic hazard and risk analysis.

A comparison of the “average” behaviour of the trained ANN model and the GMPEs obtained, based on the geometric mean, is presented in Figures 10 and 11 for selected scenario events. It can be observed from these figures that in general the predicted values by the ANN model follow those predicted by the GMPEs. However, some differences are observed. The most pronounced are associated for R_c greater than 150 km. Moreover, in some cases, the predicted values by the trained ANN models may not necessarily reflect reality. For example, the results shown in Figure 10c indicate that SA can increase with distance beyond $R_c = 200$ km for $M_w = 5.9$ and $H = 50$ km, which is unrealistic. Since this drawback

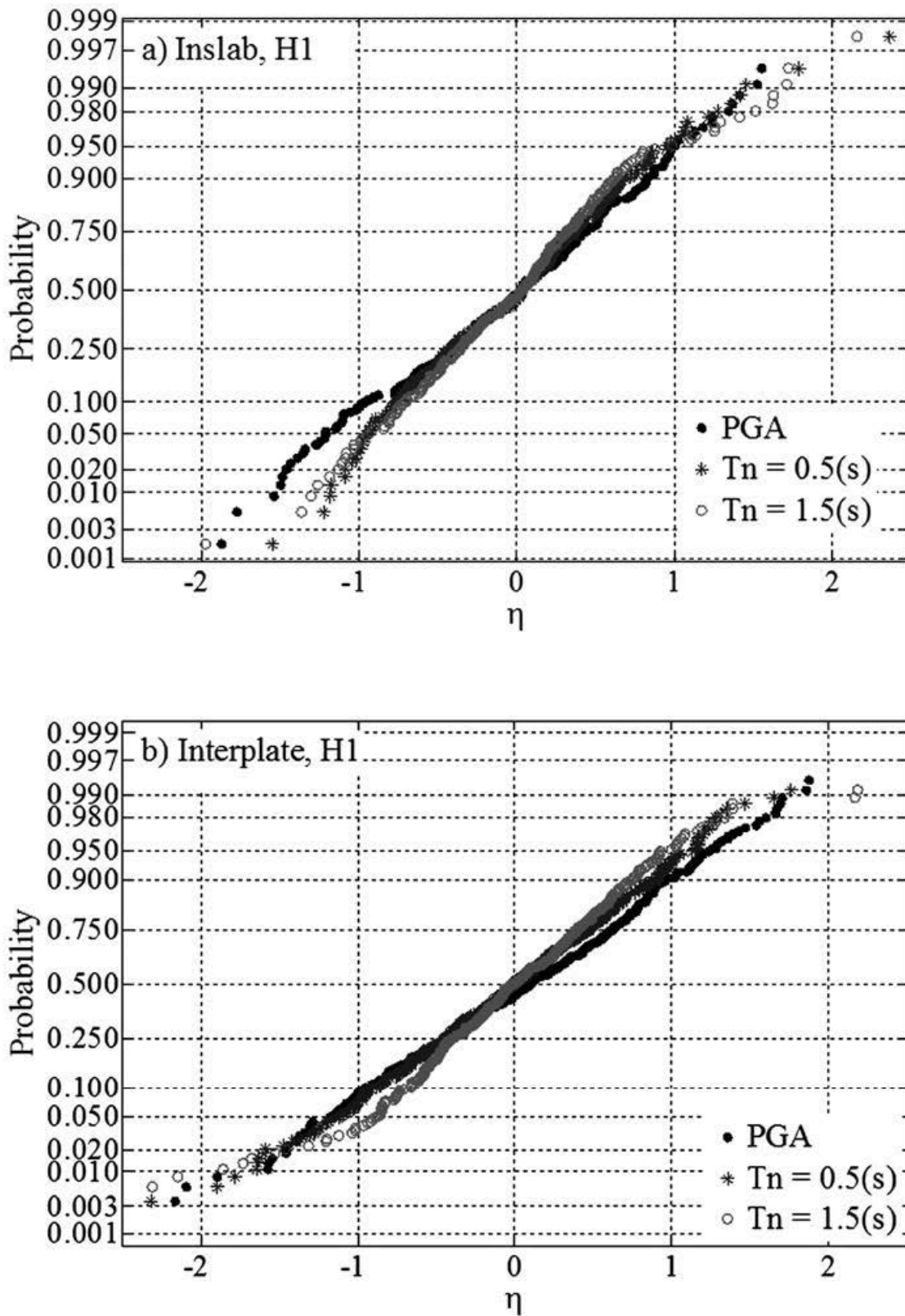


Figure 9. Normal probability plots of the residual η .

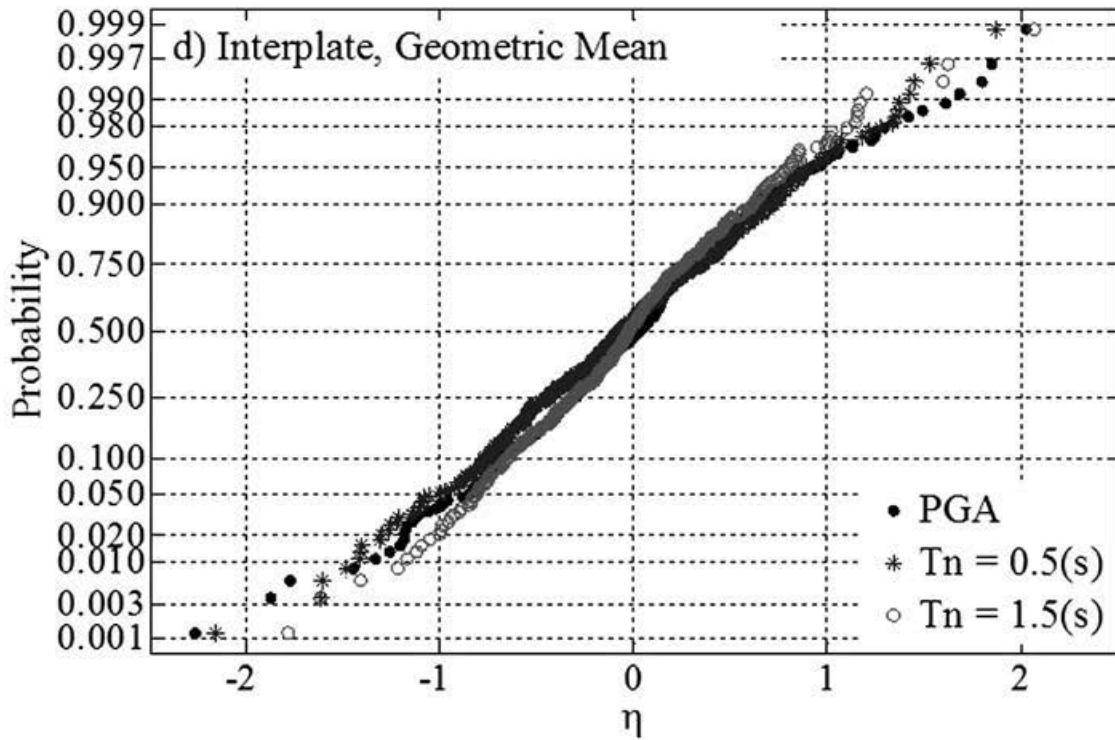
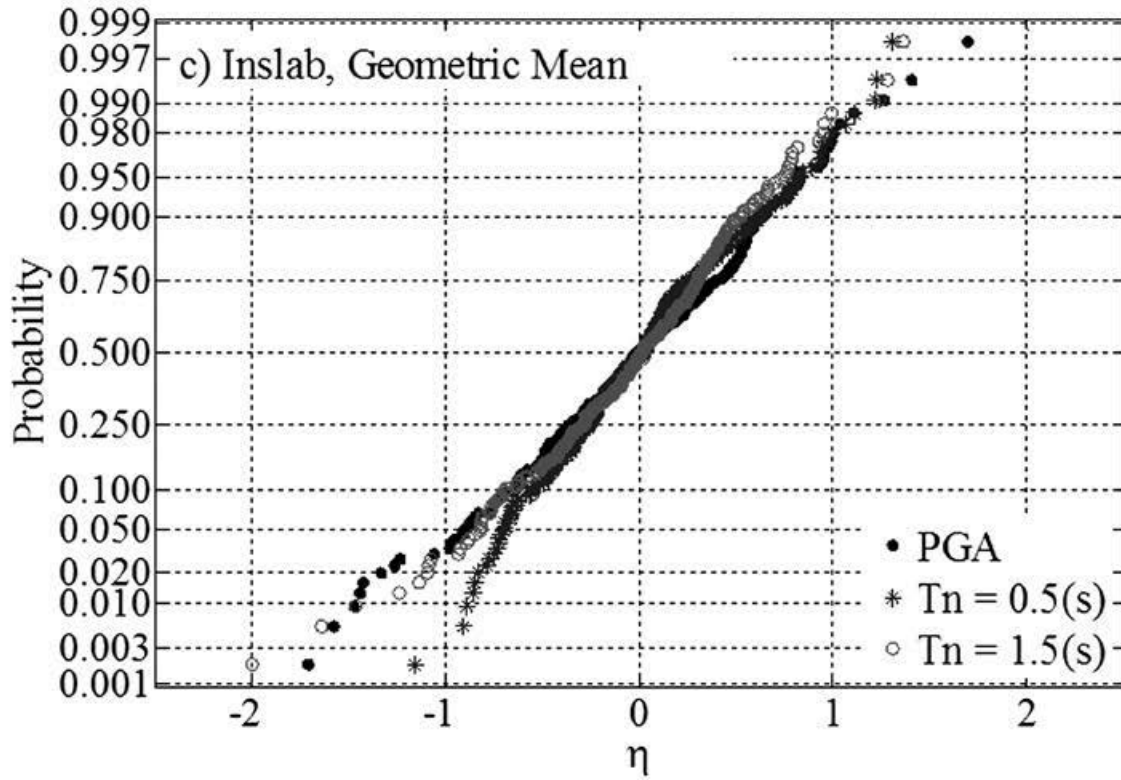
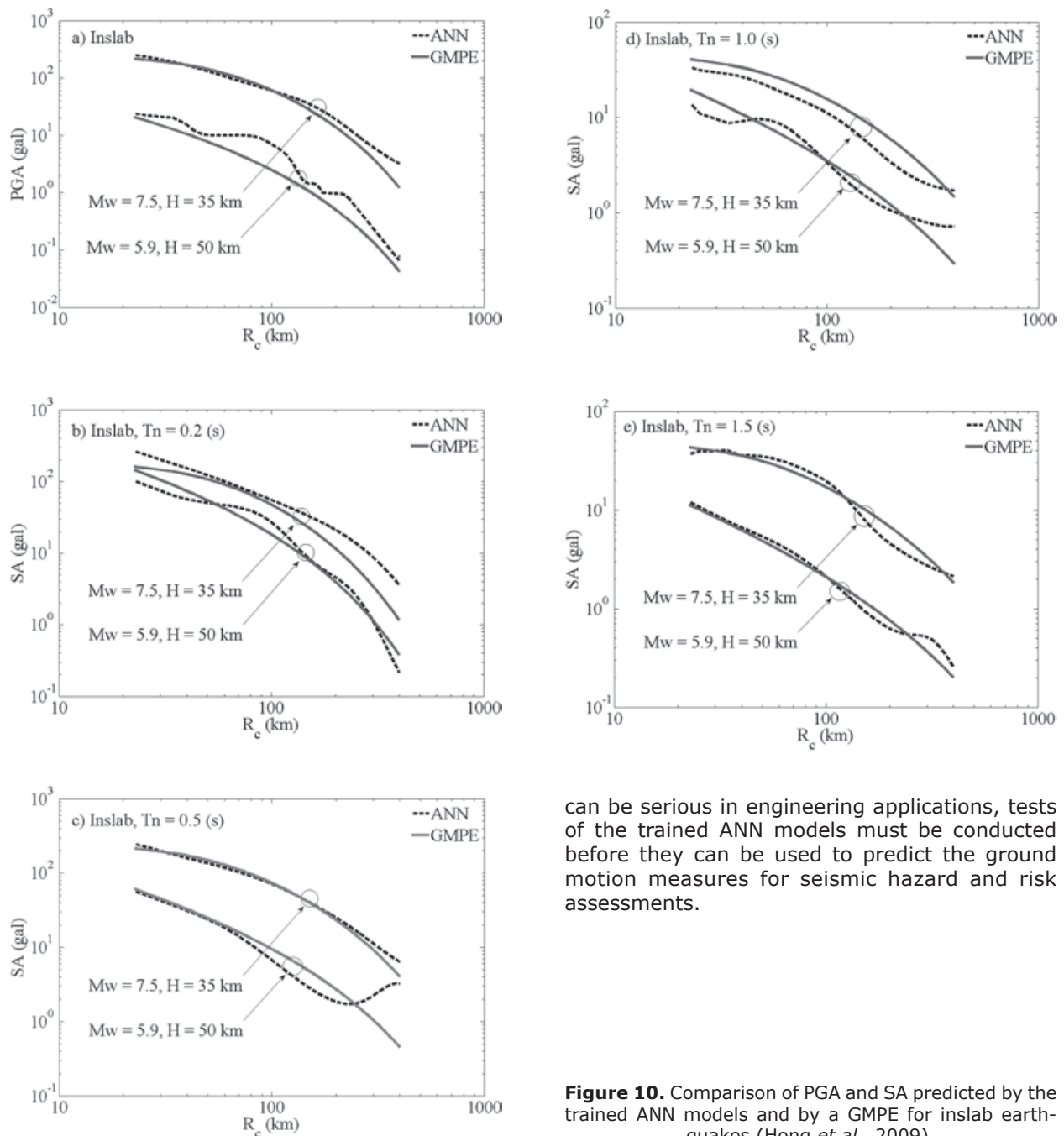


Figure 9. Continued.

Table 5. Statistics of η for cases shown in Figure 10.

Earthquake Type		H1		Geometric Mean	
Inslab	PGA	mean	Std. Dev.	mean	Std. Dev.
	SA (Tn=0.5s)	1.5E-01	0.68	9.2E-03	0.35
	SA (Tn=1.5s)	-3.0E-01	0.58	-7.3E-03	0.32
Interplate	PGA	mean	Std. Dev.	mean	Std. Dev.
	SA (Tn=0.5s)	4.9E-02	0.57	5.0E-04	0.33
	SA (Tn=1.5s)	-1.4E-01	0.67	7.3E-03	0.38
	SA (Tn=0.5s)	-5.5E-03	0.79	-1.2E-02	0.43
	SA (Tn=1.5s)	-6.6E-02	0.72	7.0E-03	0.40



can be serious in engineering applications, tests of the trained ANN models must be conducted before they can be used to predict the ground motion measures for seismic hazard and risk assessments.

Figure 10. Comparison of PGA and SA predicted by the trained ANN models and by a GMPE for inslab earthquakes (Hong *et al.*, 2009).

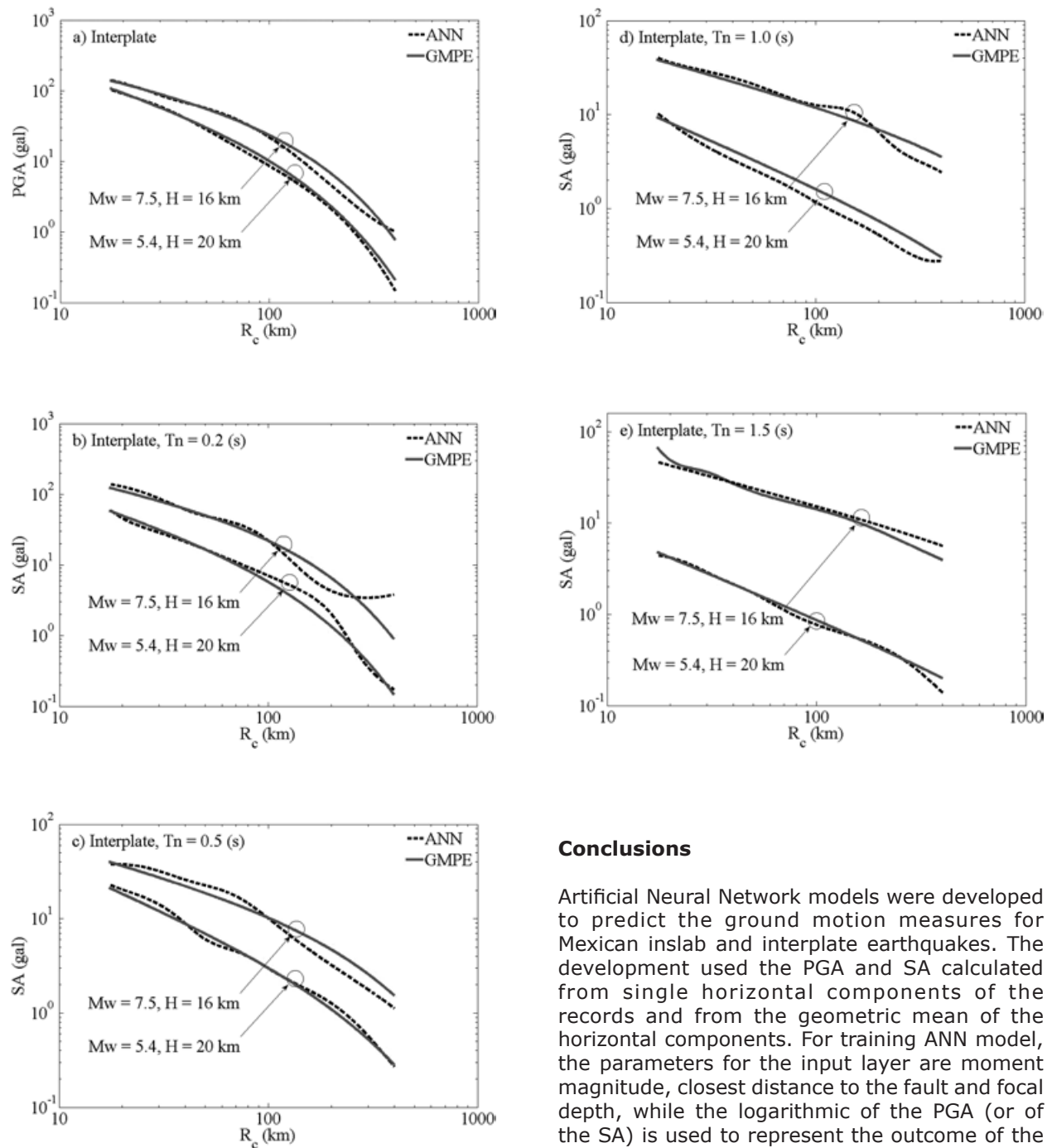


Figure 11. Comparison of PGA and SA predicted by the trained ANN models and by a GMPE for interplate earthquakes (Hong *et al.*, 2009).

Conclusions

Artificial Neural Network models were developed to predict the ground motion measures for Mexican inslab and interplate earthquakes. The development used the PGA and SA calculated from single horizontal components of the records and from the geometric mean of the horizontal components. For training ANN model, the parameters for the input layer are moment magnitude, closest distance to the fault and focal depth, while the logarithmic of the PGA (or of the SA) is used to represent the outcome of the model. The main observations that can be drawn from the analysis results are:

1. The performance of the trained ANN model by using a single hidden layer is similar to that by using two hidden layers. The most appropriate number of neurons per hidden layer seems to be within 3 to 20.
2. The use of a single horizontal component or the geometric mean of the two horizontal components leads to similar trained ANN models, implying that the number of considered records is adequate.

3. The statistics of the residuals associated with the trained ANN models are similar to those associated with the GMPEs. The ground motion measures predicted by the trained ANN models follow those predicted by the GMPEs. This indicates that the ANN models may be a good alternative to GMPEs in some applications.
4. In some cases, the SA predicted by the trained ANN models increases as the R_c increases. This does not reflect the general behaviour observed from actual records. Therefore, extensive verification of the trained ANN models should be carried out before the models can be used for seismic engineering applications.

Acknowledgments

Financial support of the National Council of Science and Technology (CONACyT) of Mexico, the Natural Science and Engineering Research Council of Canada, the University of Western Ontario, and the IIUNAM are gratefully acknowledged. We thank T.J. Liu and S.C. Lee for many fruitful discussions, constructive comments and suggestions. We also thank two anonymous reviewers for their comments and suggestions that helped to improve this work.

Bibliography

- Atkinson G.M., Boore D.M., 2003, Empirical ground-motion relations for subduction-zone earthquakes and their application to Cascadia and other regions. *Bull. Seism. Soc. Am.*, 93, 1703-1729.
- BSSC, 2004, NEHRP Recommended provisions for seismic regulations for new buildings and other structures (FEMA 450), 2003 Edition.
- Benjamin J.R., Cornell C.A., 1970, Probability, Statistics and Decision for Civil Engineers. McGraw-Hill, New York.
- Fausset L.V., 1994, Fundamentals of neural networks: Architecture, algorithms, and applications. Prentice-Hall, Englewood Cliffs, N.J., 461 pp.
- García D., Singh S.K., Herraiz M., Ordaz M., Pacheco J.F., 2005, Inslab earthquakes of Central Mexico: Peak ground-motion parameters and response spectra, *Bull. Seism. Soc. Am.*, 95, 2272-2282.
- García D., 2006, Estimación de parámetros del movimiento fuerte del suelo para terremotos interplaca e intraslab en México Central, PhD Tesis, Universidad Complutense de Madrid, Madrid, España. (In Spanish).
- García D., Singh S.K., Herraiz M., Ordaz M., Pacheco J.F., 2009, Erratum to Inslab Earthquakes of Central Mexico: Peak ground-motion parameters and response spectra, *Bull. Seism. Soc. Am.*, 99, 2607-2609.
- García S.R., Romo M.P., Mayoral J.M., 2007, Estimation of peak ground accelerations for Mexican subduction zone earthquakes using neural networks. *Geofísica Internacional*, 46, 1, 51-63.
- Ghaboussi J., Li C.C.J., 1998, New method of generating spectrum compatible accelerograms using neural networks. *Earthquake Engineering and Structural Dynamics*, 27, 4, 377-396.
- Günaydn K., Günaydn A., 2008, Peak ground acceleration prediction by artificial neural networks for northwestern Turkey. *Mathematical Problems in Engineering*, Art. No.: 919420.
- Hagan M.T., Menhaj M., 1994, Training feed-forward networks with the Marquardt algorithm. *IEEE Transactions on Neural Networks* 5, 6, 989-993.
- Hong H.P., Pozos-Estrada A., Gómez R., 2009, Orientation effect on ground motion measure for Mexican subduction earthquakes, *Earthquake Engineering and Engineering Vibration*, 8, 1, 1-16.
- Hong H.P., Liu T.J., Lee C.S., 2012, Observation on the application of artificial neural network for predicting ground motion measures. *Earthq. Sci.*, 25, 161-175.
- Joyner W.B., Boore D.M., 1993, Methods for regression analysis of strong-motion data. *Bull. Seism. Soc. Am.*, 83, 469-487.
- Kamatchi P., Rajasankar J., Ramana G.V., Nagpal A.K., 2010, A neural network based methodology to predict site-specific spectral acceleration values. *Earthq. Eng. & Eng. Vib.*, 9, 4, 459-472.
- Lee S.C., Han S.W., 2002, Neural-network-based models for generating artificial earthquakes and response spectra. *Computers and Structures*, 80, 1627-1638.
- Marquardt D.W., 1963, An algorithm for least squares estimation of non-linear parameters. *Journal of the Society for Industrial and Applied Mathematics*, 11, 2, 431-41.

Press W.H., Teukolsky S.A., Vetterling A.W.T., Flannery B.P., 1992, Numerical Recipes in C: The Art of Scientific Computing. Cambridge University Press, New York.

Shahin M., Maier H.R., Jaksa M.B., 2004, Data division for developing neural networks applied to geotechnical engineering. *Journal of Computing in Civil Engineering*, 18, 2, 105-114.

Appendix

Weights and biases for the trained models.

The coefficients of the trained models needed for their application are given in the following tables (next page).

Table A1. Trained ANN based models based on the geometric mean for inslab earthquakes.

Ground motion measure	Biases			$(\varphi_1)_j$	$(\varphi_2)_k$	$(\varphi_3)_l$
	Weights $[w_{1,ij}]$	$[w_{2,j,k}]$	$[w_{3,k,l}]$			
PGA	2.821 -0.442 -0.326	0.112 -0.867 0.572 0.620 0.283 0.919 0.792 -0.849 0.711 0.278	-0.189 ^T	3.127	1.616	
	1.550 0.298 -1.117	0.297 0.445 0.669 0.410 0.114 0.233 0.574 0.552 -0.086 0.853	-1.126	-3.449	-1.249	
	-0.403 1.062 -2.946	0.196 -0.449 -0.720 -0.513 -0.545 1.273 -1.493 -0.155 -0.530 0.199	-0.542	1.883	-0.664	
	1.393 1.396 -3.542	-0.534 0.622 -0.601 -0.773 -0.120 0.095 0.041 0.115 1.209 -0.811	-0.342	-0.255	0.404	
	-0.321 -4.174 -1.435	0.414 -0.334 1.165 -0.643 0.135 0.005 0.363 0.784 -0.164 0.710	0.118	-0.072	-0.023	
	2.260 1.522 0.371	-0.155 0.047 -0.122 0.726 1.037 0.133 -0.775 -0.347 -0.517 -0.766	0.197	-0.792	-0.239	
	-1.717 1.224 -2.953	-0.645 0.207 1.085 -1.037 0.083 -0.628 -0.080 0.536 1.290 -0.310	-1.009	-1.157	-0.421	
	1.661 -2.410 -1.047	0.271 -1.032 -0.398 -1.218 -0.722 1.412 0.024 -0.584 -0.561 0.220	-0.193	2.001	0.955	
	-1.502 1.250 2.445	-0.612 -0.534 0.038 -0.634 -1.105 0.132 1.154 0.034 -0.083 -1.051	0.145	-2.461	-1.871	
	1.450 0.044 -2.334	-0.778 -0.121 0.105 0.710 0.433 1.376 0.152 0.050 0.278 0.082	-0.510	3.317	-1.856	
SA ($T_n = 0.2s$)	1.224 -1.508 0.791	1.272 0.610 -0.819 1.773 -2.535 -0.731 -0.917 -0.996 2.389 0.103	-0.061	2.794	-2.175	
	1.951 -1.116 -2.350	0.236 1.020 -0.231 -0.724 -1.369 3.030 1.324 -0.322 -0.830 0.785	0.085	-1.198	-1.302	
	4.020 -2.741 1.574	0.463 0.362 -0.056 -1.236 -1.865 0.106 -0.484 -1.132 -1.934 0.755	-0.591	-1.397	0.714	
	-2.343 -1.005 0.470	-1.295 0.058 0.053 0.474 1.656 -0.033 -0.398 0.119 -0.025 -0.180	-0.510	-0.365	0.112	
	3.942 2.336 -1.447	-0.251 -2.146 0.704 0.288 2.652 0.022 -1.594 1.170 2.310 0.425	-0.001	0.147	0.332	
	-3.192 2.519 1.096	-1.065 0.577 -0.202 1.599 -0.456 -0.566 -1.019 -1.898 -0.221 1.603	0.859	-0.254	0.641	
	0.433 -1.072 1.655	-0.616 0.653 0.453 -0.645 -0.373 -0.649 -0.457 -0.812 -0.220 -0.317	0.493	-1.531	0.871	
	-2.459 -0.142 -2.169	-0.043 -0.732 -1.272 0.659 1.252 0.283 -1.198 -1.200 1.408 0.676	-0.156	-3.569	-0.871	
	2.804 1.662 0.401	-0.472 -0.556 -2.625 0.135 0.843 -0.558 -2.408 -0.108 -1.570 0.210	-0.158	2.171	-0.777	
	1.559 2.303 -1.665	-0.244 0.549 0.812 -0.326 -0.053 -0.414 0.005 -0.640 1.300 0.303	0.295	2.996	-1.797	
SA ($T_n = 0.5s$)	3.467 -3.972 0.384	-0.206 -1.082 2.408 -0.953 0.304 1.036 0.258 -1.810 3.089 1.195	0.222	-1.079	2.428	
	-1.492 0.465 3.979	0.953 -0.245 -1.262 0.652 -2.087 1.062 0.563 1.313 0.942 1.750	-0.117	-2.069	-1.890	
	1.757 -5.789 0.310	2.095 -0.391 -0.762 0.744 -1.352 -0.357 1.739 -1.721 1.621 0.456	0.432	-1.501	0.877	
	-1.875 -1.008 0.604	0.261 0.106 -0.337 -0.307 -1.157 0.071 0.258 0.439 2.123 1.449	-0.039	1.690	0.898	
	2.382 -0.296 0.087	-1.796 0.253 -1.052 -0.588 -1.763 1.693 0.867 -0.581 -2.418 0.063	-0.176	2.796	-0.313	
	5.506 1.845 -1.531	1.328 -1.285 1.094 0.564 -2.257 -1.572 -0.470 -1.763 -0.554 -1.288	-0.189	3.670	-0.795	
	-1.144 0.552 -1.498	1.455 0.011 0.253 -1.988 1.423 -0.080 1.055 -0.173 -0.767 -0.251	0.196	-0.639	0.368	
	-2.236 1.740 -0.007	1.531 -0.363 0.742 0.393 2.778 -1.354 0.636 1.310 0.074 -1.887	-0.127	-1.938	1.688	
	0.768 -1.121 2.577	-0.932 -1.853 0.528 1.457 1.450 -4.191 -0.193 2.582 1.314 3.679	-0.079	0.477	2.703	
	1.864 -2.560 -1.610	-1.452 -0.830 -1.892 1.849 -2.418 -0.971 -1.559 -1.284 -1.208 0.168	0.176	-3.354	-2.165	
SA ($T_n = 1.0s$)	-0.072 1.100 -3.185	0.192 -0.368 0.793 0.222 -0.391 -0.113 -0.846 -0.298 0.922 -0.225	0.186	-3.056	-1.958	
	1.722 -2.105 1.244	0.199 0.096 -0.648 -0.114 -0.647 0.508 0.420 -0.828 1.301 -1.145	0.832	-1.994	-1.507	
	0.463 -2.734 -1.250	0.351 -0.260 -0.344 0.900 0.701 -0.977 -0.188 -0.875 0.422 0.772	0.647	-1.652	0.767	
	-0.575 -2.223 -1.059	1.375 0.481 0.359 1.050 0.291 1.264 0.628 -0.138 0.878 -0.341	-0.838	1.738	-0.732	
	2.771 1.275 1.707	0.801 -0.592 -0.884 0.827 -0.832 -0.148 0.378 -0.659 -0.239 0.189	-0.274	-0.569	-0.336	
	-1.460 -1.329 -1.897	0.128 0.619 0.224 1.281 -0.580 -0.660 0.984 0.388 0.210 0.092	0.589	-0.424	-0.345	
	-0.922 -1.371 -2.621	1.279 -0.374 -1.256 -0.235 0.431 -0.354 0.068 0.419 -0.105 -0.052	-0.594	-0.781	0.719	
	0.863 1.517 2.682	0.358 -0.386 -0.373 -0.504 0.467 0.455 -0.099 -0.835 -0.597 -0.499	-0.501	1.675	1.273	
	0.678 -0.974 -2.366	0.583 0.375 -0.518 -0.721 -0.030 0.314 -0.983 0.977 0.229 -0.237	0.548	-2.271	1.369	
	-1.375 -2.302 -1.508	0.494 -0.378 -0.821 1.427 0.277 0.756 -0.041 0.292 -0.758 0.933	0.816	-2.991	1.698	
SA ($T_n = 1.5s$)	-0.733 -1.391 -2.628	-1.047 0.382 0.187 0.414 -0.091 0.164 0.514 -1.575 -0.534 0.022	-1.394	3.025	1.626	
	1.561 1.020 2.597	0.690 0.700 0.625 0.042 -0.614 -0.176 -0.263 0.791 -0.523 -0.629	-2.042	-2.042	-1.396	
	1.118 -2.763 1.810	-0.701 -0.393 1.271 -0.471 1.350 -0.860 1.176 0.642 0.397 -0.153	-0.938	-2.013	0.641	
	-0.859 1.785 -0.971	0.114 -0.237 -0.295 -0.044 0.376 -1.404 0.058 -0.486 2.229 0.828	-1.268	-0.945	-0.656	
	-2.939 1.481 2.526	-0.735 -0.719 0.457 0.411 -0.403 -1.238 -0.450 -1.205 0.612 0.578	0.844	0.820	0.375	
	-2.563 -2.328 1.668	-0.809 -0.708 -0.158 0.468 -0.889 -0.147 0.776 0.108 0.765 0.975	1.492	-0.304	-0.060	
	2.670 3.101 -0.386	-0.750 -0.870 0.006 -0.101 -0.803 1.064 0.304 -0.632 0.369 -0.457	-0.958	0.060	-0.427	
	-1.206 2.729 0.984	0.724 0.438 0.350 -1.811 -1.264 2.281 -0.083 -1.224 -0.832 -0.867	0.577	-2.518	0.973	
	2.467 2.431 -0.890	-0.412 1.044 1.244 0.008 0.244 1.134 1.245 -1.587 0.607 -0.219	1.300	2.370	1.403	
	1.280 1.701 -1.879	0.189 -0.255 0.759 0.182 -1.099 0.762 0.467 0.037 -0.553 0.597	-0.078	3.204	1.650	

Table A2. Trained ANN based prediction models based on the geometric mean for interplate earthquakes.

Ground motion measure	Biases			$(\varphi_1)_j$	$(\varphi_2)_k$	$(\varphi_3)_l$
	Weights $[w_{1,ij}]$	$[w_{2,j,k}]$	$[w_{3,kl}]$			
PGA	[1.791 -0.869 -2.141]	[0.094 1.226 1.961 0.514 -1.157 -0.186 0.045 0.184 -0.419 1.498]	^T [-0.425 0.236 0.104 0.106 0.428 -0.106 0.011 -0.180 -0.681]	[-1.840 -2.731 -2.027 -2.539 1.652 0.449 0.110 -0.079 -3.293 -1.539 1.352 2.543]	[1.350 -2.033 1.645 -0.498 0.449 0.110 -0.210 -1.539 1.352 2.543]	[0.827]
	[0.365 1.294 -2.107]	[0.280 1.264 0.123 0.035 -0.134 -1.150 1.045 0.256 -0.407 0.792]				
	[4.105 4.119 -1.505]	[-0.291 0.373 -0.372 0.701 0.946 -0.213 0.908 -0.137 -0.928 1.499]				
	[2.162 3.641 0.440]	[0.587 -0.377 -1.206 1.643 2.231 -1.531 0.819 -1.217 0.456 -0.463]				
	[0.404 -2.190 -1.070]	[-0.107 0.105 0.142 -1.171 1.519 -1.700 1.666 -1.779 1.991 -0.795]				
	[-0.559 0.745 -1.400]	[0.573 -0.045 -0.487 1.221 0.754 -0.583 -0.394 0.278 -0.347 0.653]				
	[-4.120 0.402 2.188]	[-1.336 -0.120 -1.190 1.629 0.409 -0.562 2.130 0.668 2.194 -0.748]				
	[6.272 -4.973 1.308]	[0.485 0.382 -1.370 -1.015 -1.673 1.279 0.495 4.568 1.189 0.946]				
	[1.631 1.394 0.943]	[0.847 0.869 -1.635 -0.626 -2.092 0.774 -0.460 -0.089 -0.003 0.531]				
	[-0.986 2.693 -0.063]	[-0.382 -0.184 -0.378 -0.032 0.318 1.078 -0.717 -0.428 1.293 0.278]				
SA ($T_n = 0.2s$)	[1.488 -1.858 -0.906]	[1.066 -0.661 -0.541 -1.642 2.877 -0.178 3.677 -0.336 -0.622 -1.551]	^T [1.456 -0.145 0.493 0.181 -0.281 1.397 0.183 1.098 -1.361 -0.330]	[-3.599 2.751 -1.521 0.007 -0.211 -1.048 0.648 -1.048 4.065 0.688]	[1.535 -1.139 -1.166 -0.048 -0.971 1.827 1.244 -2.517 0.500 -0.198]	[0.252]
	[-2.964 2.267 0.711]	[1.554 -0.903 -0.312 -0.893 2.219 0.487 -0.674 2.919 2.611 -1.528]				
	[2.516 -1.195 -1.058]	[0.533 -0.484 1.177 -0.577 0.644 -0.964 -0.720 0.523 -0.365 0.523]				
	[-3.650 0.815 -2.497]	[1.958 1.327 1.338 0.536 -0.688 -3.058 -1.000 1.259 -0.222 -0.899]				
	[0.422 1.359 -0.917]	[1.723 0.152 -0.933 -0.007 1.019 3.421 -0.071 0.794 -0.927 1.201]				
	[-2.388 -0.526 0.159]	[-1.722 1.002 -1.037 0.394 1.241 2.911 -0.376 -0.449 0.941 -1.324]				
	[0.881 -0.630 0.064]	[-0.860 0.244 -0.625 -0.565 -1.250 2.211 2.973 -0.311 -0.507 -1.061]				
	[-1.414 -0.609 2.831]	[1.599 -1.381 2.239 -0.651 -1.386 0.594 0.884 -0.320 0.028 0.534]				
	[1.535 2.322 -2.874]	[-1.318 0.250 2.095 -2.196 1.318 0.052 0.843 -0.108 -0.229 -0.992]				
	[-1.599 2.782 -0.566]	[-1.756 0.061 -0.757 -0.145 0.149 -1.133 -3.209 -0.307 0.532 -0.746]				
SA ($T_n = 0.5s$)	[-2.590 -1.334 0.359]	[1.120 0.372 -1.141 0.501 0.843 -1.303 0.636 0.418 -1.094 -0.196]	^T [0.589 0.051 0.173 0.449 0.412 0.149 -0.261 -0.004 0.025 0.514]	[-1.905 -1.259 1.421 -1.754 -0.312 -0.126 -1.038 1.866 -2.223 1.980]	[1.905 -1.259 1.421 -1.754 -0.312 -0.126 -1.038 1.866 -2.223 1.980]	[0.172]
	[1.683 -2.001 -1.997]	[0.496 0.371 0.076 -1.258 -0.725 1.290 0.601 1.407 1.132 -0.126]				
	[-1.286 1.843 2.949]	[-0.548 0.163 -1.305 0.309 -1.289 0.949 0.605 0.776 -0.677 -0.986]				
	[1.054 3.509 -0.110]	[0.736 0.163 -0.691 -0.065 -1.163 -0.978 -1.012 0.173 0.411 1.463]				
	[0.251 -1.177 2.782]	[-0.920 0.464 0.616 0.509 0.653 0.261 -1.092 -0.174 -0.155 -0.096]				
	[1.339 -2.444 -2.715]	[-2.365 -0.199 0.267 -1.724 0.173 -1.069 0.828 0.598 0.227 0.870]				
	[-1.525 1.977 2.194]	[-0.110 -1.286 -0.035 0.533 -0.359 0.038 1.562 0.377 -0.907 -1.083]				
	[2.903 -0.077 -2.836]	[-0.423 -0.074 1.366 0.524 0.171 -1.359 -0.125 -0.296 0.072 0.225]				
	[-0.896 2.287 1.382]	[-1.110 0.253 -0.935 0.249 -0.145 0.663 0.681 -0.719 -0.231 0.641]				
	[2.242 -0.719 1.493]	[0.599 -0.533 0.851 -0.217 0.680 0.949 -0.551 -1.376 0.439 0.297]				
SA ($T_n = 1.0s$)	[3.655 3.506 0.137]	[-1.482 0.862 2.061 -5.179 -2.552 2.095 0.475 1.271 -0.840 -1.432]	^T [0.081 0.137 -0.424 -0.124 -0.184 0.090 0.081 0.163 -0.046 0.100]	[-2.063 -2.433 -1.592 -0.598 -0.609 -0.146 -3.907 -1.872 4.147 3.378]	[3.125 0.684 0.170 1.057 -1.979 -1.578 -0.036 -1.445 -2.380]	[0.180]
	[3.371 4.949 -0.431]	[0.736 3.335 0.525 -0.781 -0.700 1.464 -0.039 2.426 1.417 2.211]				
	[0.868 -4.826 -2.522]	[-0.768 1.377 1.045 -0.798 -0.135 -1.514 0.294 -0.464 -0.332 -0.539]				
	[1.241 -0.876 -0.261]	[-0.511 2.096 -3.683 -0.383 3.655 -2.650 1.188 -1.748 0.123 -0.715]				
	[0.386 4.467 -0.583]	[2.310 -1.332 -0.879 -0.742 -0.438 -1.749 -0.688 0.338 0.830 -0.454]				
	[0.394 -0.229 0.209]	[-2.893 3.685 -4.077 0.616 -1.509 -1.471 -1.884 0.679 -0.818 0.392]				
	[-4.093 1.291 3.585]	[0.445 -0.913 1.673 1.618 -3.604 -1.164 -3.874 -2.019 -1.931 -1.765]				
	[0.274 -2.868 -2.607]	[0.125 1.110 1.111 0.528 -2.481 1.084 1.141 1.115 -1.714 -0.264]				
	[2.700 3.344 -2.763]	[-0.821 -0.842 -0.006 1.954 -2.364 -3.406 2.119 -1.170 -0.351 0.276]				
	[3.372 0.236 1.217]	[-2.626 0.883 2.018 0.837 0.032 -0.490 -1.535 -1.808 -0.646 -1.686]				
SA ($T_n = 1.5s$)	[-0.904 3.866 -0.944]	[0.878 0.722 -0.211 0.453 0.445 1.480 0.172 3.350 -0.080 1.836]	^T [-0.438 -0.390 -0.979 -1.764 -0.692 -1.486 -0.578 1.943 -0.898 0.998]	[-2.840 2.391 1.803 -1.779 -0.757 0.213 -1.583 -3.481 -3.157 -2.701]	[1.631 1.596 0.876 0.142 -0.209 0.128 1.118 -0.808 2.944 1.711]	[0.650]
	[-0.922 0.699 -3.588]	[1.251 -1.228 0.201 0.249 0.815 1.070 0.875 0.045 -2.285 0.083]				
	[-1.699 -1.149 -3.006]	[-0.832 -2.388 1.032 -0.519 -0.252 1.370 0.797 -0.344 -0.496 -0.127]				
	[-0.761 0.553 1.416]	[-0.318 -1.479 1.002 -0.582 -0.274 -0.803 -0.067 0.342 -0.289 0.347]				
	[-0.599 1.575 -1.682]	[1.725 0.762 0.220 0.189 0.006 -1.199 0.412 -1.543 1.949 0.735]				
	[-1.283 1.987 -3.340]	[-0.864 -0.904 -1.866 1.285 -0.037 0.558 -0.922 0.418 0.804 -0.640]				
	[-1.442 3.198 1.463]	[0.722 -0.104 -1.975 1.227 0.864 -0.106 -1.876 -0.612 -0.832 0.555]				
	[-4.101 -0.683 -2.028]	[-0.115 -1.564 0.057 -0.145 -0.906 -1.047 0.197 0.701 -0.237 0.513]				
	[-3.111 -1.363 0.235]	[-0.139 1.133 -1.658 0.098 1.128 1.120 0.573 -0.701 1.756 1.271]				
	[-2.997 0.019 -0.479]	[1.792 -0.343 0.074 0.260 -0.495 -0.330 -0.751 0.817 0.544 -0.744]				

Parallel numerical simulation of two-phase flow model in porous media using distributed and shared memory architectures

Luis Miguel de la Cruz* and Daniel Monsivais

Received: October 10, 2012; accepted: May 03, 2013; published on line: December 11, 2013

Resumen

En este trabajo se estudia un modelo de flujo bifásico (agua-aceite) en un medio poroso homogéneo considerando un desplazamiento inmisible e incompresible. Este modelo se resuelve numéricamente usando el Método de Volumen Finito (FVM) y se comparan cuatro esquemas numéricos para la aproximación de los flujos en las caras de los volúmenes discretos. Se describe brevemente cómo obtener los modelos matemático y computacional aplicando la formulación axiomática y programación genérica. También, implementa dos estrategias de paralelización para reducir el tiempo de ejecución. Se utilizan arquitecturas de memoria distribuida (clusters de CPUs) y memoria compartida (Tarjetas gráficas GPUs). Finalmente se realiza una comparación del desempeño de estas dos arquitecturas junto con un análisis de los cuatro esquemas numéricos para un patrón de flujo de inyección de agua, con un pozo inyector y cuatro pozos productores (five-spot pattern).

Palabras clave: flujo bifásico, medios porosos, recuperación de hidrocarburos, método de volumen finito, cómputo paralelo, Cuda.

Abstract

A two-phase (water and oil) flow model in a homogeneous porous media is studied, considering immiscible and incompressible displacement. This model is numerically solved using the Finite Volume Method (FVM) and we compare four numerical schemes for the approximation of fluxes on the faces of the discrete volumes. We describe briefly how to obtain the mathematical and computational models applying axiomatic formulations and generic programming. Two strategies of parallelization are implemented in order to reduce the execution time. We study distributed (cluster of CPUs) and shared (Graphics Processing Units) memory architectures. A performance comparison of these two architectures is done along with an analysis of the four numerical schemes, for a water-flooding five-spot pattern model.

Key words: two phase flow, porous media, oil recovery, finite volume method, parallel computing, Cuda.

L.M. de la Cruz*
D.Monsivais
Instituto de Geofísica
Departamento de Recursos Naturales
Universidad Nacional Autónoma de México
Ciudad Universitaria
Delegación Coyoacán, 04510
Mexico D.F., México
*Corresponding author: luiggix@gmail.com

Introduction

New recovery techniques (for example Enhanced Oil Recovery) are essential for exploiting efficiently oil reservoirs existing around the world. However, before these techniques can be successfully applied, it is fundamental to develop mathematical and computational investigations to model correctly all the processes that can occur. General procedures for constructing these mathematical and computational models (MCM) are presented in [1, 2], where it is shown that with an axiomatic formulation it is possible to achieve generality, simplicity and clarity, independently of the complexity of the system to be modeled. Once we have an MCM of the oil recovery process we are interested in, an efficient implementation of computer codes is required to obtain the numerical solution in short times.

Nowadays, the oil reservoir characterization technologies can produce several millions of data, in such a way that an accurate well-resolved simulation requires an increase on the number of cells for the simulation grid. The direct consequence is that the calculations are significantly slow down, and a very high amount of computer resources (memory and CPU) are needed. Currently, fast simulations on commercial software are based on parallel computing on CPU cores using MPI [3] and OpenMP [4]. On the other hand, since the introduction of the CUDA language [5], high-performance parallel computing based on GPUs has been applied in computational fluid dynamics [6, 7], molecular dynamics [8], linear algebra [9, 10], Geosciences [11], and multiphase flow in porous media [12, 13, 14, 15, 16] among many others.

The water-flooding technique is considered as a secondary recovery process, in which water is injected into some wells to maintain the field pressure and to push the oil to production wells. When the oil phase is above the bubble pressure point, the flow is two phase immiscible and there is no exchange between the phases, see [17]. Otherwise, when the pressure drops below the bubble pressure point, the hydrocarbon component separates into oil and gas phases. The understanding of the immiscible water-flooding technique is very important and still being studied as a primary benchmark for new numerical methods [18] and theoretical studies [19]. Besides, some authors have started to investigate parallel technologies to reduce the execution time of water-flooding simulations, see for example [7, 13, 15, 20].

The incorporation of the GPUs into the floating point calculation of the oil reservoir simulation, has been considered in several studies. For example, in [20] a model for two-phase, incompressible,

immiscible displacement in heterogeneous porous media was studied, where an operator splitting technique, and central schemes are implemented on GPUs producing 50-65 of speedup compared with Intel Xeon Processors. In [13], a very similar study as ours is presented, where the IMPES method is used to linearize and decouple the pressure-saturations equation system, and the SOR method is applied to solve the pressure equation implicitly. Their implementations was done considering a partition of the domain and then distributing each subdomain to blocks of threads. They obtain considerable accelerations (from 25 to 60.4 times) of water-flooding calculations in comparison with CPU codes. Multi-GPU-based double-precision solver for the three-dimensional two-phase incompressible Navier-Stokes equations is presented in [7]. Here the interaction of two fluids are simulated based on a level-set approach, high-order finite difference schemes and Chorin's projection method. They present an speed-up of the order of three by comparing equally priced GPUs and CPUs.

The numerical application studied in this paper, is the well known five-spot pattern model, and we work this model in the limit of vanishing capillary pressure, applying Darcy's law coupled to the Buckley-Leverett equation. This assumption generates an hyperbolic partial differential equation which can presents shocks in its solution. Our approach for solving this equation is to use four numerical schemes for approximating the fluxes adequately on the faces of the discrete volumes. We are interested in to study the numerical throughput of these four numerical schemes. We also focus our attention in the comparison of two parallel implementations written to run on a high-performance architecture consisting of CPUs and GPUs. We made this comparison in equality of conditions in order to do an objective analysis of the performance. The parallel implementations we present, are based on the use of well established opensource numerical libraries for solving linear systems. We use PETSc [21, 22] for distributed memory and CUSPARSE [24, 23] for GPU shared memory. We coupled these two libraries to our software TUNAM [25, 26], which implements FVM from a generic point of view. With this software we can easily implement, incorporate and evaluate the four numerical schemes for the approximation of the fluxes on the faces. Our objective is to give a quantitative reference that can be reproduced easily, and applied to other applications.

This paper is structured as follows. In section 2, we discuss the mathematical modeling of multiphase flows in porous media. The presentation is based on the axiomatic formulation introduced in [1, 2], and a pressure-saturation formulation is described for the two-phase flow. In section 3, the FVM is applied to the mathematical model, and the four numerical

schemes for approximating the fluxes on the faces are introduced. We also explain the IMPES method used to obtain the solutions. The computational implementation of the algorithms, including our parallel implementations are also explained. In section 4, we solve the five-spot model using the four numerical schemes in combination with a linear and quadratic relative permeability models. In section 5, an analysis of the performance of our parallel implementations is done. Finally, in section 6 we give our conclusions.

Governing equations of a multiphase system

Given an intensive property ψ and a reference body $B(t)$ of a continuous system, the general balance equation, in conservative form see [27], can be written as follows

$$\int_{B(t)} \frac{\partial \psi}{\partial t} dx + \int_{B(t)} \nabla \cdot \underline{\mathcal{F}} dx = \int_{B(t)} q dx, \quad (1)$$

where x represents the position and t is the time. In equation (1) the *flux function* is defined as $\underline{\mathcal{F}} = v\psi - \tau$, and the quantities $v(x, t)$, $q(x, t)$ and $\tau(x, t)$ represent the velocity of the particles of $B(t)$, the generation and the flux of property ψ , respectively (see [1] for a complete description on this formulation).

In a multiphase porous media system, the mass of fluid of the phase α is an extensive property M_α , and the corresponding intensive property is ψ_α . Both properties are related as follows

$$M_\alpha = \int_{B(t)} \psi_\alpha dx,$$

where the intensive property is defined as $\psi_\alpha = \phi \rho_\alpha S_\alpha$. Here ϕ is the porosity, ρ_α and S_α are the density and the saturation of phase respectively.

From equation (1), and using the fact that $B(t)$ is arbitrarily chosen, the conservative form of the balance equation for the mass of fluid of the phase α is

$$\frac{\partial(\phi \rho_\alpha S_\alpha)}{\partial t} + \nabla \cdot (\underline{\mathcal{F}}_\alpha) = q_\alpha, \quad (2)$$

where the flux function $\underline{\mathcal{F}}_\alpha$ is defined as

$$\underline{\mathcal{F}}_\alpha = -\rho_\alpha \underline{k} \lambda_\alpha (\nabla p_\alpha - \rho_\alpha \wp \nabla \mathcal{D}) - \tau_\alpha, \quad (3)$$

In equation (3) we have introduced the Darcy's law for multiphase systems

$$\underline{u}_\alpha = -\underline{k} \lambda_\alpha (\nabla p_\alpha - \rho_\alpha \wp \nabla \mathcal{D}), \quad (4)$$

where λ_α is the mobility of the phase α defined as $\lambda_\alpha = k_{r\alpha} / \mu_\alpha$. Here $k_{r\alpha}$ is the relative permeability of phase α . The viscosity, the pressure and the density of phase α are denoted by μ_α , p_α and ρ_α , respectively. The tensor \underline{k} is the absolute permeability. The symbol \wp is the magnitude of earth gravity and \mathcal{D} represents the depth of the porous media, see [17]. We also used the Darcy's velocity of phase α defined as $\underline{u}_\alpha = v \phi S_\alpha$.

Pressure equation

Equation (2) represents a fully-coupled system of N_p phases. Using a pressure-saturation formulation, see [17], it is possible to decouple the N_p equations into one for a phase pressure and $N_p - 1$ for saturations. These equations will be weakly coupled and can be solved iteratively.

In order to obtain a pressure equation, we start from equation (2) and neglecting the diffusion $\tau_\alpha = 0$, dividing by ρ_α and summing over all phases, we obtain

$$\sum_{\alpha=1}^{N_p} \left\{ \frac{1}{\rho_\alpha} \left[\frac{\partial(\phi \rho_\alpha S_\alpha)}{\partial t} + \nabla \cdot (\rho_\alpha \underline{u}_\alpha) - q_\alpha \right] \right\} = 0,$$

Developing the derivatives and using the fact that we obtain the phase pressure equation

$$\begin{aligned} \frac{\partial \phi}{\partial t} - \sum_{\alpha=1}^{N_p} \nabla \cdot (\underline{k} \lambda_\alpha (\nabla p_\alpha - \rho_\alpha \wp \nabla \mathcal{D})) \\ + \sum_{\alpha=1}^{N_p} \frac{1}{\rho_\alpha} \left[\phi S_\alpha \frac{\partial \rho_\alpha}{\partial t} + \underline{u}_\alpha \cdot \nabla \rho_\alpha \right] - \sum_{\alpha=1}^{N_p} \frac{q_\alpha}{\rho_\alpha} = 0. \end{aligned} \quad (5)$$

where the Darcy's law was written explicitly.

Saturation equation

The solution of equation (5) produce the pressure for a phase α . Other phase pressures can be obtained via the capillary pressure relations

$$p_{c\alpha_1\alpha_2} = p_{\alpha_1} - p_{\alpha_2}, \alpha_1 \neq \alpha_2, \quad (6)$$

where α_1 represent a *non-wetting* phase and α_2 represent a *wetting* phase.

Using the phase pressures we can calculate the velocities via Darcy's Law, equation (4). This velocity is necessary to solve the saturation equations (2), which can be written as follows

$$\frac{\partial(\phi\rho_\alpha S_\alpha)}{\partial t} - \nabla \cdot (\rho_\alpha k \lambda_\alpha (\nabla p_\alpha - \rho_\alpha \phi \nabla \mathcal{D})) - q_\alpha = 0, \quad (7)$$

Incompressible two-phase pressure-saturation model

Two-phase flow in porous media modeling is concerned to the displacement of one fluid by another. In general, a wetting fluid, say water, is injected into the porous media displacing a non-wetting fluid, say oil, which is being extracted at another location. Due to the physical interaction between the two phases, this process generates a moving front at the interface between the phases. The evolution of the front is of primary interest for the production of hydrocarbons in oil recovery field.

We consider two incompressible and immiscible phases: water (w) and oil (o) in a porous media of constant porosity ϕ . Equations are commonly posed in terms of the field variables oil pressure and water saturation as follows

$$\nabla \cdot \underline{\mathcal{F}}_1 = Q_w + Q_o, \quad (8)$$

$$\phi \frac{\partial(S_w)}{\partial t} + \nabla \cdot \underline{\mathcal{F}}_2 = Q_w, \quad (9)$$

where

$$\underline{\mathcal{F}}_1 = -k \left(\lambda \nabla p_o - \lambda_w \frac{dp_{cow}}{dS_w} \nabla S_w - (\lambda_w \rho_w + \lambda_o \rho_o) \phi \nabla \mathcal{D} \right)$$

$$\underline{\mathcal{F}}_2 = -k \left(\lambda_w \nabla p_o - \lambda_w \frac{dp_{cow}}{dS_w} \nabla S_w - \lambda_w \rho_w \phi \nabla \mathcal{D} \right)$$

and the source terms are defined as $Q_w = q_w / \rho_w$ and $Q_o = q_o / \rho_o$. The capillary pressure is defined as $p_{cow}(S_w) = p_o - p_w$ and because it depends on water saturation, it is possible to write $\nabla p_{cow} = (dp_{cow} / dS_w) \nabla S_w$. Equations (8) and (9) are coupled and non-linear. In order to decouple and linearize those equations, we employ the IMPES method, which will be explained in the next section. Note that equations (8) and (9) are simplified versions of equations (5) and (7), respectively.

Numerical model

The numerical formulation of the equations (8) and (9) is based on the finite volume method (FVM) which is derived on the basis of the integral form of the global balance equation (1), see [28, 29, 27].

In the FVM we keep track of an approximation to the integrals of equation (1) over each control

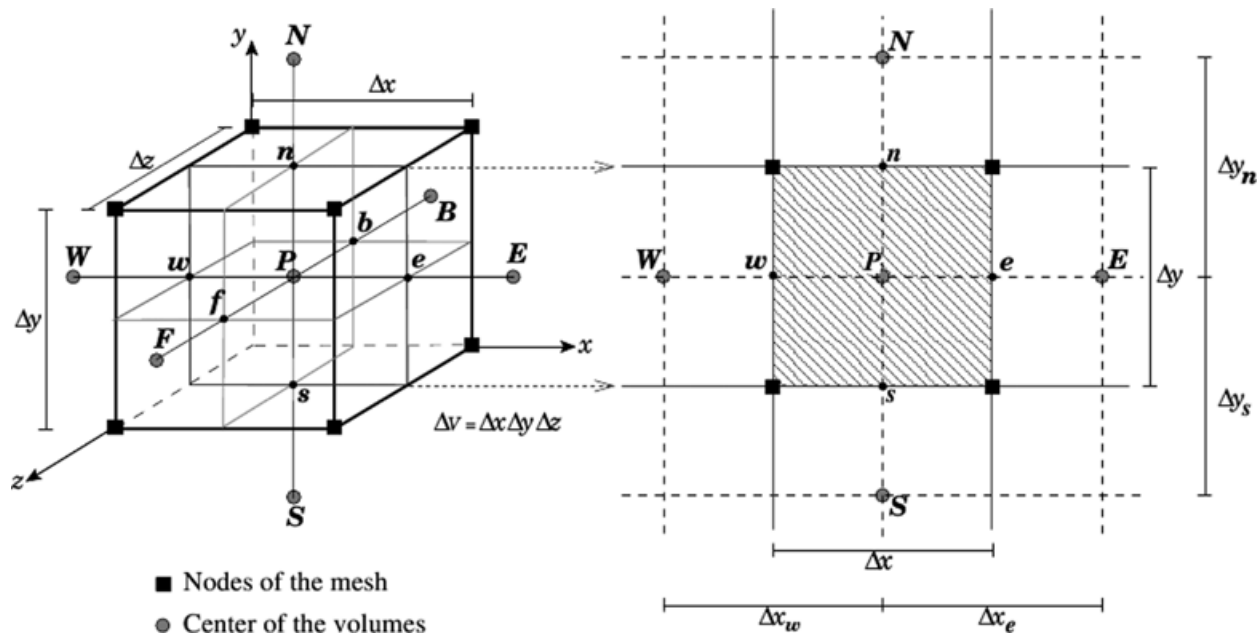


Figure 1. Control volume: black squares represent the nodes commonly used in finite differences or finite element methods. The center of the volumes (circles) are labeled with uppercase letters, meanwhile the faces are labeled using lowercase letters.

volume, see figure 1. Every time step, we update these values using approximations to the fluxes throughout the faces of the volumes. When the approximations are calculated in a control volume, we transform the original equations into a set of algebraic equations.

Applying FVM to equation (8), and using the notation and we obtain the next discrete pressure equation

$$a_P^n p_P^{n+1} = a_E^n p_E^{n+1} + a_W^n p_W^{n+1} + a_N^n p_N^{n+1} + a_S^n p_S^{n+1} + a_F^n p_F^{n+1} + a_B^n p_B^{n+1} + f_P^n, \quad (10)$$

where the superscript is the time step and the subscripts indicate the node of the mesh according to figure 1. Equation (10) was obtained for a fully implicit temporal scheme and assuming that the a_{NB}^n coefficients, for $NB \in \{P, E, W, N, S, F, B\}$, can be calculated from values of the fluxes at instant n . The shape of a_{NB}^n coefficients depends on the numerical schemes used to approximate the fluxes on the control volume faces. In obtaining equation (10) we use the fact that the pressure equation is coupled with the saturation one, in such a way that, even though there is not temporal term in equation (8), we need to update the pressure field when a new saturation field is obtained.

The discretized form of equation (9) using FVM is

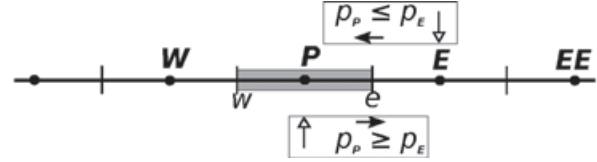
$$S_P^{n+1} = S_P^n + b_P^n S_P^n - (b_E^n S_E^n + b_W^n S_W^n + b_N^n S_N^n + b_S^n S_S^n + b_F^n S_F^n + b_B^n S_B^n) - c_P^n p_P^n + (c_E^n p_E^n + c_W^n p_W^n + c_N^n p_N^n + c_S^n p_S^n + c_F^n p_F^n + c_B^n p_B^n) + d_P^n D_P^n - (d_E^n D_E^n + d_W^n D_W^n + d_N^n D_N^n + d_S^n D_S^n + d_F^n D_F^n + d_B^n D_B^n) + \bar{Q}_w \left| P \frac{\Delta t}{\phi} \right. \quad (11)$$

The shape of the coefficients for equations (10) and (11) are given in appendix A.

Numerical schemes for water saturation

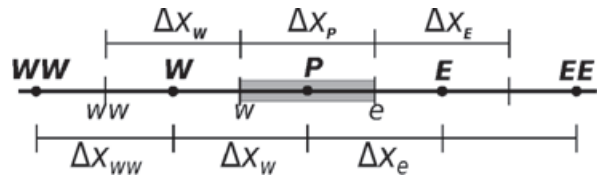
Coefficients of equations (10) and (11) depends on the mobilities and capillary pressure evaluated on the faces of control volumes. These coefficients in turn depend on the water saturation, S_w , which is an unknown of the system of equations, and is updated every time iteration at the center of the volumes. In order to calculate the mobilities and the capillary pressure we require the value of S_w on the faces of volumes. There exist several approaches to evaluate S_w on the faces, and in this work we implemented four numerical schemes which are described below.

Upwind : linear upstream; for example for face e we have



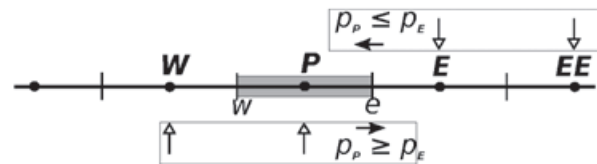
if ($p_P^n \leq p_E^n$) then
 $S_e^n = S_E^n$
 else
 $S_e^n = S_P^n$
 end if

Average : a weighted average is done using the neighbors to point P ; for example for face e we have



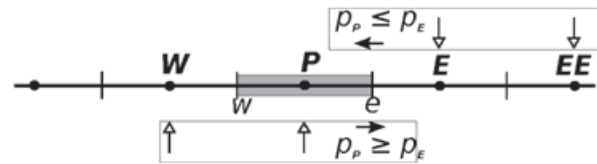
$$S_e^n = \beta S_E^n + (1 - \beta) S_P^n$$

where $\beta = (x_e - x_p) / \Delta x_e$.



UpwindE : quadratic upstream with extrapolation [30]; for example for face e we have

if ($p_P^n \leq p_E^n$) then
 $S_e^n = S_E^n (1 - \beta_E) - S_{EE}^n \beta_E$
 else
 $S_e^n = S_P^n (1 - \beta_P) - S_W^n \beta_P$
 end if



where $\beta_P = \Delta x_P / 2\Delta x_w$ and $\beta_E = \Delta x_E / 2\Delta x_{ee}$.

UpwindQ : cubic upstream [31]; for example for face e and uniform meshes we have

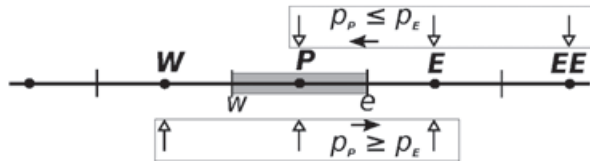
if ($p_P^n \leq p_E^n$) then
 $S_e^n = -\frac{1}{8} S_{EE}^n + \frac{3}{4} S_E^n + \frac{3}{8} S_P^n$

```

else

$$S_e^n = -\frac{1}{8} S_W^n + \frac{3}{4} S_P^n + \frac{3}{8} S_E^n$$

end if
    
```



Solution method

The IMPES (*IMplicit Pressure, EXplicit Saturation*) method is very used for solving two phase flow models of incompressible or slightly compressible fluids, see [17, 30]. As presented in sections §2.1 and §2.2, we can formulate our problem in terms of one equation for a phase pressure and $N - 1$ equations for phase saturations. In the IMPES method, for the two-phase case, we solve the pressure equation (8) implicitly and the saturation equation (9) explicitly. In order to solve the pressure equation, we use an initial saturation, and once the pressure is obtained, we can use it to solve the saturation equation. This process linearize and decouple the system of equations and is done iteratively for a given number of time steps. The IMPES method is given in algorithm (1).

Algorithm 1 IMPES

- 1: Initial data: S^0, p^0, T_{max} and Δt .
- 2: $n \leftarrow 0$.
- 3: **while** $t < T_{max}$ **do**:
- 4: Calculate the coefficients of equation (10) using S^n .
- 5: Solve discrete pressure equation (10) implicitly to obtain p^n .
- 6: Calculate the coefficients of equations (11) using p^n and S^n .
- 7: Solve discrete saturation equation (11) explicitly to obtain S^{n+1} .
- 8: $t^{n+1} \leftarrow t^n + \Delta t$.
- 9: $n \leftarrow n + 1$.
- 10: **end while**

Even though that it is possible to use different time steps for pressure and saturation equations, here we use the same time step in order to

evaluate the total elapsed time of pressure and saturation solution, when both are obtained for the same number of iterations.

Computational implementation

We use the software TUNAM [25] to implement the FVM applied to the equations described in previous sections. The TUNAM library use object-oriented and generic programming, in such a way that it is possible to extend its functionality to solve many sort of problems. In TUNAM there are three main concepts: *Generalization*, *Specialization* and *Adaptors*, which are related through the application in two levels of the *Curiously Recurring Template Pattern* [32].

The main generalization in TUNAM is the `GeneralEquation` concept, which refers to the general balance equation (1) and its FVM discrete formulation represented by equations (10) and (11). In principle, this general concept accounts for all the FVM coefficients. We inherit from this concept the `TwoPhaseEquation`, which is an specialization that includes all particular features of the two-phase model described in section §2.3. Because we are interested in to analyze the performance of the four numerical schemes described in section §3.1, we implement eight adaptors resumed in table 3.

Next two lines of code explains how the pressure and saturation equations are defined in the TUNAM framework

```

TwoPhaseEquation<FSIP1<double, 3> >
pressure(p, A, b, mesh);
TwoPhaseEquation<FSES1<double, 3> >
saturation(Sw, A, b, mesh);
    
```

The pressure and saturation equations are defined in lines 1 and 2 of the above code, respectively. These equations are defined in terms of the objects `p` (pressure field), `sw` (saturation field), `A` (matrix of algebraic system), `b` (source term) and `mesh` (mesh of the domain). The template parameters `FSIP1` and `FSES1` are two adaptors that define the shape of the coefficients of equations (10) and (11). We can use any of the adaptors listed in table 3, and the change in the code would be only in lines 1 and 2 (for example we can use `FSIP2` and `FSES2`, instead). For more details of the TUNAM framework see [26].

Using the objects `pressure` and `saturation` the IMPES method is implemented in the next simple manner:

```

while (t <= Tmax) {
    pressure.calcCoefficients();
    Solver::TDMA3D(pressure, tol, maxIter);
    pressure.update();
}
    
```

```

saturation.calcCoefficients();
Solver::solExplicit3D(saturation);
saturation.update();
t += dt;
}

```

Parallel implementation

Inside the IMPES algorithm (1), the step 5 is the most time consuming task. In the TUNAM code, related to the IMPES cycle as described in sections §3.2 and §3.3, the solution of the pressure equation can be achieved by different approaches. Due to the size of the problem, the use of iterative algorithms is usually the fast (and many times the only) way to get the solution vector. Among these, is the BiCGStab [33], a Krylov sub-space method, which gave us the better time convergence and stability than other similar methods. This solver method can be implemented easily in parallel exploiting different type of architectures. In this work, we study the performance of two memory architectures: a distributed memory of a cluster via the PETSc library[21, 22]; and a shared memory architecture of a Graphics Processing Unit (GPU) using the CUSPARSE library[24, 23], which is based on CUDA.

The linear algebra operations contained in a regular iteration of the BiCGStab method (without preconditioning) are listed in the table 1, as well as the number of times each operation is called inside the iteration. Using PETSc¹ and CUDA libraries we wrote down two codes with the same operations, as shown in table 1, in order to achieve the BiCGStab algorithm, see appendix B. Also, the same type of matrix's compression format was used to fix down the same conditions for both codes. In this case, the most time-consuming operations are the 2 matrix-vector product.

The Compressed Row Storage (CRS) format[34] was used to store the matrix of the linear system. In the CRS, the non-zero elements are stored in a linear array A^* , and an auxiliary array J^* is used to keep the column number j of each element of

A^* . In order to know the row of every element stored, a third array I^* is used. This array keeps the segmentation of the array A^* in elements of the same row in the original matrix A , i.e. the position in the array A^* of the first non-zero element of each row. For diagonal matrices, the growth in size of the data stored is $O(n)$, against the $O(n^2)$ of the non-compressed counterpart.

We adapted the TUNAM code described in section §3.3 for using PETSc and CUDA. At the very beginning of each IMPES iteration, just after updating the matrix and vectors of the linear system for pressure, the containing arrays from TUNAM were handled to conform the format required by the two evaluated parallel libraries. The explicit solution of the saturation equation, can be expressed as a set of linear algebra operations (see appendix C). In this approach, the saturation vector S at time $n + 1$, is calculated as follows

$$S^{n+1} = S^n - \underline{\underline{B}}^n S^n - \underline{\underline{C}}^n p^n + \underline{\underline{D}}^n d^n + \bar{Q}_w \frac{\Delta t}{\phi}, \tag{12}$$

where S , p , d , \bar{Q}_w are vectors corresponding to equation (11) and $\underline{\underline{B}}$, $\underline{\underline{C}}$, $\underline{\underline{D}}$ are diagonal-banded matrices (see Appendix B) containing respectively, the coefficients b_{NB}^n , c_{NB}^n and d_{NB}^n . The linear operation (20) was translated to an equivalent parallel implementation, with 5 axpy's operations and 3 matrix-vector products.

Application to the five-spot pattern

Waterflooding is classified as a secondary oil recovery technique, which consists in the injection of water into the reservoir through injectors wells, pushing the hydrocarbons into the rocks and forced to flow towards the producers wells.

A simplified, but realistic two-phase flow model, is that from Buckley and Leverett [35], where we have two immiscible and incompressible

Table 1. Operations used in the BiCGStab and number of calls for each one of them inside the method.

Copy	Scale	Dot product	Norm	Axpy	Matrix-Vector
$y \leftarrow x$	$x \leftarrow \alpha x$	$c \leftarrow x \cdot y$	$x \leftarrow \ x\ $	$y \leftarrow \alpha x + y$	$y \leftarrow \alpha \underline{\underline{A}}x + y$
2	1	4	2	6	2

¹Despite of PETSc has a BiCGStab implementation, these includes operations not present in CUBLAS, as WAXPY

fluids, the diffusivity and capillary pressure effects are ignored, and the gravity is neglected. With these considerations pressure equation (8) is elliptic, whilst saturation equation (9) is hyperbolic and may develop discontinuities in the solution. Applying the model of Buckley-Leverett, we studied the well established five-spot pattern. The domain of study is a parallelepiped domain, where four producers wells are located in the corners, and one injector well is in the center of the domain. Due to the symmetry only a quarter of the domain is simulated. The complete data set was taken from [18] and is resumed in table 2.

Relative permeability model

We use the Corey's model [36] to evaluate the

Table 2. Quarter five-spot data.

Parameters	Values SI units
Dimension for x -axis and y -axis	182.76 [m]
Dimension for z -axis	9.14 [m]
Water injection rate (\bar{Q}_w)	3.86×10^{-04} [m ³ /s]
Absolute permeability (\bar{k})	0.9869×10^{-15} [m ²]
Porosity (ϕ)	0.2 -
Water (μ_w) and Oil (μ_o) viscosities	1.0×10^{-03} [Pa s]
Water residual saturation (S_{rw})	0 -
Oil residual saturation (S_{ro})	0.2 -

relative permeabilities. This model is defined as follows

$$k_{rw} = S_e^n \text{ and } k_{ro} = (1 - S_e)^\sigma$$

where the effective saturation is defined as $S_e = (S_w - S_{rw}) / (1 - S_{rw} - S_{ro})$.

Table 3 shows the adaptors implemented in TUNAM for this work, which combine the relative mobility model for and $\sigma = 1$, and 2 the numerical schemes presented in section §3.1.

Numerical results

Figures 2 and 3 show the distribution of water

Table 3. Numerical schemes evaluated and implemented in TUNAM.

Numerical Scheme	Adaptors			
	$\sigma = 1$		$\sigma = 2$	
	p	S	p	S
Upwind	FSIP1	FSIS1	FSIP2	FSIS2
Average	FSIP3	FSIS3	FSIP4	FSIS4
UpwindE	FSIP5	FSIS5	FSIP6	FSIS6
UpwindQ	FSIP7	FSIS7	FSIP8	FSIS8

saturation after 600 days of simulation, for the cases lineal ($\sigma = 1$) and quadratic ($\sigma = 2$), respectively. The numerical schemes Upwind, Average, UpwindE and UpwindQ are presented in graphics (a), (b), (c) and (d) respectively of those figures. In the linear case, the water front is well behaved independently of the numerical scheme. Figure 4(a) presents the profiles of water saturation for the linear case, along a line joining the injector and extractor wells. We observe in this figure that all the four schemes are very similar; UpwindE scheme introduce a numerical diffusion, producing an smeared solution; the other three schemes approximate the water front more accurate, and the best is UpwindQ, which is $O(\Delta x^3)$. On the other hand, for the case $\sigma = 2$, figures 3(a) and (c) show similar distribution, while graphics (b) and (d) have a non-realistic behavior. This is more clear in figure 4(b). High-order schemes provide accurate approximation of the front, but when they are used in isolation will usually result in physically meaningless solutions. The situation arises from the violation of the so called "entropy condition", and to solve it a monotonicity constraint is required, see [37]. We do not address this problem in this work. The numerical scheme UpwindE produce the best solution for $\sigma = 2$.

Performance analysis

All the results presented in this section were obtained by executing our codes in a cluster with 216 (Intel(R) Xeon(R) CPU X5650 2.67GHz) cores. The interconnection between the nodes of the cluster is Gigabit Ethernet. Moreover, the cluster has a TESLA M4050 GPU, with 448 cuda cores. The parameters for the simulation were the same as those in the table 2. The number of volumes in the x , y , and z directions were 320, 320, and 16 respectively, given a total of 1638400 cells. We reach the memory limit of the GPU using this number of volumes.

Linear algebra operations

The most time-consuming linear algebra operations used inside the BiCGSTab (see table 1), for a fixed number of volumes, were evaluated. This evaluation gave us the optimal number of processors for using the PETSc library in our cluster. Using matrices and vectors of the same size, as those used in the whole two-phase simulation, a PETSc implementation of each linear algebra operation from table 1, was analyzed in terms of the average FLOPs (floating point operations per second) measured over 10000 executions, for a distinct number of cores (between 1 and 216). Next, the average FLOPs of same linear algebra operations for the CUSPARSE implementation were measured using the same parameters as with PETSc. The matrix-vector

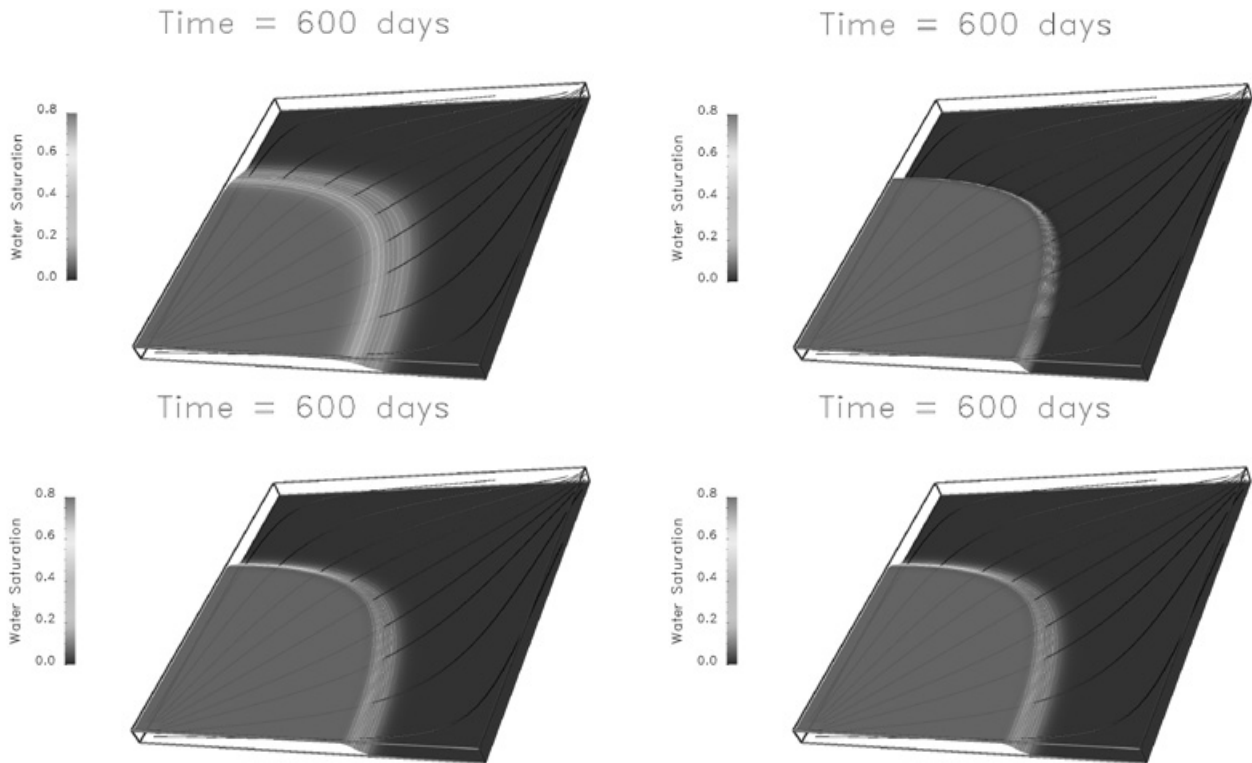


Figure 2. Water saturation for $\sigma = 1$. (a) Upwind scheme; (b) Average scheme; (c) UpwindE scheme; (d) UpwindQ scheme. Black lines represent the streamlines from the injector to the extractor wells.

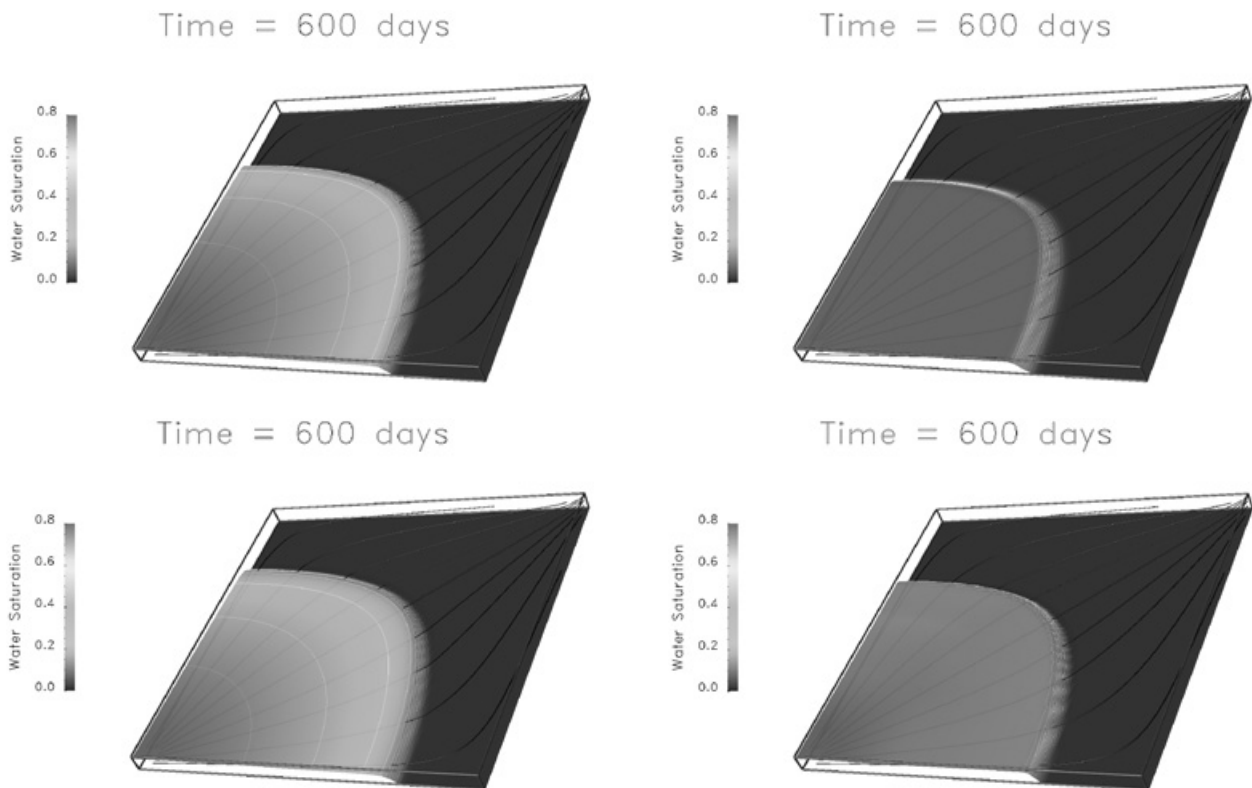


Figure 3. Water saturation for $\sigma = 2$. (a) Upwind scheme; (b) Average scheme; (c) UpwindE scheme; (d) UpwindQ scheme. Black lines represent the streamlines from the injector to the extractor wells.

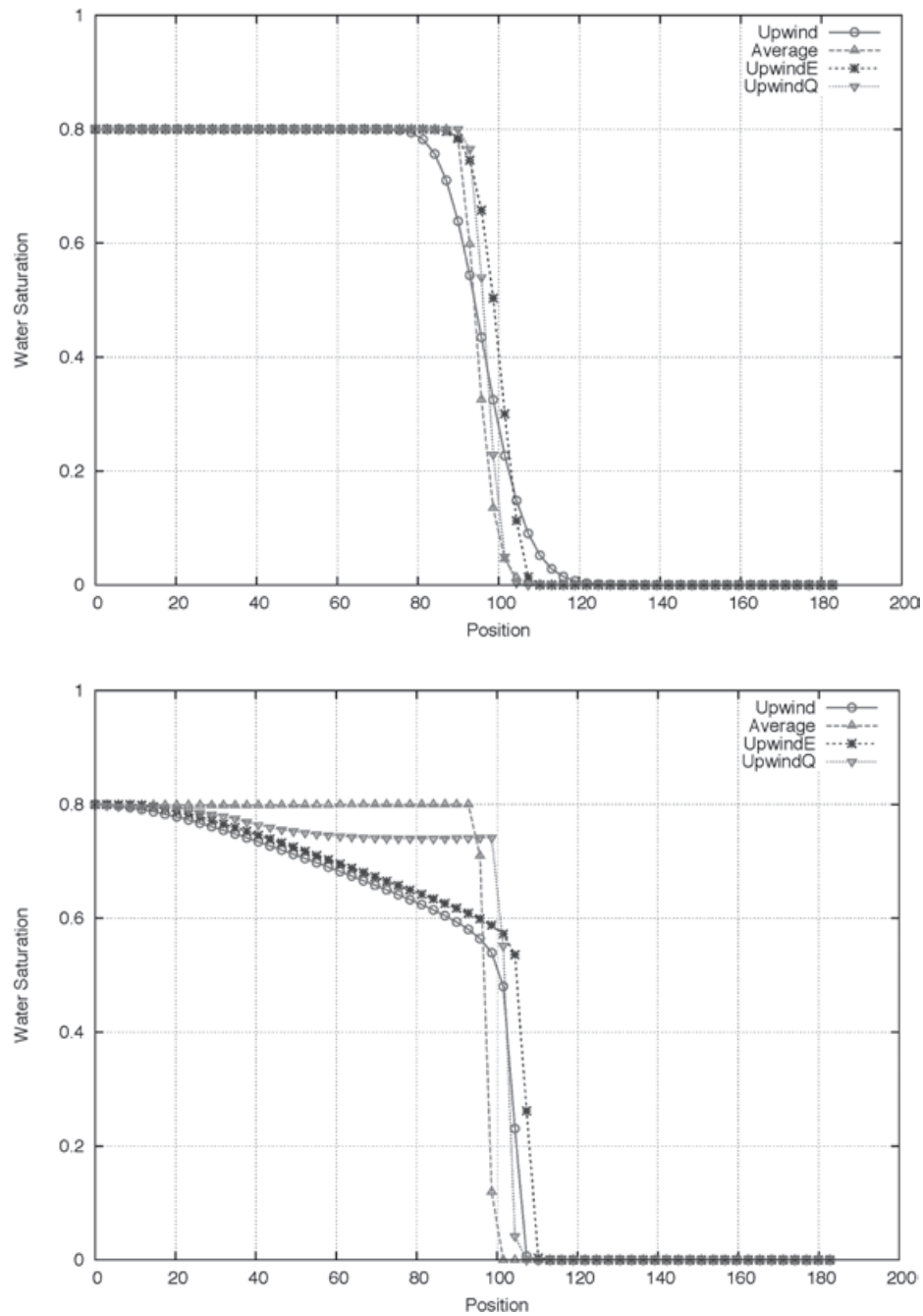


Figure 4. Water saturation profiles along a line joining the injector and extractor wells, after 600 days of simulation. (a) $\sigma = 1$ and (b) $\sigma = 2$.

product, axpy operation, dot product and norm of a vector performances are shown respectively in graphics a), b), c) and d) of the figure 5. In all graphics, the results of the CUSPARSE operations are shown as a horizontal line (blue), because the number of cores is fixed in a GPU, giving us only one point to compare with. On the other hand, for the PETSc library it is possible to measure the FLOPs with several number of processor, and we have at most 216 in our cluster.

Convergence speed of the four numerical schemes

During the simulation, the evolution of the water front (shock) depends on the numerical scheme used to calculate the water saturation on the volume's faces, see section §3.1. The saturation field and each numerical scheme generates different conditions for the calculation of coefficients of discrete pressure equation. As a consequence, the linear system to be solved in the iterative process of the BiCGStab, will change its condition number depending particularly on

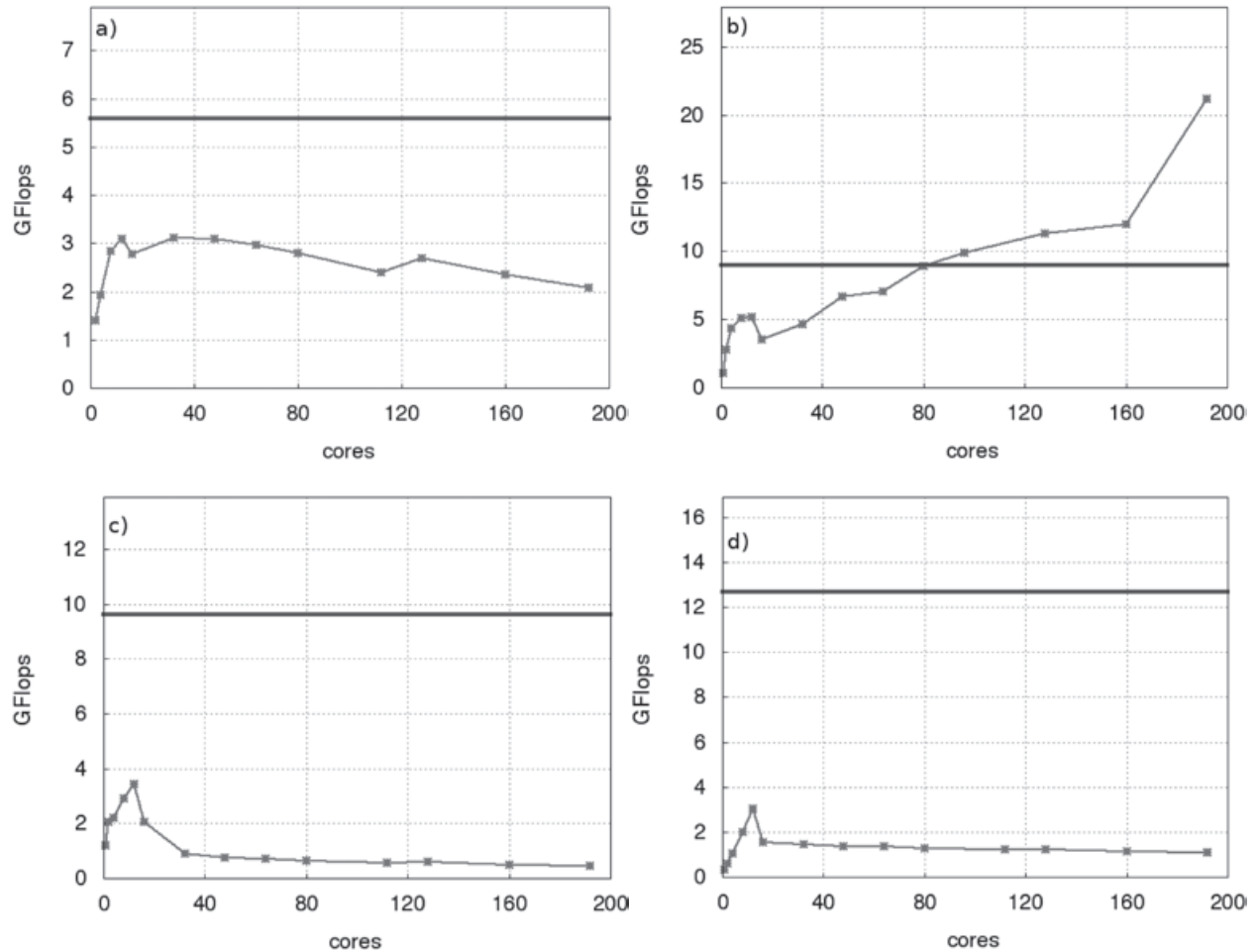


Figure 5. Average FLOPs as a function of number of cores: a) matrix-vector product, b) axpy operation, c) dot product, and d) norm of a vector. In all cases, the horizontal line (blue) represents the FLOPs obtained with the CUDA implementation and the broken line represents the PETSc implementation. All operations were executed with vectors and matrices corresponding to a mesh of $320 \times 320 \times 26 = 1638400$ cells.

the numerical scheme. The profiles of the water front at a fixed time, using the four different numerical schemes described in section §3.1, was shown in the figure 4, where the scheme-dependence is clear. In order to take into account this dependence, in table 4 we show the average number of iterations done by the BiCGStab method to converge using a tolerance (relative error) of 10^{-7} , for each one of the four numerical schemes. We also report the condition number of the matrix generated by each one of the numerical schemes. The average is calculated over the total number of IMPES iterations (1200 steps) and a mesh of $80 \times 80 \times 4$. The remaining data were the same as in table 2.

We observe from table 4 that the linear case, $\sigma = 1$, do not present any kind of complications, and the condition number and the average number of iterations is the same for all the four schemes. On

the other hand, the case $\sigma = 2$ give us different numbers for different schemes. It can be observed that the best behaved scheme is the UpwindE, as we already observed in section §4.2.

We do not present the results for the case UpwindQ with $\sigma = 2$, because it was not able to converge. As we pointed out before, this implementation does not contains the monotonicity constrain and therefore the results are unrealistic for this case. Similar comments are valid for the Average with $\sigma = 2$, but in that case we do not obtain convergence, although the numbers are not useful because it also presents a similar behavior as the UpwindQ scheme.

SpeedUp of the parallel IMPES method

The solving time for the pressure and saturation equations, during the simulation for PETSC and

Table 4. Average number of iterations (AI) taken by BiCGStab to converge using a tolerance of 10^{-7} for each one of the four numerical scheme; CN stands for the condition number of the matrix generated by each numerical scheme.

Numerical Scheme	$\sigma = 1$		$\sigma = 2$	
	AI	CN	AI	CN
Upwind	206.00	7399.59	304.61	7897.30
Average	206.00	7399.59	300.03	7853.45
UpwindE	206.00	7399.59	273.68	7450.28
UpwindQ	206.00	7399.59	-	-

CUSPARSE are shown in the figure 6. We use non-dimensional time, defined as the ratio between the greater time (for one core in PETSc) between the times obtained for each number of cores. Again, the horizontal line (blue) represent the CUSPARSE result. Taking as reference the execution time with one core in the PETSc implementation, the speedup analysis is shown in the bottom graphic of the figure 6.

Here the speedup is defined as the ratio between the time taken to solve the pressure and saturation equations in a serial process, divided by the time taken in a parallel process (448 cores for CUDA and n cores for PETSc, with $1 \leq n \leq 192$). All operations were executed with vector and matrices corresponding to a mesh of 1638400 nodes.

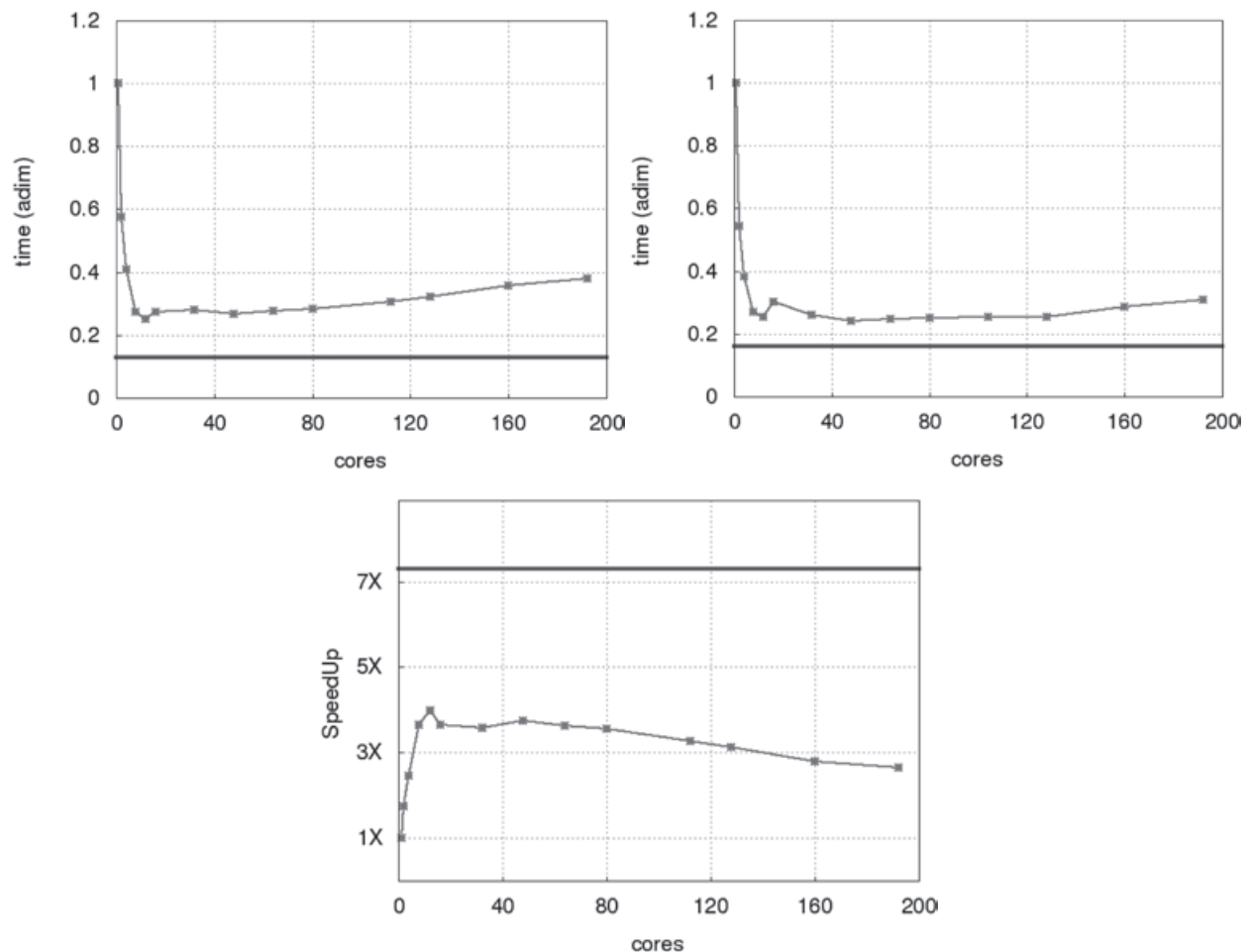


Figure 6. Top-left: Average non-dimensional time to complete the pressure solution (BiCGstab). Top-right: Average non-dimensional time to solve saturation. Bottom: Speedup of whole the parallel implementation. The horizontal (blue) line represents the CUSPARSE results, meanwhile the red line is for PETSc.

In figure 6 we observe that the best performance is obtained on the GPU for a fixed problem size. The speedup is almost 8 times in relation with the serial code. For the PETSc implementation, we observe that the peak performance is obtained for 12 processors. After that, the speedup starts to decrease monotonically as the number of processors is increased. This effect is due to the fact that the size of the problem is fixed and this size is tied to the memory of the GPU. When we increase the number of processor, the number of grid cells assigned to each processor by PETSc is reduced, and therefore, the communications between processors will have more impact on the execution time than the floating operations. We also recall that the interconnection of the cluster is not a high-end technology (for example infiniband), then is expected a reduction on the speedup when we increase the communications. Each node of our cluster contains 12 independent CPUs, which share memory. Hence, the results shown in figure 6 are compatible with the architecture of the cluster. Our conclusion here is that, in equality of conditions, a GPU TESLA M4050 GPU give us double of speedup than a node composed of 12 Intel Xeon processors, using CUSPARSE and PETSc as was described in the previous sections.

Conclusions

In this work we investigated the impact of four numerical schemes on the solution of a two-phase flow in an homogeneous porous media. Our study was focus on two objectives: 1) accuracy of the numerical scheme; and 2) performance in parallel using two memory architectures.

For the first objective, we found that the UpwindQ scheme, which is third order, gives the better approximation to the water-oil front than the other three, for the linear permeabilities model ($\sigma = 1$). In this case, all the schemes work fine, although some of them introduce numerical diffusion which smears the numerical solution. For the quadratic permeability model ($\sigma = 2$), it was observed that the best scheme was UpwindE, which is second order, and the Average and UpwindQ present unrealistic solutions due to the lack of a monotonicity constrain in their implementations. The Upwind scheme, which is first order, gives good approximation but produce higher numerical diffusion than UpwindE scheme.

The second objective was studied using two libraries: PETSc for distributed memory and CUSPARSE for GPUs where the memory is shared. We implemented a BiCGStab method with both libraries and we use similar operations in order to have equality of conditions. The saturation calculation step was implemented in terms of linear algebra operations, and we also measured the performance of this step. We obtained

that, for a fixed problem size the CUSPARSE implementation is approximately two times the speedup than the PETSc one. At this point we can say that our CUSPARSE implementation for a single GPU, is a better option than our PETSc implementation executed on a 12 CPU node. On the other hand, the PETSc implementation can be used for a bigger problems size, and in the case of our cluster, we can run in at least 8 nodes, allowing to investigate eight times bigger problems. This is important for more realistic research were we have very large-scale data sets.

Finally, we can say that a GPUs cluster will have better performance than a CPU only cluster. In some cluster architectures it is possible to deploy more than one GPU by node, allowing more floating point operations powerful. Combining the CPU and GPUs, along with efficient opensource libraries, like CUSPARSE and PETSc, we can face the challenge of oil reservoir simulation to a large-scale and more realistic formulations.

Acknowledgments

Luis M. de la Cruz wishes to acknowledge the support from the project IX10110 of DGAPA-UNAM to develop this research.

Appendix A

Coefficients of discrete pressure equation (10)

$$\mathbf{a}_e^n = \frac{k_{11} \lambda^n|_e A_x}{\Delta x_e} \equiv \mathbf{T}_e^n, \quad \mathbf{a}_w^n = \frac{k_{11} \lambda^n|_w A_x}{\Delta x_w} \equiv \mathbf{T}_w^n;$$

$$\mathbf{a}_n^n = \frac{k_{22} \lambda^n|_n A_y}{\Delta y_n} \equiv \mathbf{T}_n^n; \quad \mathbf{a}_s^n = \frac{k_{22} \lambda^n|_s A_y}{\Delta y_s} \equiv \mathbf{T}_s^n;$$

$$\mathbf{a}_f^n = \frac{k_{33} \lambda^n|_f A_z}{\Delta z_f} \equiv \mathbf{T}_f^n; \quad \mathbf{a}_b^n = \frac{k_{33} \lambda^n|_b A_z}{\Delta z_b} \equiv \mathbf{T}_b^n;$$

$$\mathbf{a}_p^n = \mathbf{a}_e^n + \mathbf{a}_w^n + \mathbf{a}_n^n + \mathbf{a}_s^n + \mathbf{a}_f^n + \mathbf{a}_b^n \equiv \mathbf{T}_p^n; \quad (13)$$

$$\begin{aligned} f_p^n &= \left(\sum_{nb} \mathbf{T}_{nb}^n \frac{dp_{cow}^n}{dS} \Big|_{nb} \right) S_p^n + \left(\varphi \sum_{nb} l_{nb}^n \right) \mathcal{D}_p - \\ &\left(\mathbf{T}_e^n \frac{dp_{cow}^n}{dS} \Big|_e S_e^n + \varphi l_e^n \mathcal{D}_e + \mathbf{T}_w^n \frac{dp_{cow}^n}{dS} \Big|_w S_w^n + \varphi l_w^n \mathcal{D}_w \right) - \\ &\left(\mathbf{T}_n^n \frac{dp_{cow}^n}{dS} \Big|_n S_n^n + \varphi l_n^n \mathcal{D}_n + \mathbf{T}_s^n \frac{dp_{cow}^n}{dS} \Big|_s S_s^n + \varphi l_s^n \mathcal{D}_s \right) - \\ &\left(\mathbf{T}_f^n \frac{dp_{cow}^n}{dS} \Big|_f S_f^n + \varphi l_f^n \mathcal{D}_f + \mathbf{T}_b^n \frac{dp_{cow}^n}{dS} \Big|_b S_b^n + \varphi l_b^n \mathcal{D}_b \right) + \\ &(\bar{Q}_w + \bar{Q}_o) \Big|_p \Delta V, \quad (\text{for } \mathbf{nb} \in \{e, w, n, s, f, b\}); \end{aligned} \quad (14)$$

$$\begin{aligned}
\mathbf{T}_e^n &= \frac{k_{11} \lambda_w^n |e| A_x}{\Delta x_e}; & \mathbf{T}_w^n &= \frac{k_{11} \lambda_w^n |w| A_x}{\Delta x_w}; & \mathbf{T}_n^n &= \frac{k_{22} \lambda_w^n |n| A_y}{\Delta y_n}; \\
\mathbf{T}_s^n &= \frac{k_{22} \lambda_w^n |s| A_y}{\Delta y_s}; & \mathbf{T}_f^n &= \frac{k_{33} \lambda_w^n |f| A_z}{\Delta z_f}; & \mathbf{T}_b^n &= \frac{k_{33} \lambda_w^n |b| A_z}{\Delta z_b}; \\
\mathbf{T}_{nb}^n &= \frac{(\lambda_w^n \rho_w + \lambda_0^n \rho_0) |nb|}{\Delta x_{nb}} \text{ for } nb \in \{e, w, n, s, f, b\};
\end{aligned} \tag{15}$$

Coefficients \mathbf{T}_{NB}^n and $\mathbf{T}_{NB'}^n$, for $NB = P, E, W, N, S, F, B$ and $nb = e, w, n, s, f, b$, are known as the transmissibilities of each control volume.

$$\begin{aligned}
\mathbf{b}_E^n &= \mathbf{T}_e^n \left. \frac{dp_{\text{cow}}^n}{dS} \right|_e \frac{\Delta t}{\phi \Delta V}; & \mathbf{b}_W^n &= \mathbf{T}_w^n \left. \frac{dp_{\text{cow}}^n}{dS} \right|_w \frac{\Delta t}{\phi \Delta V}; \\
\mathbf{b}_N^n &= \mathbf{T}_n^n \left. \frac{dp_{\text{cow}}^n}{dS} \right|_n \frac{\Delta t}{\phi \Delta V}; & \mathbf{b}_S^n &= \mathbf{T}_s^n \left. \frac{dp_{\text{cow}}^n}{dS} \right|_s \frac{\Delta t}{\phi \Delta V}; \\
\mathbf{b}_F^n &= \mathbf{T}_f^n \left. \frac{dp_{\text{cow}}^n}{dS} \right|_f \frac{\Delta t}{\phi \Delta V}; & \mathbf{b}_B^n &= \mathbf{T}_b^n \left. \frac{dp_{\text{cow}}^n}{dS} \right|_b \frac{\Delta t}{\phi \Delta V}; \\
\mathbf{b}_P^n &= \mathbf{b}_E^n + \mathbf{b}_W^n + \mathbf{b}_N^n + \mathbf{b}_S^n + \mathbf{b}_F^n + \mathbf{b}_B^n;
\end{aligned} \tag{16}$$

$$\begin{aligned}
\mathbf{c}_E^n &= \frac{k_{11} \lambda_w^n |e| A_x \Delta t}{\Delta x_e \phi \Delta V}; & \mathbf{c}_W^n &= \frac{k_{11} \lambda_w^n |w| A_x \Delta t}{\Delta x_w \phi \Delta V}; & \mathbf{c}_N^n &= \frac{k_{22} \lambda_w^n |n| A_y \Delta t}{\Delta y_n \phi \Delta V}; \\
\mathbf{c}_S^n &= \frac{k_{22} \lambda_w^n |s| A_y \Delta t}{\Delta y_s \phi \Delta V}; & \mathbf{c}_F^n &= \frac{k_{33} \lambda_w^n |f| A_z \Delta t}{\Delta z_f \phi \Delta V}; & \mathbf{c}_B^n &= \frac{k_{33} \lambda_w^n |b| A_z \Delta t}{\Delta z_b \phi \Delta V}; \\
\mathbf{c}_P^n &= \mathbf{c}_E^n + \mathbf{c}_W^n + \mathbf{c}_N^n + \mathbf{c}_S^n + \mathbf{c}_F^n + \mathbf{c}_B^n;
\end{aligned} \tag{17}$$

$$\begin{aligned}
\mathbf{d}_E^n &= \frac{k_{11} \lambda_w^n |e| \rho_w \wp}{\Delta x_e} \frac{\Delta t}{\phi \Delta V}; & \mathbf{d}_W^n &= \frac{k_{11} \lambda_w^n |w| \rho_w \wp}{\Delta x_w} \frac{\Delta t}{\phi \Delta V}; \\
\mathbf{d}_N^n &= \frac{k_{22} \lambda_w^n |n| \rho_w \wp}{\Delta x_n} \frac{\Delta t}{\phi \Delta V}; & \mathbf{d}_S^n &= \frac{k_{22} \lambda_w^n |s| \rho_w \wp}{\Delta x_s} \frac{\Delta t}{\phi \Delta V}; \\
\mathbf{d}_F^n &= \frac{k_{33} \lambda_w^n |f| \rho_w \wp}{\Delta x_f} \frac{\Delta t}{\phi \Delta V}; & \mathbf{d}_B^n &= \frac{k_{33} \lambda_w^n |b| \rho_w \wp}{\Delta x_b} \frac{\Delta t}{\phi \Delta V}; \\
\mathbf{d}_P^n &= \mathbf{d}_E^n + \mathbf{d}_W^n + \mathbf{d}_N^n + \mathbf{d}_S^n + \mathbf{d}_F^n + \mathbf{d}_B^n;
\end{aligned} \tag{18}$$

Appendix B

In this section, we show our implementations of BiCGStab [33]. This iterative Krylov-subspace method requires a matrix A and a left-side vector b , and returns an approximate vector solution x of the system $Ax = b$. The algorithm (2) presents the general steps of the BiCGStab method.

Algorithm 2 BiCGStab

- 1: $r_0 \leftarrow b - Ax_0$
- 2: r_0^* arbitrary
- 3: $p_0 \leftarrow r_0$
- 4: **for** $j = 0, 1 \dots j_{\max}$ **do**:
- 5: $\alpha_j \leftarrow (r_j, r_0^*) / (Ap_j, r_0^*)$
- 6: $s_j \leftarrow r_j - \alpha_j Ap_j$
- 7: $w_j \leftarrow (As_j, s_j) / (As_j, As_j)$
- 8: $x_{j+1} \leftarrow x_j + \alpha_j p_j + w_j s_j$
- 9: $r_{j+1} \leftarrow s_j - w_j As_j$
- 10: $\beta_j \leftarrow (r_{j+1}, r_0^*) / (r_j, r_0^*) \times \alpha_j / w_j$
- 11: $p_{j+1} \leftarrow r_{j+1} + \beta_j (p_j + w_j Ap_j)$
- 12: **end for**

The corresponding CUDA implementation used in this work is presented below.

```

init_res = cublasDnrm2(N,d_r,1);
if(init_res!=0.0) init_res=1./init_res;
else return false;

cusparseDcsrmmv(handle,CUSPARSE_OPERATION_
NON_TRANSPOSE, N, N,-1.,
descr, d_val, d_row, d_col, d_x, 1., d_r);
res = cublasDnrm2(N,d_r,1);
res *= init_res;
if (res < tol) return true;

cublasDcopy(N,d_r,1,d_rtilde,1);

while ( res > tol && k <= max_iter) {
    ri_0 = cublasDdot(N,d_rtilde,1, d_r,1);
    if (ri_0 == PrecType(0)) {
        return false;
    }

    if (k!=1){
        if (omega == 0.) {
            return false;
        }

        beta = (ri_0 / r_ant) * (alpha / omega);
        cublasDaxpy(N,-omega,d_Ap,1,d_p,1);
        cublasDscal(N,beta,d_p,1);
        cublasDaxpy(N,PrecType(1),d_r,1,d_p,1);
    } else {
        cublasDcopy(N,d_r,1, d_p,1);
    }

    cusparseDcsrmmv(handle,CUSPARSE_OPERATION_
NON_TRANSPOSE, N, N, 1.,

```


- Balay S., Brown J., Buschelman K., Gropp W.D., Kaushik D., Knepley M.G., Curfman McInnes L., Smith B.F., Zhang H., 2012, PETSc Users Manual, ANL-95/11 - Revision 3.3, Argonne National Laboratory.
- Barrett R., Berry M., Chan T.F., Demmel J., Donato J., Dongarra J., Eijkhout V., Pozo R., Romine C., Van der Vorst H., 1994, Templates for the Solution of Linear Systems: Building Blocks for Iterative Methods, 2nd Edition, SIAM, Philadelphia, PA.
- Beisembetov I.K., Bekibaev T.T., Assilbekov B.K., Zhabbasbayev U.K., Kenzhaliev B.K., 2012, Application of GPU in the development of 3D hydrodynamics simulators for oil recovery prediction, *AGH Drilling Oil Gas*, 29, 1.
- Boris N. Chetverushkin B., Churbanova N.G., Morozov D.N., Trapeznikova M.A., 2010, Kinetic approach to simulation of multiphase porous media flow, V European Conference on Computational Fluid Dynamics ECCOMAS CFD 2010, J. C. F. Pereira and A. Sequeira (Eds), Lisbon, Portugal, 14-17.
- Buckley S., Leverett M., 1942, Mechanism of fluid displacement in sands. *Trans. AIME*, 146, 107-116.
- Bydal A., 2009, GPU-accelerated simulation of flow through a porous medium (Master degree thesis). Faculty of Engineering and Science, University of Agder, Grimstad May 25. http://brage.bibsys.no/hia/bitstream/URN:NBN:no-bibsys_brage_10942/1/Bydal.pdf.
- CUDA Toolkit 4.2, CUSPARSE Library NVIDIA Corporation, 2012, 2701 San Tomas Expressway, Santa Clara, CA 95050.
- Chen Z., Huan G., Ma Y., 2006, Computational Methods for Multiphase Flows in Poros Media, SIAM.
- Chen Z., 2007, Reservoir Simulation Mathematical Techniques in Oil Recovery, SIAM, Philadelphia, USA.
- Coplien J.O., 1995, Curiously recurring template patterns. C++ Report, 24-27.
- Corey A., 1954, The interrelation between gas and oil relative permeabilities. *Prod. Montly*, 19, 1, 3841.
- Datta-Gupta A., King M.J., 2007. Streamline Simulation: Theory and Practice, Society of Petroleum Engineers Textbook Series Vol. 11.
- De la Cruz L.M., Template units for numerical applications and modelling (TUNAM) Web page, <http://code.google.com/p/tunam/>.
- De la Cruz L.M., Ramos E., 2012, General Template Units for the Finite Volume Method in Box-shaped Domains. Accepted to be published in *Trans. Math. Soft.*
- Herrera I., Pinder G.F., 2012, Mathematical Modeling in Science and Engineering: An Axiomatic Approach, John Wiley.
- Herrera I., Herrera G., 2010, Unified Formulation of Enhanced Oil-Recovery Methods, *Geofisica Internacional*, 2010.
- Kirk D.B., Hwu W., 2010, Programming Massively Parallel Processors: A Hands-on Approach (Applications of GPU Computing Series). Elsevier, Massachusetts.
- Leonard B.P., 1979, A stable and accurate conevctive modelling procedure based on quadratic upstream interpolation. *Comp. Meth. in App. Mech. and Engineering*, 19:59-98.
- Leveque R.J., 2004, Finite Volume Methods for Hyperbolic Problems. Cambridge University Press.
- Openmp: Simple, portable, scalable smp programming. <http://www.openmp.org/>.
- Patankar S.V., 1980, Numerical Heat Transfer and Fluid Flow. McGraw-Hill.
- Pereira F., Rahunanthan A., 2010, Numerical Simulation of Two-phase Flows on a GPU Proceedings of 9th International Meeting, High Performance Computing for Computational Science (VECPAR 2010), Berkeley, CA.
- Saad Y., 2000, Iterative Methods for Sparse Linear Systems. PWS/ITP 1996. Online: <http://www-users.cs.umn.edu/~saad/books.html>.
- Snir M., Otto S., Huss-Lederman S., Walker D., Dongarra J., 1998, MPI: The Complete Reference: Volume 1, The MPI Core. The MIT Press, Cambridge, Massachusetts, London, second edition edition.
- The NVIDIA CUDA Sparse Matrix library (cuSPARSE) Web page, 2012, <http://developer.nvidia.com/cuda/cusparse>.

- Tolke J., Krafczyk M., 2008, TeraFLOP computing on a desktop PC with GPUs for 3D CFD. *International Journal of Computational Fluid Dynamics*, 22, 7, 443-456.
- Tomova S., Dongarra J., Baboulina M., 2010, Towards dense linear algebra for hybrid GPU accelerated many core systems. *Parallel Computing*, 36, 56, Pages 232-240.
- Torp A., 2009, *Sparse linear algebra on a GPU with Applications to flow in porous Media* (Master degree thesis). Norwegian University of Science and Technology, Department of Mathematical Sciences. <http://ntnu.diva-portal.org/smash/record.jsf?pid=diva2:347855>
- Trapeznikova M., Chetverushkin B., Churbanova N., Morozov D., 2012, Two-Phase Porous Media Flow Simulation on a Hybrid Cluster, I. Lirkov, S. Margenov, and J. Wasniewski (Eds.): *LSSC 2011, LNCS 7116*, pp. 646-653. Springer-Verlag Berlin Heidelberg.
- Versteeg H., Malalasekera W., 1995, An introduction to computational fluid dynamics: The finite volume method. Longman.
- Walsh S.D.C., Saar M.O., Bailey P., Lilja D.J., 2009, Accelerating geoscience and engineering system simulations on graphics hardware. *Computers & Geosciences*, 35, 2353-2364.
- Zaspel P., Griebel M., 2012, Solving incompressible two-phase flows on multi-GPU clusters. *Computers & Fluids journal*, In press.

Reducing wind noise in seismic data using Non-negative Matrix Factorization: an application to Villarrica volcano, Chile

Giuseppe Cabras*, Roberto Carniel, Joshua P. Jones and Minoru Takeo

Received: January 17, 2013; accepted: April 05, 2013; published on line: December 11, 2013

Resumen

La separación de distintas fuentes existentes en una sola señal sísmica es un problema interesante y al mismo tiempo difícil. En este trabajo presentamos un método semi-ciego para la separación de un solo canal sísmico para mejorar la parte de señal de origen volcánico. En este método, el esquema de descomposición de las fuentes se basa en una factorización en matrices dispersas y non-negativas (Non-negative Matrix Factorization, NMF) de la representación tiempo-frecuencia del único canal sísmico vertical. Como caso de estudio se presenta una aplicación a partir de datos sísmicos registrados en el volcán Villarrica, Chile, uno de los más activos de los Andes meridionales. Los datos analizados están fuertemente contaminados por el ruido del viento y el procedimiento propuesto se utiliza para separar un componente de origen volcánico de otro de origen meteorológico.

Palabras clave: Tremor volcánico, NMF, Villarrica, reducción del ruido del viento.

Abstract

Single channel source separation of seismic signals is an appealing but difficult problem. In this paper, we introduce a semi-blind single-channel seismic source separation method to enhance the components of volcanic origin. In this method, the source decomposition scheme is addressed as a Sparse Non-negative Matrix Factorization (NMF) of the time-frequency representation of the single vertical seismic channel. As a case study we present an application using seismic data recorded at Villarrica volcano, Chile, one of the most active in the southern Andes. The analysed dataset is strongly contaminated by wind noise and the procedure is used to separate a component of volcanic origin from another of meteorological origin.

Key words: volcanic tremor, NMF, Villarrica, wind noise reduction.

G. Cabras*
Dipartimento di Chimica, Fisica e Ambiente
Università degli Studi di Udine
Via delle Scienze, 206
Udine, Italy
*Corresponding authors: giuseppe.cabras@uniud.it

R. Carniel
Laboratorio di misure e trattamento dei segnali
Dipartimento di Ingegneria Civile e Architettura
Università degli Studi di Udine
Via delle Scienze, 206
Udine, Italy

Earthquake Research Institute
University of Tokyo
Tokyo, Japan
E-mail: roberto.carniel@uniud.it

Geognosis Proj., Int. Syst. Lab.
National Research University
of Information Technologies
Mechanics and Optics
Kronverksky Prospect, 49
St. Petersburg 197101, Russia

J.P. Jones
Department of Physics - CCIS
University of Alberta,
Edmonton AB T6G 2E1
Canada
E-mail: jppjones@ualberta.ca

M. Takeo
Earthquake Research Institute
University of Tokyo
Tokyo, Japan
E-mail: takeo@eri.u-tokyo.ac.jp

Introduction

Villarrica volcano (Chile), located in the southern Andes (39.42° S, 71.93° W) has more than 60 important historical eruptions (Casertano, 1963). As other volcanoes of basic composition (Behncke *et al.*, 2003; Behncke, 2009), Villarrica can not only produce effusive and moderate explosivity activity, but also pyroclastic flows that represent the most dangerous scenario (Moreno, 1998). It is currently characterized by the presence of a small (30-40 m wide) summit lava lake which produces a persistent volcanic tremor and discrete events associated to strombolian activity (Ortiz *et al.*, 2003; Tárrega *et al.*, 2008). In November 2004 we installed an L22 three-component geophone ($f_0 = 2.0$ Hz) approximately 800 m from the summit crater. The seismometer recorded continuously for a period of 10 days, between November 8, 2004 and November 17, 2004.

Noise often affects records of volcanic tremor or ambient ground-motion recordings used e.g. for HVSR estimates of seismic site amplification. Benson *et al.* (2007) introduce several methods to reduce the effects of local, non-stationary noise sources, earthquakes and instrumental irregularities on ambient noise. Lambert *et al.* (2011) propose four methodologies focused on the removal of the effects of anthropogenic noise. In this work, we apply an innovative wind noise reduction procedure to the tremor recorded at Villarrica, based on Non-negative Matrix Factorization with Sparse Coding (Hoyer, 2002) and on the construction of a wind noise dictionary which is estimated from the available seismic recording itself. The presented procedure can be extended to the filtering of wind noise in other volcanic geophysical time series, such as the ones recorded by infrasonic sensors (Ichihara *et al.*, 2012).

A two training step strategy to Single-Sensor Seismic Analysis

In this paper, we extend the Non-negative Matrix Factorization (NMF) and Sparse Coding (SC) procedure introduced in (Cabras *et al.*, 2012), where the basic idea is that we can obtain a meaningful part-based factor decomposition (Lee & Seung, 1999) from a single-channel time series imposing only the constraints of non-negativity and sparseness of the data. For a general discussion on NMF and SC, see Cichocki *et al.* (2009). As we will describe in detail below, the main contribution with respect to the original procedure (Cabras *et al.*, 2012) lies in the training stage, where we learn two sets of basis components in two steps directly from the available dataset: in the first training step we learn an approximate volcanic-set basis components (or preliminary volcanic-set dictionary), \tilde{D}'_s , selecting a non windy data-set

for training; in the second training step we learn the wind-set basis components (or noise-set dictionary), D'_n , selecting a windy data-set for training. The separation stage remains the same of (Cabras *et al.*, 2012), providing a fixed wind-set basis components, D'_n to the constrained sparse NMF learning loop.

We can state an NMF problem as follows: given a non-negative data matrix $\mathbf{X} \in \mathbb{R}_+^{F \times T}$ (with $x_{ft} \geq 0$ or equivalently $X \geq \theta$) and a reduced rank K ($K \leq \min(F, T)$), find two non-negative matrices $\mathbf{D} \in \mathbb{R}_+^{F \times K}$, called dictionary or basis components and $\mathbf{H} \in \mathbb{R}_+^{K \times T}$, called sparse code or weights, which factorize X as well as possible, that is:

$$X = DH + E, \quad (1)$$

where $E \in \mathbb{R}_+^{F \times T}$ represents the approximation error to minimize. The meaning of dictionary matrix D , sparse code matrix H and rank K depends on the specific application and signal representation. To estimate the parameters of NMF, (i.e. the factor matrices D and H), we need to minimize the measure of similarity (or cost function C) between the data matrix X and the estimated model matrix $\hat{X} = DH$; the simplest and widely used measure is the squared Euclidean distance (or Frobenius norm):

$$\operatorname{argmin}_{D, H} C_F(X \| DH) = \frac{1}{2} \| XDH \|_F^2 + \lambda \| H \|_1 \quad (2)$$

where λ is a non-negative regularization parameter that controls the tradeoff between sparseness and reconstruction error and $\| H \|_1$ is an ℓ_1 norm regularization function proposed in Hoyer (2002).

Cabras *et al.* (2012) adopted the single channel enhancement model originally developed for processing audio records (Cabras *et al.*, 2010) to separate a "high convective", relatively transient, seismic source of interest from a "low convective", relatively continuous, "noise" in a single-sensor seismic time series recorded at Erta 'Ale volcano (Harris *et al.*, 2005). Erta 'Ale is characterized by the presence of a permanent lava lake that produces, in a similar way to Villarrica, at least part of a continuous volcanic tremor (Jones *et al.*, 2006), which is really characterized by a superposition of different independent sources (Jones *et al.*, 2012). In the Erta 'Ale case study, we learned the basis components of the noise $n(t)$, denoted by D'_n , in a single step training stage, because in our data-set we have segments of pure "low convective noise" for training.

In the present case study of Villarrica volcano, this strategy is not directly applicable. In fact, our data-set is characterized by a relatively continuous "volcanic tremor", our source of interest, immersed in a relatively transient "wind" noise that we want to suppress. Wind components change rapidly in

time and wind gusts can show very high energy, with comparable or greater energy than the volcanic tremor background, which is always present. This implies that we have no samples of pure “wind” noise for training. Both tremor and wind are non-stationary broad-band sources, with overlapping components in time and frequency as in the daily data-set shown in Figure 1. Focusing our attention to power spectral density of a windy day and a few hours of tremor signal registration without wind present, we recognize that most of the energy overlaps in the low frequency range, while high frequency range is dominated by wind components, as depicted in Figure 2. Our final task is to reduce wind noise in single-channel volcanic seismic recordings by means of a classical refiltering technique as suppression rule, such as a Wiener one (see Figure 3).

As in the Erta 'Ale case (Cabras *et al.*, 2012), we aim to estimate the undesired components, or interference, $n(t)$ and the source of interest, or target, $s(t)$ directly from the observable data mix in

the time domain, with minimal *a priori* knowledge. A common technique to manipulate a time-varying observed signal consists in transforming it into a time-frequency representation. Assuming that saturation effects are absent in the mixed observable $x(t)$:

$$x(t) = s(t) + n(t), \quad (3)$$

and assuming that $s(t)$ and $n(t)$ are uncorrelated, we can extend linearity in the power spectral domain and transform the data into a non-negative representation suitable for NMF scheme:

$$|X(f, t)|^2 = |X_s(f, t)|^2 + |X_n(f, t)|^2, \quad (4)$$

where the observable signal $x(t)$ and the sources $s(t)$ and $n(t)$ are transformed into a complex time-frequency representation $X(f, t)$, $X_s(f, t)$ and $X_n(f, t)$ respectively. The most commonly used time-frequency representation is the Short-Time Fourier Transform (STFT) which transforms a discrete time signal into a complex spectrogram.

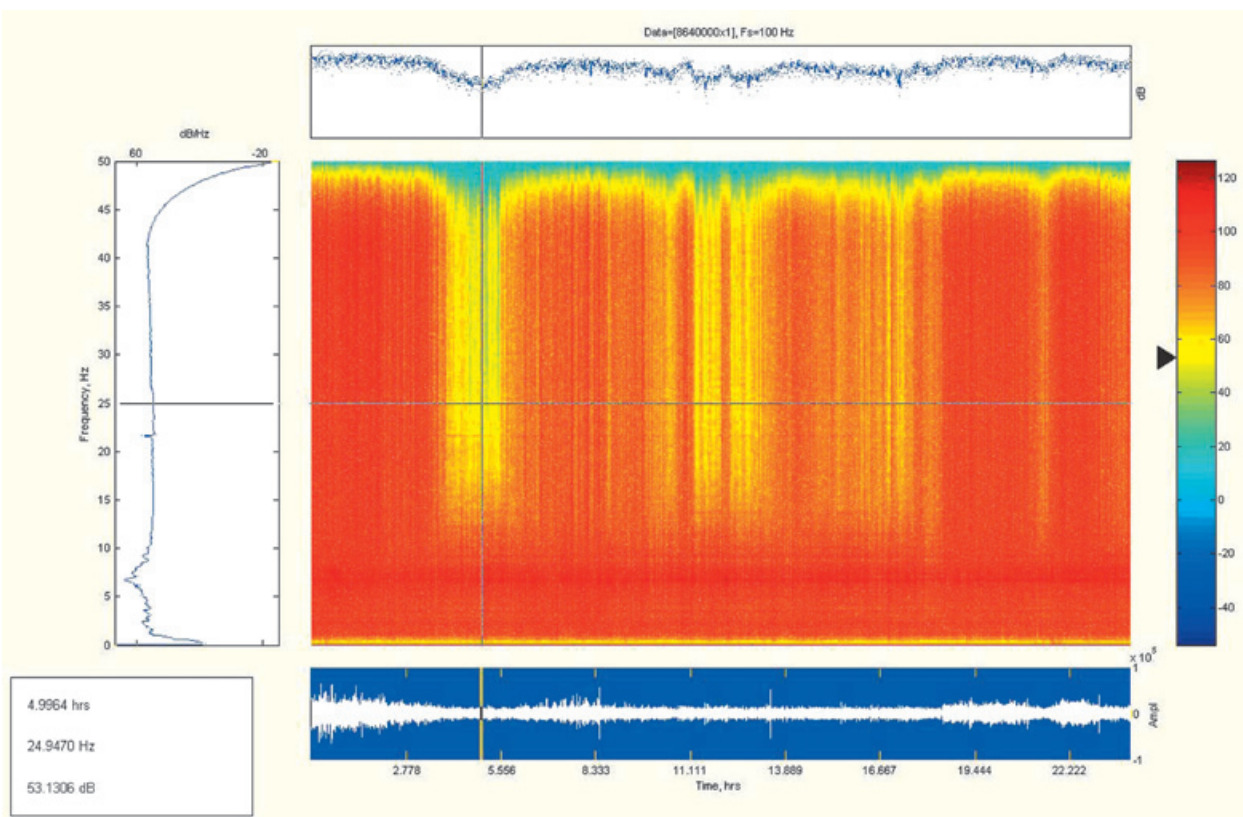


Figure 1. Spectral analysis of one day data-set, in the center-bottom panel, a full day time-series registration showing largest amplitudes in presence of wind noise; in the center-medium panel, the spectrogram showing a highly non-stationary broad-band wind noise and relatively continuous broad-band tremor with a peak at approximately 7 Hz; in the left-center panel, the power spectral density (psd) shows the average broad-band spectrum of the signal with a peak of energy centered again at about 7 Hz; in the center-top panel, marginal time-slice energy distribution at a given frequency (e.g. 25 Hz) is shown, pointing out the non-stationary character of the recorded signal at a given frequency.

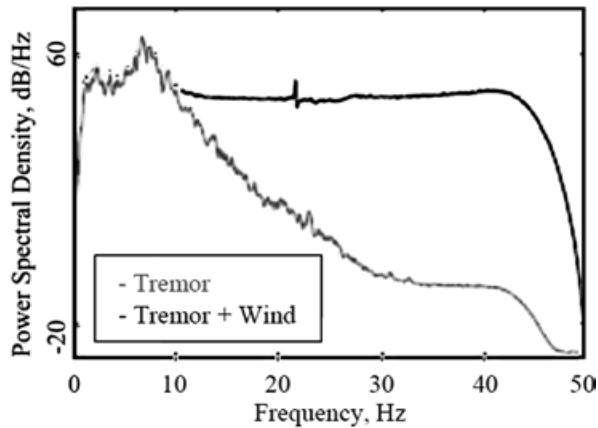


Figure 2. Power Spectral Density of the windy day dataset of Figure 1 (blue line) and a few hours of volcanic tremor without wind of another day data-set available (red line). Both records are broad-band signals with a peak of energy centered at about 7 Hz, attributable to tremor. Windy record is characterized by a constant high energy broad-band noise. At $f > 10$ Hz, tremor energy decays rapidly and wind noise dominates, masking anything volcanic in this frequency range.

In the following a more general element-wise exponentiated STFT was adopted:

$$|X(f, t)|^2 = |STFT\{x(t)\}|^{2\beta}, \quad (5)$$

where β is an important parameter to NMF performance, not only in audio application as shown in Schmidt *et al.* (2007), but also on seismic time-frequency signal representation.

In a time-frequency representation, the k columns of the dictionary matrix D in Eq. 1 constitute the characteristic frequency components of the spectrogram amplitude, while the k rows of the sparse code matrix H contains the weights of corresponding components of the dictionary matrix used in each time frame of the spectrogram amplitude.

Assuming the additivity of sources, the dictionary of the mixed signal of Eq. 1 can be seen as the horizontal concatenation of the individual source dictionaries. Moreover, the sparse code of the mixed signal can be seen as the vertical concatenation of the individual source sparse codes:

$$X = X_s + X_n = [D_s D_n] \begin{bmatrix} H_s \\ H_n \end{bmatrix} + E = DH + E, \quad (6)$$

where all matrices are non-negative.

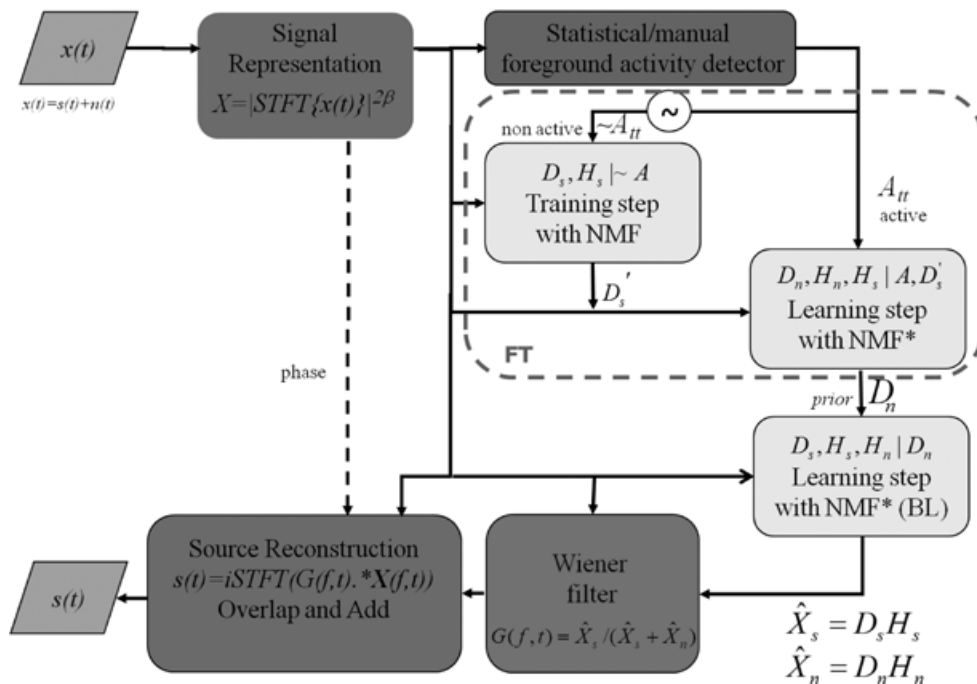


Figure 3. General scheme of the target enhancement model FT/BT. Preliminary precompute background target dictionary (D'_s) when non-overlapped to foreground noise, learn foreground noise dictionary (D_n) from mixed recording, learn background target dictionary (D_s) from mixed recording (**Foreground Training** and Background Learning, **FT/BL**).

In order to estimate the magnitude of true sources X_s and X_n , we use a constrained sparse NMF (NMF*) to compute the dictionary of the target source D_s and the sparse code of both sources H_s and H_n assuming the dictionary D_n known *a priori* (Cabras *et al.*, 2010). Finally we estimate the spectrogram of tremor source as:

$$\hat{X}_s = D_s H_s, \quad (7)$$

and the spectrogram of the wind noise as:

$$\hat{X}_n = D_n H_n, \quad (8)$$

Three strategies can be adopted to learn dictionaries D_s and D_n depending on available mixed and unmixed training data, characterizing the following enhancement models:

a) Precompute all dictionaries (D_s and D_n or in general D_1, D_2, \dots, D_N) in non-overlapping time-series (Sources Training, ST enhancement model);

b) Precompute background noise dictionary (D_n) when non-overlapped to target and learn target dictionary (D_s) from mixed recording (Background Training and Foreground Learning, BT/FL enhancement model);

Preliminary precompute background target dictionary (D'_s) when non-overlapped to foreground noise, learn foreground noise dictionary (D_n) from mixed recording, learn background target dictionary (D_s) from mixed recording (Foreground Training and Background Learning, FT/BL enhancement model).

A limitation of the Sources Training enhancement model strategy is that each source dictionary D_1, D_2, \dots, D_N must be modeled prior to the separation. This approach was followed by Mehmood *et al.* (2012) in a seismic footstep detection based system to separate the human footstep signatures from the horse footstep spectral signatures. However, the availability of non-overlapping time series for all the different sources rarely applies to natural seismic datasets. Background Training and Foreground Learning is a more realistic strategy when background noise is more stationary than the foreground signal of interest and we can easily recognize enough samples of background noise-only to learn D_n . Schmidt *et al.*, (2007) suggest to pre-compute D_n , an approach followed also by (Cabras *et al.*, 2012), then learn $D_s(f, m)$, $H_s(m, t)$ and $H_n(k, t)$ with a modified constrained NMF, where m is the number of user defined components of the target source dictionary and k is the number of user defined components of the noise dictionary.

But if we are interested in a Background Source more stationary than the Foreground Noise, it

will be probably very difficult to find samples of noise-only components to carry out the training. An alternative approach has then to be followed, where a first training step on background source-only samples is followed by a learning step of noise components which determines the new 2 steps foreground noise training (FT in Figure 3) while in Cabras *et al.* (2012) background noise was trained in one single step, because of noise-only samples availability. The estimation of *a priori* noise dictionary, D_n , is modeled by a two step sparse NMF computation, where equations are similar to the equations described in Cabras *et al.* (2012) but switching the index definitions of "noise" (n) and "source" (s) and shortly reformulated here for clarity. In the first step the sparse NMF algorithm starts with randomly initialized matrix, D'_s and H'_s , and alternates the following updates until convergence:

$$\begin{aligned} H'_s &\leftarrow H_s \odot \frac{\tilde{D}'_s{}^T X \bar{A}}{\tilde{D}'_s{}^T \tilde{D}'_s H'_s + \lambda_s}, \quad (9) \\ D'_s &\leftarrow \tilde{D}'_s \odot \frac{X \bar{A} H'_s{}^T + \tilde{D}'_s \odot (1(\tilde{D}'_s H'_s H'_s{}^T \odot \tilde{D}'_s))}{\tilde{D}'_s H'_s H'_s{}^T + \tilde{D}'_s \odot (1(X \bar{A} H'_s{}^T \odot \tilde{D}'_s))}, \quad (10) \end{aligned}$$

where \odot operator indicates element-wise multiplication, the fraction line element-wise division between two matrices, \tilde{D}'_s is the Euclidean column-wise normalization of the dictionary to prevent joint numerical drifts D'_s in H'_s and (Eggert and Körner, 2004), $\mathbf{1}$ is a suitable size square matrix of ones and A is the activity diagonal binary square matrix, explained in more detail in the discussion section. The parameter λ_s determines the degree of sparsity in the code matrix. The trained preliminary dictionary of target source D'_s is the *a priori* knowledge to learn the noise dictionary D_n , which can be trained directly from selected time sections of the available noisy signal using a constrained sparse NMF (NMF*) model estimation, so that only D_n , H_n and H'_s are estimated, while D'_s is predefined and left unchanged by the following updating equations until convergence:

$$H_n \leftarrow H_n \odot \frac{\tilde{D}'_n{}^T X A}{\tilde{D}'_n{}^T (\tilde{D}'_s H'_s + \tilde{D}'_n H_n) + \ell_n}, \quad (11)$$

$$H'_s \leftarrow H'_s \odot \frac{\tilde{D}'_n{}^T X A}{\tilde{D}'_n{}^T (\tilde{D}'_s H'_s + \tilde{D}'_n H_n)}, \quad (12)$$

$$D_n \leftarrow D_n \odot \frac{X A H'_n{}^T + \tilde{D}_n \odot (1((\tilde{D}'_s H'_s + \tilde{D}'_n H_n) H'_n{}^T \odot \tilde{D}_n))}{(\tilde{D}'_s H'_s + \tilde{D}'_n H_n) H'_n{}^T + \tilde{D}_n \odot (1(X A H'_n{}^T \odot \tilde{D}_n))}, \quad (13)$$

The resulting noise dictionary, D_n , is the *a priori* estimated information needed by the final Background Learning step (BL) as shown in Figure 3. BL is the final Blind Source Separation step (BSS) which assigns the decomposed parts to the source of interest and discards the interference source described in Cabras *et al.* (2012) with a solution based on a constrained sparse Non-negative Matrix Factorization (NMF) model estimation and *prior* knowledge on undesired component.

A case study: Villarrica wind noise reduction

For illustrative purposes, we applied our methodology to a seismic dataset recorded at Villarrica volcano.

Datasets

The analyzed dataset consists of 10 full day records of a single L22 short period vertical sensor component ($f_0=2.0$ Hz) sampled at 100 Hz. Each record exhibits non stationary high frequency non volcanic signal contamination, presumably determined by strong wind. No additional *a priori* information, such as a wind gauge, is available. Figure 1 shows an example of a full day record spectral analysis. The Power Spectrum Density (PSD) of Figure 2 shows that the wind energy recorded from the vertical sensor component dominate in frequency > 10 Hz, while overlaps with tremor energy in the low frequency range.

Parameters

In order to process the dataset with the NMF algorithm, volcanic recordings are analyzed by an 8192 point Hamming windowed with $\beta = 1/3$ exponentiated STFT and 50% overlap (Eq. 4). This heuristic value of β , which corresponds to the cube root compression, is quite important to achieve good NMF data decomposition in terms of SNR, our experimental results confirm that the more common value $\beta = 1$ produces worse separation results.

The number of components in the target source dictionary, m , and the number of components in the noise source, k , are very important parameters which depend highly to the true but unknown sources, since all these components concur to model the sources. Using too few components results in a poor model of the sources which show strong evidence only for a limited set of data; conversely, more complex models (i.e. with many components) can always fit the data, but we must avoid implausible over-parameterized models, following the principle of parsimony, i.e. finding the model that most simply accounts for the observed dataset. With our seismic datasets, we get plausible dictionaries with k and m in the range of 32-64 components.

The sparsity regularization parameter enforces sparseness (i.e. simplicity) to learn the preliminary volcanic dictionary and controls the tradeoff between sparseness and reconstruction error. Increasing the sparseness term, the dictionary solution becomes less fragmented, since the decomposition algorithm tends to encode the input matrix using less dictionary components. Good solutions are achieved with $\lambda_s = 0.5$.

In a similar way, sparseness regularization parameter enforces sparseness to learn the wind noise dictionary D_n , in our experimental datasets; good results were obtained for $\lambda_s = 0.5$.

Results and discussion

In order to estimate the preliminary target dictionary D_s , we analyze several 1 day records (8.64 Msamples@100Hz sampling frequency) to catch some temporal frames without wind, as at 5 hrs of Figure 1, where Power Spectral Density is similar to the red line of Figure 2. It is evident that a major requirement for the method to work properly is the availability and the recognition by the user of a time period for which there is only "source" signal, i.e. without wind contamination. This training period should be chosen by careful examination of the spectral content time evolution and/or, if available, using additional data such as datasets from pressure sensors, microphones, infrasound sensors or anemometers. Visual spectrogram screening can be a subjective and an error prone selection activity which must be taken in account and reduced adopting a statistical estimation algorithm, in figure 3 we call it Statistical Foreground Activity Detector, which detect and flag the active frames (if frame t is active: $A_t = 1$, otherwise 0), implemented as a time-recursive averaging algorithm based on signal-presence uncertainty, similar to statistical Voice Activity Detector (VAD) used in speech enhancement methods (Cabras *et al.*, 2010). With the selected temporal frames we apply a sparse NMF to preliminary train the tremor dictionary shown in bottom left panel of Figure 4. This pre-estimated source model is then used to estimate the wind noise dictionary applying a sparse NMF* learning algorithm on a strong windy day data-set; the resulting D_n is depicted in the top right panel of Figure 4. This is a definitive wind noise dictionary for our data-set and is very important to prevent volcanic tremor components amongs D_n components. The further learning step (BL in Figure 3) was applied to all records of the data-set to estimate D_s , H_s and H_n and estimate the tremor source spectrogram (Eq. 7) and the noise source spectrogram (Eq. 8). Figure 5 shows the estimated spectrogram sources of a full day recording. The dataset tremor dictionary D_s is shown in the right bottom of Figure 4. It is similar to but smoother, depending on more data frames, and it differs greatly from D_n , although it points out some frequency superposition.

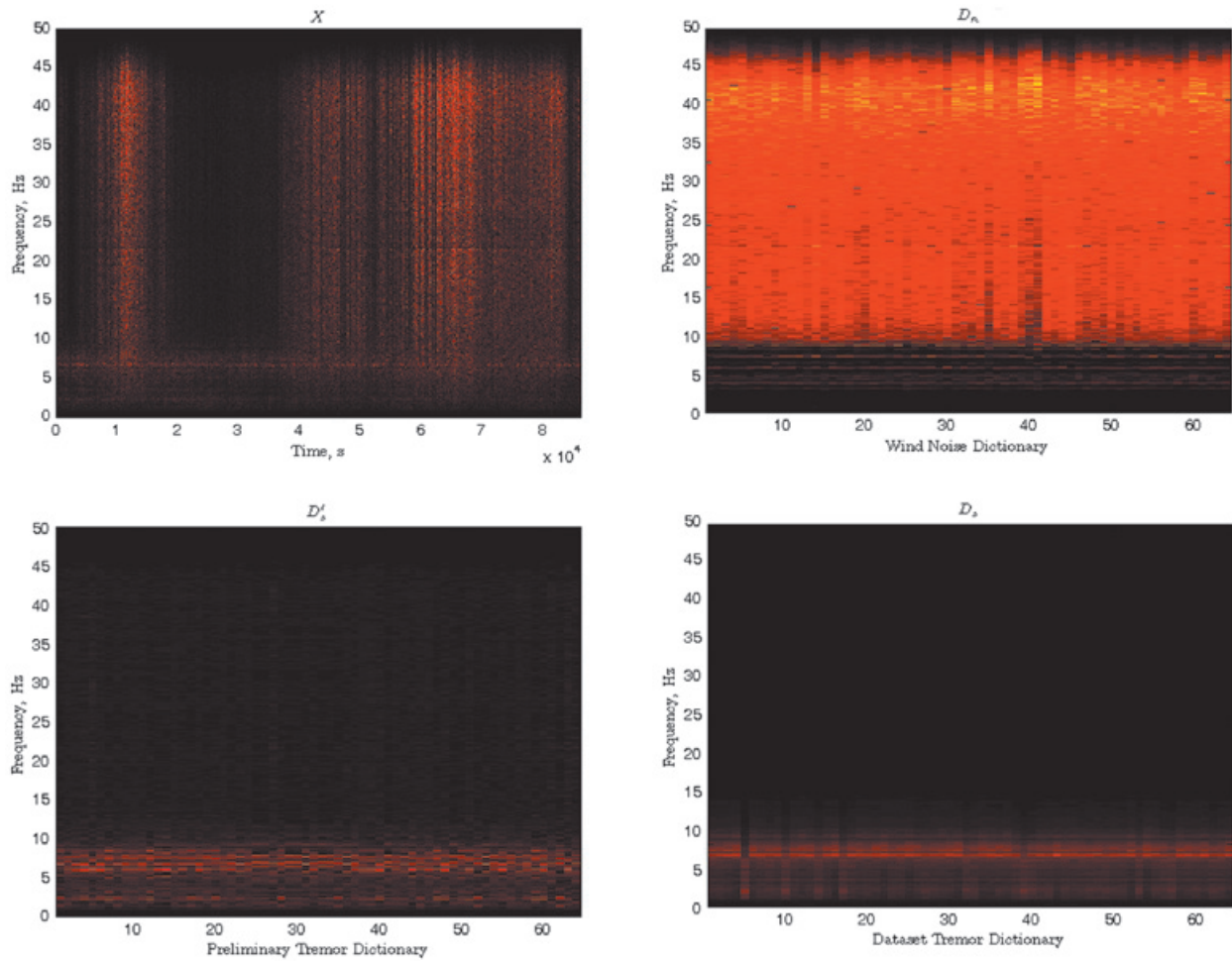


Figure 4. Observed signal spectrogram X (top left panel), characterized by 2 windy temporal windows; preliminary tremor dictionary D'_s estimated in a short, wind free, temporal window (bottom left); wind noise dictionary D_w estimated in the second windy temporal window (top right); dataset tremor dictionary D_s estimated in the full day.

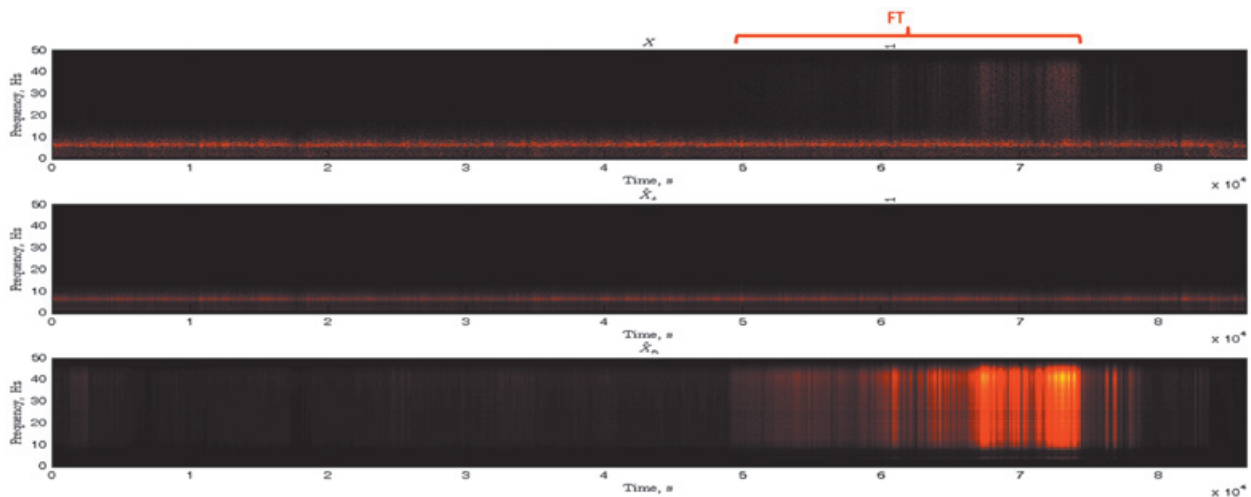


Figure 5. Spectrograms of a wind corrupted signal X (top panel), estimated tremor source \hat{X}_s (center panel) and estimated wind noise \hat{X}_w (bottom panel) of a 24 hours of Villarrica vertical sensor component. Foreground Training (FT) was applied in the temporal window between 5×10^4 s and 7.5×10^4 s.

Conclusions

We have presented an automatic method for wind noise reduction of volcanic tremor based on estimating the noise components dictionary by means of sparse NMF algorithms. The novel idea is to pre-compute a preliminary dictionary model only for the target source and infer the dictionary model of the noise from a suitable representation of a signal mixture. Notwithstanding the obvious drawback that the user must be able to highlight a time period where source signal is not affected by wind (if possible with the help of additional wind-affected sensors), experiments on a real world seismic-only dataset recorded at Villarrica volcano contaminated by strong wind noise show that sparse NMF algorithms and our method are quite effective to reduce wind noise in single channel seismic recordings and can be successfully used to better investigate the time evolution of tremor spectral content.

Acknowledgments

We are grateful to Dr. Jeff Witter for assistance with location and deinstallation of the seismometer site.

Bibliography

Behncke B., Neri M., Carniel R., 2003, An exceptional case of endogenous lava dome growth spawning pyroclastic avalanches: The 1999 Bocca Nuova eruption of Mt. Etna (Italy). *Journal of Volcanology and Geothermal Research*, 124, 1-2, 115-128.

Behncke B., 2009, Hazards from pyroclastic density currents at Mt. Etna (Italy). *Journal of Volcanology and Geothermal Research*, 180, 2-4, 148-160.

Benson G.D., Ritzwoller M.H., Barmin M.P., Levshin A.L., Lin F., Moschetti M.P., Shapiro N.M., Yang Y., 2007, Processing seismic ambient noise data to obtain reliable broadband surface wave dispersion measurements. *Geophys. J. Int.*, 169, 1239-1260.

Cabras G., Canazza S., Montessoro P.L., Rinaldo R., 2010, The restoration of single channel audio recordings based on non-negative matrix factorization and perceptual suppression rule. In H. Pomberger, F. Zotter, A. S., editor, Proc. of the 13th Int. Conference on Digital Audio Effects - DAFX-10, pages 458-465, Graz, Austria.

Cabras G., Carniel R., Jones J., 2012, Non-negative Matrix Factorization: an application to Erta 'Ale volcano, Ethiopia, *Bollettino di Geofisica Teorica ed Applicata*, 53, 2, 231-242.

Casertano L., 1963, General characteristics of active Andean volcanoes and summary of their activities during recent centuries. *Bull. Seism. Soc. Am.*, 53, 1415-33.

Cichocki A., Zdunek R., Phan T., Amari S., 2009, Nonnegative Matrix and Tensor Factorizations: Applications to Exploratory Multy-way Data Analysis and Blind Source Separation. Wiley, Tokyo, 500pp. Eggert, J. and Körner, E., 2004. Sparse coding and NMF. In IEEE International Conference on Neural Networks, pages 2529-2533. IEEE.

Harris A.J.L., Carniel R., Jones J., 2005, Identification of variable convective regimes at Erta Ale Lava Lake. *J. Volcanol. Geotherm. Res.*, 142, 207- 223.

Hoyer P.O., 2002, Non-negative sparse coding. In Neural Networks for Signal Processing, IEEE Workshop on, pages 557-565.

Ichihara M., Takeo M., Yokoo A., Oikawa J., Ohminato T., 2012, Monitoring volcanic activity using correlation patterns between infrasound and ground motion, *Geoph. Res. Lett.*, 39, L04304.

Jones J., Carniel R., Harris A.J.L., Malone S., 2006, Seismic characteristics of variable convection at Erta 'Ale lava lake, Ethiopia. *Journal of Volcanology and Geothermal Research*, 153, 1-2, 64-79.

Jones J.P., Carniel R., Malone S.D., 2012, Decomposition, location, and persistence of seismic signals recovered from continuous tremor at Erta 'Ale, Ethiopia. *Journal of Volcanology and Geothermal Research*, 213-214, 116-129.

Lambert M.-A., Nguyen T. , Saenger E.H., Schmalholz S.M., 2011, Spectral analysis of ambient ground-motion—Noise reduction techniques and a methodology for mapping horizontal inhomogeneity, *Journal of Applied Geophysics*, 74, 2-3, 100-113

Lee D.D., Seung H.S., 1999, Learning the parts of objects by non-negative matrix factorization, *Nature*, 401, 788-791.

Mehmood A., Damarla T., Sabatier J., 2012, Separation of human and animal seismic signatures using non-negative matrix factorization, *Pattern Recognition Letters*, 33 16, 2085-2093.

Moreno H., 1998, Volcán Villarrica, Geología y peligro volcánico. Regiones IX y X 39°25' S, Servicio Nacional de Geología y Minería. Chile, 140 pp.

Ortiz R., Moreno H., García A., Fuentealba G., Astiz M., Peña P., Sánchez N., Tárraga, M. 2003, Villarrica Volcano (Chile): characteristics of the volcanic tremor and forecasting of small explosions by means of materials failure method. *J. Volcanol. Geotherm. Res.*, 128, 1-3, 247-59.

Schmidt M.N., Larsen J., Hsiao F.T., 2007, Wind noise reduction using non-negative sparse coding, in IEEE Workshop on Machine Learning for Signal Processing, 431-436.

Tárraga M., Carniel R., Ortiz R., García A., Moreno H., 2008, A dynamical analysis of the seismic activity of Villarrica volcano (Chile) during September-October 2000. *Chaos, Solitons and Fractals*, 37, 5, 1292-1299.

Volcano-sedimentary stratigraphy in the Valsequillo Basin, Central Mexico inferred from electrical resistivity soundings

Jaime Urrutia-Fucugauchi*, Alfonso Trigo-Huesca, Eloísa Téllez-García, Ligia Pérez-Cruz, Fabiola Méndez-Rivero and Valsequillo Project Team

Received: July 22, 2013; accepted: July 31, 2013; published on line: December 11, 2013

Resumen

La estratigrafía de la secuencia volcano-sedimentaria en la cuenca de Valsequillo, Puebla es investigada por medio de sondeos eléctricos de resistividad. Los depósitos en la cuenca preservan registros paleontológicos, paleoclimáticos y paleoambientales, que incluyen evidencias sobre restos fósiles de megafauna asociados con artefactos humanos. El reporte de posibles huellas de humanos preservadas en la tefra Xalnene, con una edad de alrededor de 38 mil años, ha atraído nuevamente interés en analizar la estratigrafía en Valsequillo. Este estudio se realizó en la zona cubierta por la tefra Xalnene, en la planicie situada al noroeste del volcán Toluquilla, empleando sondeos eléctricos verticales (SEVs). Los modelos de inversión de las curvas SEVs muestran una secuencia caracterizada por unidades de alta y baja resistividad aparente, que son asociadas a las tefras, sedimentos lacustres y fluviales y rocas volcánicas. Las secciones compuestas de resistividad documentan tres unidades, con las tefras y sedimentos formando una sección de unos 30 m sobre las rocas volcánicas. Los datos relacionan las tefras con el volcán monogenético, las cuales se emplazan en un ambiente lacustre somero. Las secciones de resistividad documentan las variaciones de espesores de los depósitos. Observaciones durante los estudios de campo y adquisición de datos proporcionan evidencias adicionales sobre el posible origen de las huellas aparentes, que estarían asociadas a las excavaciones de las tefras como materiales de construcción y los procesos de erosión. Estudios de detalle y experimentos en laboratorio proporcionarían mayor evidencia para entender la morfología y rasgos en las tefras. El retiro y actividades de corte están afectando significativamente al depósito por lo que se requieren de medidas de protección para proteger la zona dado su valor científico.

Palabras clave: Cuenca de Valsequillo, Tefra Xalnene, estratigrafía, estudio eléctrico de resistividad, sondeos eléctricos verticales, centro de México.

Abstract

Initial results of an electrical resistivity survey of the volcano-sedimentary sequence of the Valsequillo basin in central Mexico are presented. The volcano-sedimentary deposits preserve rich paleontological, paleoclimatic and paleoenvironmental records, which include extinct megafauna remains associated with human artifacts. The report of possible 38 ka old human footprint tracks in the Xalnene tuff attracted renewed interest in the basin stratigraphy. We examine the shallow stratigraphic sequence in the Xalnene tuff outcrop plain northwest of Cerro Toluquilla volcano using vertical resistivity soundings (VES). Inversion models of VES soundings show a layered structure of high and low resistivity units, which characterize the Xalnene tuff, lacustrine and fluvial sediments and volcanic rocks. 2-D resistivity cross sections document three major units corresponding to the Xalnene tuff and sediments filling a <30 m deep basin lying on volcanic rocks. Resistivity models provide further support for the association of Xalnene tuff with the Toluquilla volcano and emplacement of the pyroclastic deposits on a shallow lacustrine environment. The resistivity cross sections constrain the thickness of the tuff layers and underlying lacustrine sediments. Observations during the data acquisition field work provide insight on the possible origin of the apparent tracks, which seem to develop from erosion processes acting on quarrying marks. Further analysis and experimental evidence is required to understand the morphology and weathered patterns. The tuff layers are being removed by quarrying operations and the outcrops significantly altered. Adequate conservation measurements should be implemented to preserve the deposits for scientific research.

Key words: Valsequillo basin, Xalnene tuff, stratigraphy, electrical resistivity survey, vertical resistivity soundings, central Mexico.

J. Urrutia-Fucugauchi*
A. Trigo-Huesca
E. Téllez-García
L. Pérez-Cruz
F. Méndez-Rivero
and Valsequillo Project Team
Laboratorio de Paleomagnetismo y Paleoambientes,
Instituto de Geofísica
Universidad Nacional Autónoma de México
Ciudad Universitaria
Delegación Coyoacán, 04510
México D.F., México
*Corresponding author: juf@geofisica.unam.mx

Introduction

Finding of apparent human footprint tracks in the Xalnene tuff in the Valsequillo basin, central Mexico sparked renewed interest on the basin volcano-sedimentary sequences (González *et al.*, 2006a,b). The possible footprint tracks are preserved in an indurate ash layer associated with Cerro Toluquilla monogenetic volcano (Figure 1). The tuff was dated at 38 ka using optical stimulated luminescence (OSL). The implications for an early presence of humans in the Americas (Goebel *et al.*, 2008; Urrutia-Odabachian and Urrutia-Fucugauchi, 2011) promptly attracted further studies on the nature of the tracks, age of eruption and stratigraphy of the volcano-sedimentary deposits. Renne *et al.* (2005) reported Ar/Ar dates of 1.3 Ma, challenging the interpretation as possible human footprint tracks. Further radiometric and magnetostratigraphic studies were conducted, which have supported an old age for the Xalnene tuff (Feinberg *et al.*, 2009). Re-analyses of the tracks have questioned an origin as human tracks (Morse *et al.*, 2010). The studies have highlighted the interest in the volcano-sedimentary sequences in the Valsequillo basin. Here we present the initial results of a geophysical study of the basin, with the inversion models from electrical resistivity soundings of the lacustrine, fluvial and volcanoclastic deposits in the Xalnene tuff outcrop plain (Figure 1).

Electrical resistivity soundings appear well suited for shallow stratigraphic investigations of the volcano-sedimentary deposits, with vertical resistivity contrasts associated with the different lithologies and fluids in stratified deposits. Electrical resistivity surveys have been applied to geohydrology, geological mapping, geotechnical and archaeological prospecting and mineral deposits exploration (e.g., Keller and Frischknecht, 1966; Roy and Apparao, 1971; Zhdanov and Keller, 1994; Urrutia-Fucugauchi, 1992; Loke and Barker, 1996a,b; Marin *et al.*, 1998). Vertical electrical resistivity soundings (VES) have been used to investigate the underground structure and stratigraphy of sedimentary sequences in different geologic settings.

The Valsequillo volcano-sedimentary sequences have long been investigated because of the rich paleontological and archaeological remains (e.g., Malde, 1968; Szabo *et al.*, 1969; Steen-McIntyre *et al.*, 1981; González *et al.*, 2006a). Studies conducted in the 1960's as part of a joint project between Harvard University and University of Puebla documented evidence for extinct megafauna remains associated with human artifacts. Reconnaissance field surveys and excavations reported occurrence of fossil remains of mammoth, mastodon, camel, horse, four-horned antelope, saber-toothed tiger, and dire wolf in five different localities, mainly in the Tetela peninsula of the Valsequillo dam

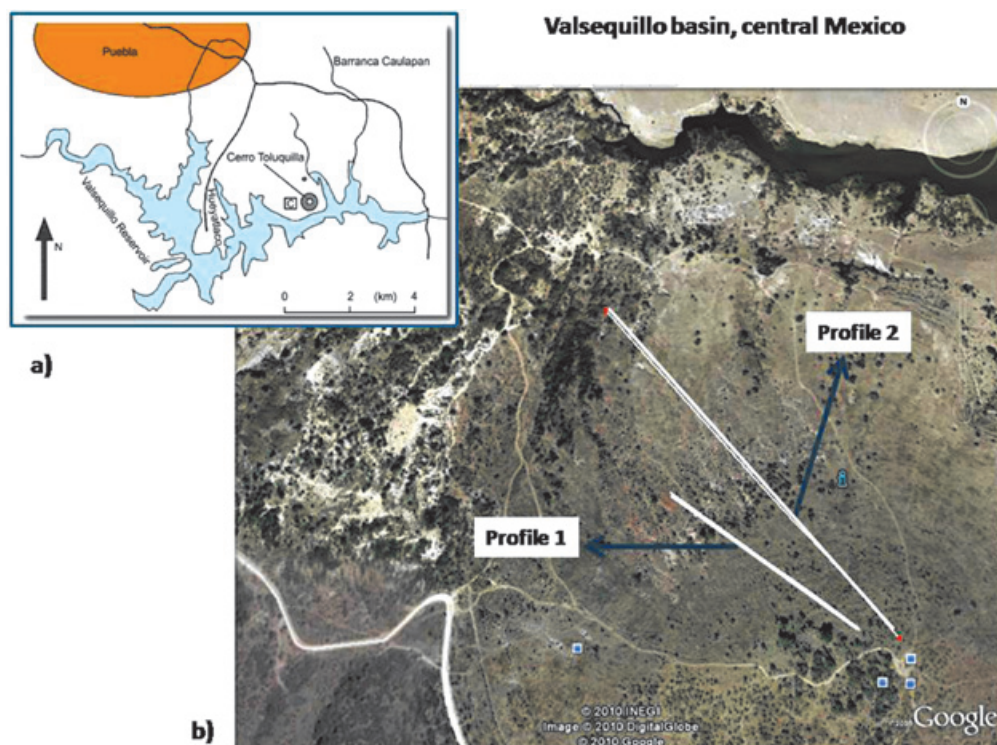


Figure 1. Valsequillo basin study area, central Mexico. (a) Schematic map of the Valsequillo dam reservoir. Study area is in the northern sector (González *et al.*, 2006a). (b) Location of resistivity profiles in the Xalnene outcrop plain (base map is a Google Landsat satellite image).

reservoir. Along the shores of the Valsequillo dam, built in 1944, fluvial, lacustrine, tephra and volcanoclastic deposits are exposed, with fossil remains recovered from the Valsequillo gravels.

Xalnene Tuff and Toluquilla volcano

González *et al.* (2006a) reported an emplacement age for the Xalnene tuff of 38.04 ± 8.57 ka based on OSL dating, which lead to the proposal that humans were present in central Mexico by around 40 ka ago. This interpretation was challenged by Renne *et al.* (2005) based on Ar/Ar dates on the basaltic lapilli retrieved from the tuff, with a mean age of 1.30 ± 0.03 Ma. Renne *et al.* (2005) also presented paleomagnetic evidence, with reverse paleomagnetic directions for the Xalnene tuff, which were correlated to the Matuyama C1r.2r chron. González *et al.* (2006a, b) argued that the lapilli in the tuff could be reworked or inherited, resulting in heterogeneous material not suitable for dating. They also suggested that the paleomagnetic record could result from self-reversal phenomena or related to the Laschamp subchron in agreement with the 40 ka age. Gogichaishvili *et al.* (2007) reported intermediate directions for the Xalnene tuff and low paleointensities for Cerro Toluquilla lavas, interpreted in terms of the Laschamp subchron.

Feinberg *et al.* (2009) reported additional paleomagnetic data from lava samples of Cerro Toluquilla volcano and from individual lapilli grains

in the Xalnene tuff, which yield reverse directions. They conclude that the Xalnene tuff has not been disturbed since emplacement by re-working associated with wave action in the lake shore. Feinberg *et al.* (2009) also report additional Ar/Ar dates for Toluquilla lavas, with a mean age of 1.29 ± 0.02 Ma, supporting the date for the Xalnene tuff. The nature of the fossil evidence, age dating and stratigraphy are being examined using different methods and approaches (e.g., Renne *et al.*, 2005, González *et al.*, 2006a,b; Duller, 2006; Gogichaishvili *et al.*, 2007; Feinberg *et al.*, 2009; Urrutia Fucugauchi *et al.*, 2012).

Electrical Resistivity Survey

The shallow stratigraphy underlying the Xalnene ash deposits was investigated using vertical electrical resistivity soundings along two profiles in the tuff outcrop in the area with the apparent human and animal footprint tracks (Figure 1). Survey area is located northwest of Toluquilla volcano and north of the Valsequillo reservoir.

The local basement for the volcano-sedimentary sequences is the Balsas Group (Figure 2b), which is a continental red bed sequence that is widespread in central and southern Mexico. Age of the Balsas Group ranges from Late Cretaceous to Eocene. González *et al.* (2006a) summarized the stratigraphy, with older deposits in the eastern sector, east of the Barranca Calpulapan are the Zacachimalpa or Calpulapan tuffs and lake sediments and the Ixcalo lavas. The lower

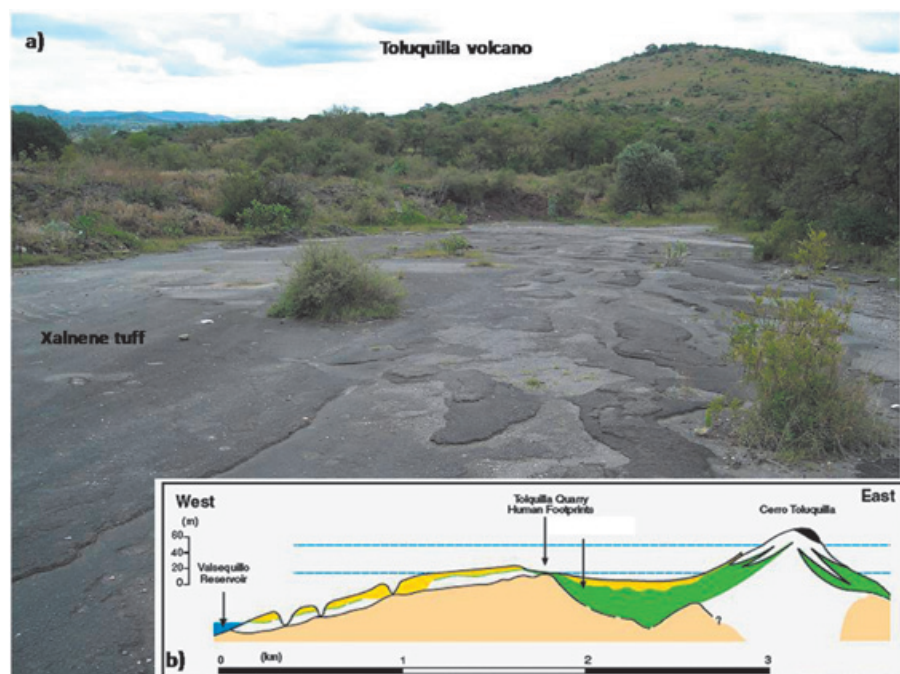


Figure 2. Cerro Toluquilla volcano and Xalnene tuff. View of Cerro Toluquilla volcano from the Xalnene quarry. (b) Cross section showing subsurface stratigraphy (González *et al.*, 2006a).

local lacustrine sequence then lies above the Ixcalo lavas or in the study area appears directly on top of the Balsas red beds. The Xalnene tuff serves as a local marker to separate the lacustrine sequence into a lower and upper sequence. Lahar deposits are interbedded within the lacustrine sediments. The fossil-bearing Valsequillo gravels and colluviums deposits correlate with the upper lacustrine sequence and are then above the Xalnene tuff.

The Xalnene quarry is characterized by an extended outcrop of the tuff that covers the surface (Figure 1). In the outcrop the tuff is flat-lying and formed by a succession several meters thick of multiple graded tuff layers of coarse lapilli interbedded with fine ash. The Xalnene tuff has been described in González *et al.* (2006 a, b) and Feinberg *et al.* (2009) and studies cited therein. The Xalnene tuff is a moderately indurate olivine basalt lapilli tuff deposited from eruption of Cerro Toluquilla.

The electrical resistivity survey was carried out using vertical resistivity soundings with the Schlumberger electrode configuration. The instrument used is a Siscal resistivity meter

equipped with a portable electronic acquisition unit. VES profiles are oriented along the long dimension in the Xalnene tuff outcrop, to permit the larger electrode apertures. The profiles were oriented towards the slope of Toluquilla volcano (Figures 1b and 2a), with current electrode apertures up to 30 and 40 m.

Resistivity VES profile curves show a marked change in shape approaching the volcano slopes, indicating low to high resistivities, suggesting a change in subsurface structure. The VES soundings are quantitatively modeled using inversion procedures described in Edwards (1977) and Locke and Barker (1996a, b). VES data inversions are carried out using the RES2DINV GISCO software version 3.2 and IPI2WIN software version 3.01 (Edwards, 1977; Shevlin and Modin, 2003). The inversion assumes horizontal stratified layers with vertical resistivity contrasts. Inversion models permit to estimate the thickness of the layers and resistivity values. Three to five layer models are used in the inversion procedure. Examples of VES curves showing the different curve types and inversion models are shown in Figure 3.

Vertical resistivity soundings (VES) over the Xalnene tuff

Apparent resistivity curves and inversion models

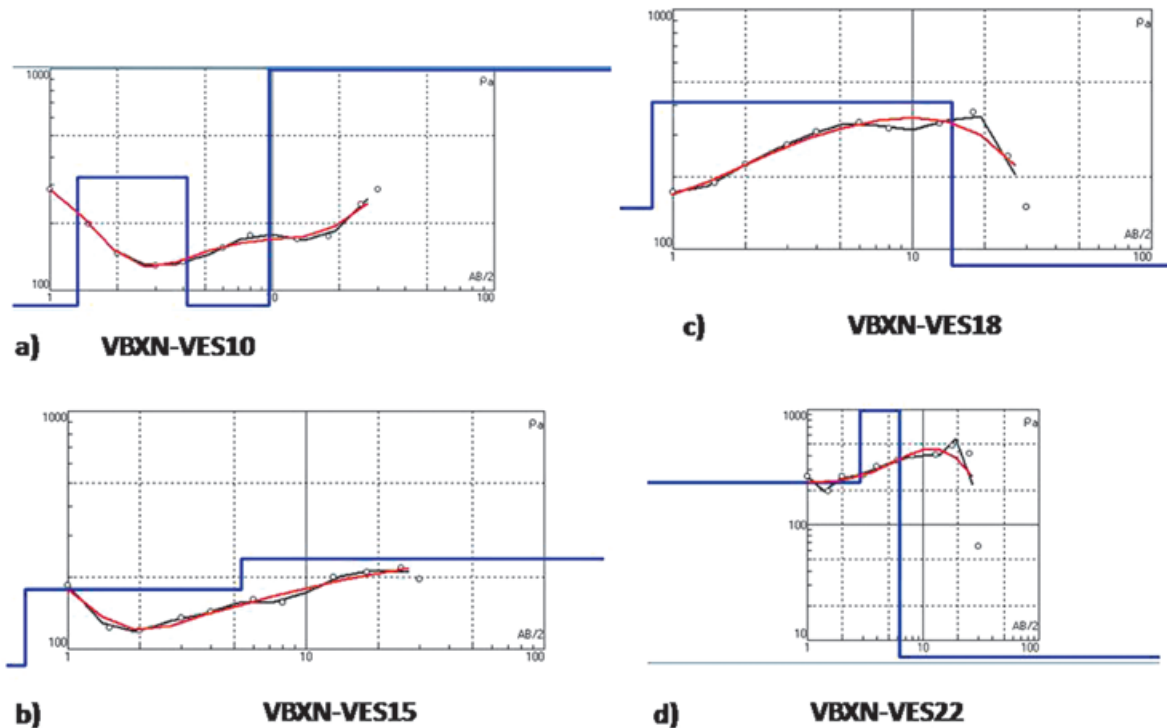


Figure 3. Representative examples of vertical electrical soundings (VES) in Xalnene tuff plain. The inversion models are included in the blue lines.

Resistivity cross sections are constructed from the SEVs (Figure 4). Cross sections show occurrence of a high resistivity zone which is associated with volcanic rocks from the Toluquilla volcano. The volcanic rocks form the basement to the lacustrine and fluvial deposits, represented by lower resistivity contrasts. The zone of low resistivities is associated with the Lower lacustrine sequence, with a thickness up to ~25-30 m. The lacustrine sequence gets thinner towards the Toluquilla volcano (Figure 4). The Xalnene tuff is characterized by intermediate resistivities. Intermediate resistivities may indicate ash and pyroclastic layers, although this is not well constrained in the models.

Discussion

The vertical electrical resistivity soundings assist in reconstructing the lake basin topography and the construction of Cerro Toluquilla volcano. The electrical resistivity cross sections provide indications on the lacustrine sequences and the pyroclastic flows and Xalnene tuff.

Eruption of Toluquilla volcano probably started underwater in the former lake, with eventual rising of a subaerial cone above the water level and emplacement of lava flows. The Xalnene tuff was probably emplaced as subaqueous density flows and subaerial base surges. In the quarrying trenches and pits, individual tuff layers visible by alternations of thin ash layers are between 1 and 10 cm thick. Ash layers contain baked, orange, sandy-silty, angular fragments derived from the lower lake sediments (González *et al.*, 2006a, b). The lake sediments above the Xalnene tuff display evidence of shallow water re-working possibly due to lake level changes. Presence of palagonite surfaces suggests hot ash emplacement in water.

The resistivity cross sections constrain the thickness of the tuff layers and underlying lacustrine sediments. Inversion models of VES soundings show a layered structure of high and low resistivity units, which characterize the Xalnene tuff, lacustrine and fluvial sediments and volcanic rocks. 2-D resistivity cross sections document three major units corresponding to the Xalnene

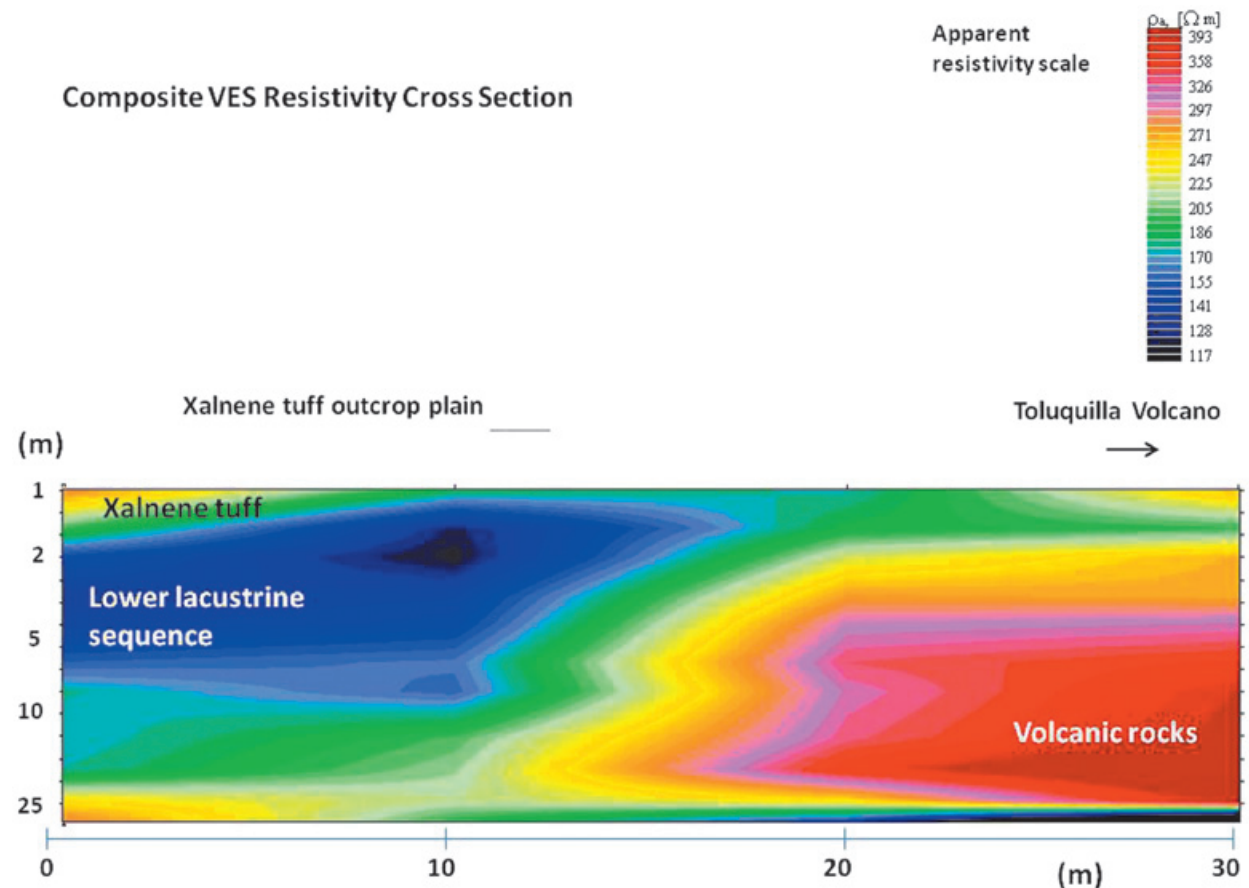


Figure 4. Resistivity cross section in the Xalnene tuff plain. Note that the vertical depth scales in the resistivity cross sections are not linear.

tuff and sediments filling a <30 m deep basin lying on the volcanic flows from the Toluquilla volcano (Figure 4). Resistivity models link the Xalnene tuff and underlying volcanic rocks with the Toluquilla volcano. González *et al.* (2006a) estimated a thickness for the Xalnene tuff of about 5.4 m close to Cerro Toluquilla and thinning down to 10 cm some 4 km to the northwest. The resistivity cross sections image the lower lacustrine unit and the pyroclastic deposits, deposited in a shallow lacustrine environment. González *et al.* (2006a, b) suggested that if ash layers are interbedded with the lacustrine sediments, then lacustrine sedimentation alternated with volcanic activity episodes. The resistivity cross sections do not permit to resolve alternations of ash and lacustrine sediments (Figure 4).

The Xalnene tuff is being quarried for construction and ornamental material (Figure 5). The tuff layers are being removed by quarrying operations and the outcrops significantly altered

(Figure 5b, c). Taking into consideration the rich paleontological and paleoenvironmental record preserved in the volcano-sedimentary deposits, it is proposed that adequate conservation measurements should be implemented. It is proposed that the Valsequillo basin should be granted status of a national geological heritage park.

Morse *et al.* (2010) reported a re-examination of the apparent footprint tracks, and compared the observations with other footprint-bearing sites. They concluded that the footprint tracks in the Xalnene tuff are not consistent with the morphology and characteristics of known tracks and are of questionable origin, suggesting that the marks in the tuff originated from the quarrying activities. Quarrying been carried out using manual and machine methods, using hand picks and a mechanical excavator. From our observations during the data acquisition field work, we consider the proposal by Morse *et al.*

Xalnene tuff quarry plain



Figure 5. Views of the Xalnene tuff. (a) View of the quarry zone investigated by the resistivity soundings. (b, c) Views of the quarry operations, showing the trenches and the slabs cut from the ash layers. (d) View of marks left from quarry operations, modified by erosion. (a) View of marks produced by the mechanical excavator, partly eroded. The incision pattern with parallel grooves can be observed.

(2010) a likely explanation. The apparent tracks seem to develop from erosion processes acting on quarrying marks. The mechanical excavator produces deep incisions (Figure 5d), which are eroded and modified. The extraction involves excavating trenches and is directed to cutting slabs (Figure 5b, c), which results in an apparent regular pattern, plus the waste material and gaps in between trenches. The surface layer is altered and eroded and linear features and other marks left by the quarrying activities might be modified into intermittent marks. However, isolated marks and linear incisions can be observed at various parts of the surface. A clear pattern for the modification process is not apparent and further analyses and experimental evidence are needed. Experiments may help understanding the morphology and weathered patterns.

Acknowledgments

This study forms part of the Valsequillo Basin geophysics project. We thank team members participating in the study A. Ortega, E. Torres, D. Lopez, J. Mayo and R. Zamora.

Bibliography

- Duller G.A.T., 2006, Comment on "Human footprints in central Mexico older than 40,000 years". *Quaternary Science Reviews*, 25, 3074-3076.
- Edwards L.S., 1977. A modified pseudosection for resistivity and induced-polarization. *Geophysics*, 42, 1020-1036.
- Feinberg J.M., Renne P.R., Arroyo-Cabrales J., Waters M.R., Ochoa-Castillo P., Perez-Campa M., 2009, Age constraints on alleged "footprints" preserved in the Xalnene tuff near Puebla, Mexico. *Geology*, 37, 267-270.
- Goebel F.E., Waters M.R., O'Rourke D.H., 2008, The Late Pleistocene dispersal of modern humans in the Americas. *Science*, 319, 1497-1502.
- Gogichaishvili A., Martin del Pozzo A.L., Urrutia Fucugauchi J., Soler A.M., 2007, Human footprints found in central Mexico could be at least 40,000 years old. *Geofísica Internacional*, 46, 85-87.
- González S., Huddart D., Bennett M.R., González-Huesca A., 2006 a, Human footprints in central Mexico older than 40,000 years. *Quaternary Science Reviews*, 25, 201-222.
- González S., Huddart D., Bennett M.R., 2006b, Valsequillo Pleistocene archaeology and dating: Ongoing controversy in Central Mexico. *World Archaeology*, 38, 611-627.
- Keller G.V., Frischknecht F.C., 1966, *Electrical Methods in Geophysical Prospecting*. Pergamon Press, Oxford, 519 pp.
- Loke M.H., Barker R.D., 1996a, Rapid least-squares inversion of apparent resistivity pseudosections using a quasi-Newton method. *Geophys. Prosp.*, 44, 131-152.
- Loke M.H., Barker R.D., 1996b, Practical techniques for 3D resistivity surveys and data inversion. *Geophys. Prosp.*, 44, 499-523.
- Marin L., Steinich B., Jaglowski D., Barcelona M.J., 1998, Hydrologic site characterization using azimuthal resistivity surveys. *J. Environ. Eng. Geophys.*, 3, 179-184.
- Morse S.A., Bennett M., González S., Hudart D., 2010, Techniques for verifying human footprints: reappraisal of pre-Clovis footprints in Central Mexico. *Quaternary Science Reviews*, 29, 2571-2578.
- Renne P.R., Feinberg J.M., Waters M.R., Arroyo-Cabrales J., Ochoa-Castillo P., Perez-Campa M., Knight K.B., 2005, Age of the Xalnene ash, Central Mexico, and archaeological implications. *Nature*, 438, E7-E8.
- Roy A., Apparao A., 1971, Depth of investigation in direct current methods. *Geophysics*, 36, 943-959.
- Shevnin V.A., Modin I.N., 2003, IPI2WIN (3.0.1) Free Version, [1D interpretation of VES profile], Moscow State University, Geological Faculty, Department of Geophysics: GEOSCAN-M Ltd.
- Steen-McIntyre V., Fryxell R., Malde H.E., 1981, Geologic evidence for age of deposits at Huayatlaco archaeological site, Valsequillo, Mexico. *Quaternary Research*, 16, 1-17.
- Szabo B.J., Malde H.E., Irwin-Williams C., 1969, Dilemma posed by uranium-series dates on archaeologically significant bones from Valsequillo, Puebla, Mexico. *Earth Planetary Science Letters*, 6, 237-244.
- Urrutia-Fucugauchi J., 1992, Reconnaissance electrical resistivity and self-potential studies of the Atotonilco-Jonacatepec region, Morelos State, Mexico. *Geofísica Internacional*, 31, 341-358.
- Urrutia-Fucugauchi J., Trigo-Huesca A., Pérez-Cruz L., 2012, Magnetic links among lava flows, tuffs and the underground plumbing system in a monogenetic volcano, derived from magnetics and paleomagnetic studies. *Phys. Earth Planet. Int.*, 212-213, 10-18.

Urrutia-Odabachian A., Urrutia-Fucugauchi J., 2011, El poblamiento temprano de América: ¿cómo, cuándo, dónde, quiénes?. In: Escenarios de cambio climático: Registros del Cuaternario en América Latina, Universidad Nacional Autónoma de México, México, v. I, p. 9-28.

Van Landingham S.L., 2006, Diatom evidence for autochthonous artifact deposition in the Valsequillo region, Puebla, Mexico during the Sangamonian (sensu lato = 80,000 to ca. 220,000 yr BP and Illinoian (220,000 to 430,000 yr BP)). *Journal Paleolimnology*, 36, 101-116.

Zhdanov M.S., Keller G.V., 1994, The Geoelectrical Methods in Geophysical Exploration, *Elsevier Sci. Publ.*, 873 pp.

A very special Fractal: Gingko of Jena

Peter G. Malischewsky

Received: September 23, 2013; accepted: October 03, 2013; published on line: December 11, 2013

Resumen

Después de una breve explicación sobre el significado de los fractales en las Ciencias de la Tierra, se presenta una modificación de la famosa iteración de Mandelbrot. El resultado tiene un cierto parecido con una hoja de gingko, el cual es una especie de árbol singular, no solo en la botánica sino en la cultura y la filosofía oriental. Se presentan algunas de las características inusuales del nuevo fractal "hoja de gingko".

Palabras clave: fractales en geofísica, conjunto de Mandelbrot, gingko biloba, iteración de la hoja gingko.

Abstract

After shortly explaining the significance of fractals in the geosciences I present a modification of the famous Mandelbrot iteration. The result bears a certain resemblance to a gingko leaf. The gingko tree is special in botany, in cultural history and in philosophy. Some unusual features of the new gingko-leaf fractal are presented.

Key words: fractals in geophysics, Mandelbrot set, gingko biloba, gingko leaf iteration.

P.G. Malischewsky
Friedrich-Schiller-Universität Jena
Institut für Geowissenschaften
Burgweg 11
D-07749 Jena, Germany
Corresponding author: p.mali@uni-jena.de

Introduction

This special article out of competition does not directly concern geophysics but indirectly by presenting a special new fractal (the ginkgo-leaf fractal) and beyond that by enabling the view on beauty of science and connections to philosophy, art, and nature.

It is well-known that fractals surround us everywhere [see e. g. Mandelbrot (1977) and Barnsley (1988)]. The concept of fractals was introduced into science by Mandelbrot (1967) in a geological context. Later it became more and more evident that fractals are very important for geophysics and geology. That is small wonder because following Scholz and Mandelbrot (1989) one possible broad explanation of the role of fractals in geophysics may be found in probabilistic limit theorems, and in the existence of classical "universality classes" related to them. A second possible explanation may come from deterministic chaotic dynamics. Additionally, Turcotte (1989) pointed out that scale invariance has long been recognized as an important feature of many geological problems. A fractal distribution is the only distribution that is scale invariant. Thus it is not surprising that many geological and geophysical data sets are fractals. In this context, fractals are a method of empirically correlating a variety of quantitative observations. But in addition to being appropriate for empirical correlations fractals also result from several classes of theoretical studies. Dimri has devoted the first chapter of his book [Dimri (2005)] the fractals in geophysics and seismology. The applications in seismology range from the size-frequency distribution of earthquakes, Omori's law and the analysis of aftershock data even up to the forecasting of tsunami. For completeness, we cite here also two articles which analyse the fractal geometry and seismicity in the Mexican subduction zone [Angulo-Brown *et al.* (1998)] and fracture arrays in Baja California Sur, Mexico, by using fractal analysis [Nieto-Samaniego *et al.* (2005)].

One of the most prominent fractals is without doubt the Mandelbrot set. After Taylor and Spratt (2008) Mandelbrot saw this set for the first time at 1 March 1980. It must have been an indescribably great feeling to see that whole cosmos of wonderful and unimaginably fragile structures. The author of the present article was also surprised in suddenly seeing the ginkgo-leaf fractal (see Figure 2) for the first time about 25 years ago. It has not those fine ramifications and complexity of the Mandelbrot set which is following Dewdney (1985) "the most complex object in mathematics". But the ginkgo-leaf set is complex enough and has its own specialities and beauties as we will see later. We start with a short description of the ginkgo tree's prominence.

The ginkgo tree

It is well known that the ginkgo tree (*Ginkgo biloba*) is a "living fossil" because of its special botanic history. It is a medical plant with botanical and historico-cultural significance. The German curatorship "Baum des Jahres" (tree of the year) has declared it as the "tree of the millennium". It is a great symbol for our world, a tree of the world and a symbol of strength and hope. The far eastern philosophy considers the tree, among other things because of its splited leaves, as an incarnation of the famous Ying-Yang principle and connected with that it is also considered as a symbol for harmony and fertility. Last but not least the people are fascinated from the special beauty of the leaves. Nobody less than Johann Wolfgang von Goethe (1749-1832) was also fascinated from this tree and its leaves and initiated the growing of a ginkgo in the botanical garden in Jena, which is now the oldest ginkgo tree in Thuringia. He even wrote a poem "Gingo Biloba" [Goethe (1819)] which he devoted to his muse Marianne von Willemer (1784-1860) (see Figure 1) and whose rough English translation is (see en.wikipedia.org/wiki/Ginkgo_biloba):

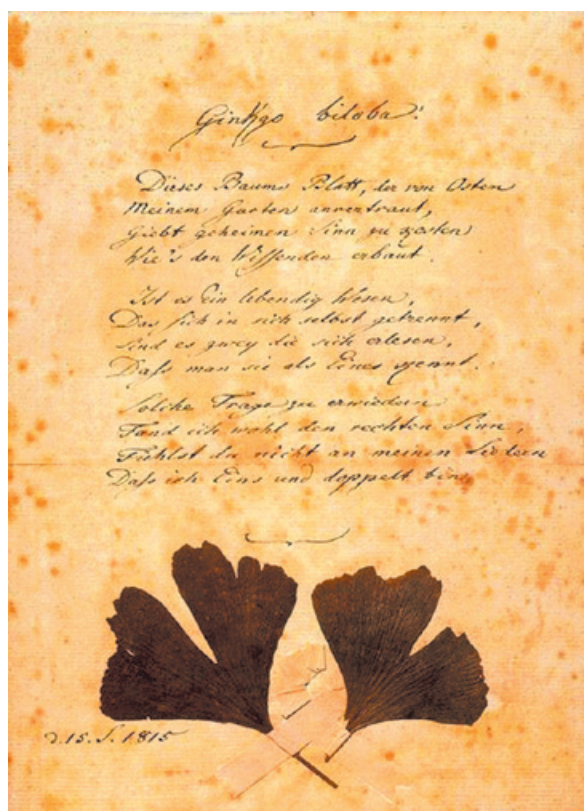


Figure 1. Facsimile of Goethe's poem Gingo biloba devoted to M. v. Willemer.

Gingo Biloba

*This leaf from a tree in the East,
Has been given to my garden.
It reveals a certain secret,
Which pleases me and thoughtful people.
Is it a living being,
Which has separated in itself?
Or are these two, who chose
To be recognized as one?
Answering this kind of question,
Haven't I found the proper meaning,
Don't you feel in my songs,
That I'm one and double?*

The Mandelbrot and the gingo-leaf iteration

It is well-known that the Mandelbrot set consists of all points $c = a + ib \triangleq (a, b)$ of the complex plane for which the quadratic recurrence equation

$$z_{n+1} = z_n^2 + c, z_0 = 0, \quad (1)$$

does not tend to infinity, i. e. $\forall n, n > 0, z_n \neq \infty$. It can be also written in real notation with $z = x + iy$:

$$\begin{aligned} x_{n+1} &= x_n^2 - y_n^2 + a, \\ y_{n+1} &= 2x_n y_n + b. \end{aligned} \quad (2)$$

There are a lot of generalizations of (1), e. g. with higher polynomials instead of (1) or with bicomplex numbers in order to produce Mandelbrot sets in dimensions three and four [Rochon (2000)] among many others. All these generalizations do not create the elementary beauty of the original Mandelbrot set, the so-called apple-man.

We apply now another special generalization of (1) which leads to a structure which can be considered as a stylized gingo leaf (see Figure 2). It is defined as follows:

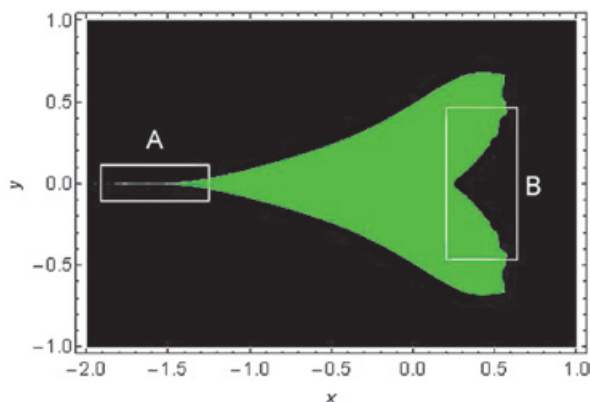


Figure 2. Gingo-leaf set with indication of 2 regions A and B of interest.

$$\begin{aligned} z_{n+1} &= \frac{1}{2} (z_n^2 + z_n^{*2}) + \frac{1}{4} (z_n^2 - z_n^{*2}) (z_n + z_n^*) \\ &+ c, z_0 = 0, \end{aligned} \quad (3)$$

where the star means complex conjugation. We call it **gingko-leaf iteration**. It is a polynomial of third order in z_n and z_n^* . However, the cubic terms in x_n and y_n cancel. By using the real notation we see immediately what is going on here in contrast to (2):

$$\begin{aligned} x_{n+1} &= x_n^2 - y_n^2 + a, \\ y_{n+1} &= 2x_n y_n + b. \end{aligned} \quad (4)$$

That means, the only third order term is the mixed term $x_n^2 y_n$.

A visualization of the Mandelbrot set together with the new gingo-leaf set is presented in Figure 3. It shows the approximate border strip of the apple-man together with the gingo leaf. Figure 3 was calculated with Mathematica and for the reader's convenience we present here the main features of the program without explanation:

```
CompiledMandel = Compile[{{c, _Complex}},
Length[FixedPointList[#^2+c
&,c,25,
SameTest->(Abs[#2]>2.0&)]];
CompiledGingko = Compile[{{c, _Complex}},
Length[FixedPointList[#^2
+Im[#^2]*(Re[#]-1)*I+c&,
c, 25, SameTest -> (Abs[#2] >
2.0&)]];
g = DensityPlot[compiledGingko[x + I y], {x, -2, 0.6}, {y,
-1.3, 1.3}, PlotPoints -> 500,
Mesh -> False, Frame -> False, AspectRatio ->
Automatic,
ColorFunction -> (If[# = 1, RGBColor[0.3, 0.7, 0],
RGBColor[1, 1, 1]] &)];
c = ContourPlot[compiledMandel[x + I y], {x, -2, 0.6}, {y,
-1.3, 1.3}, PlotPoints -> 300,
Frame -> False, AspectRatio -> Automatic,
ContourShading ->False,
Contours -> {13}];
Show[g, c]
```

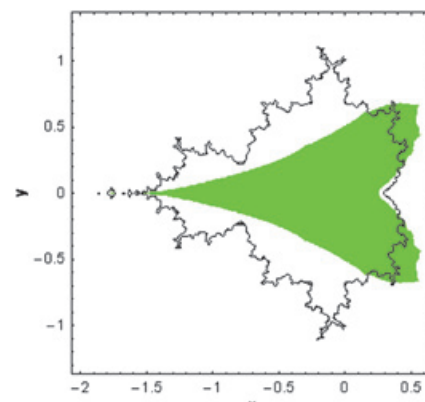


Figure 3. The gingo-leaf set together with the contour of the Mandelbrot set.

Obviously, the gingko-leaf set is symmetric concerning the x -axis. The proof for that behaviour is simple and is omitted here. It can be carried out similarly as for the Mandelbrot set.

Some features of the gingko-leaf set

The Mandelbrot set has a rich structure at its border line and also in the outer regions not belonging to the set. The latter structure can be visualized by using so-called velocity diagrams, where the number of iterations necessary for exceeding a given limit is colour-coded [see e. g. Peitgen and Richter (1986)]. The same is true for the gingko-leaf set especially within the regions A and B of Figure 2 and we present some examples. A very convenient and effective vehicle for visualizing these structures is the "Fractalizer" of Sontheimer (2007), which was used for painting Figures 6-9. Additionally we have investigated also the inner region of the set (Figure 4) with Turbo Pascal by using the following colour-code, where $t = x_n^2 + y_n^2$:

$t > 4$	→ black
$3 < t < 4$	→ light green
$2 < t < 3$	→ dark grey
$1 < t < 2$	→ crimson
$0.4 < t < 1$	→ leaf green
$0.155 < t < 0.4$	→ crimson
$0.1 < t < 0.155$	→ light yellow
$0.05 < t < 0.1$	→ light brown
$0.008 < t < 0.05$	→ dark crimson

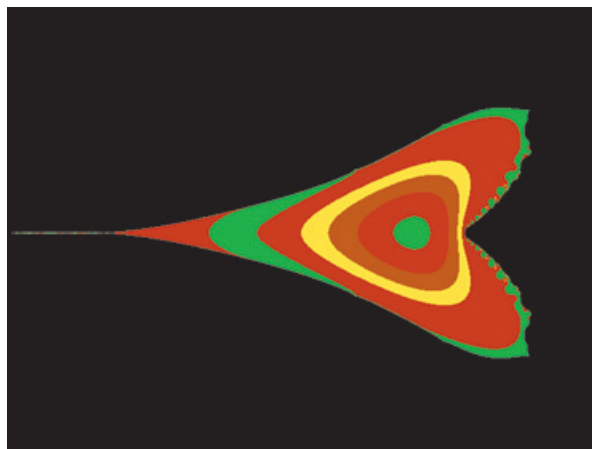


Figure 4. Inner structure of the gingko-leaf set

It could be carried out with Mathematica as well by using e. g. the RasterArray command.

The stalk (region A) is characterized by the occurrence of so-called satellites which are typical for the antenna of the Mandelbrot set and which have now the form of stylized gingko leaves in the broadest sense (Figure 5).

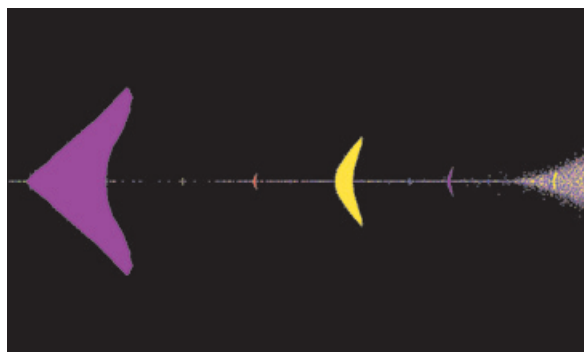


Figure 5. Colour-coded range $a \in [-1.8, -1.5]$, $b \in [-0.01, 0.01]$ within region A with Turbo Pascal.

The colour-code for Figure 5 is:

$t > 4$	→ black
$3 < t < 4$	→ light green
$2 < t < 3$	→ pink
$1 < t < 2$	→ violet
$0.4 < t < 1$	→ light blue
$0.1 < t < 0.4$	→ light purple
$t < 0.1$	→ light yellow

The nodality in region A has also a nice structure which we demonstrate with the "landscape" in Figure 6. The black parts belong to the gingko-leaf set.

Very interesting and beautiful structures occur in region B nearby the sawtooth-like indentations at the right end of the gingko leaf. In Figure 7 we see a stylized winter rose (*Euphorbia pulcherrima*), whose origin is Mexico. It occurs in many places of region B.

Another winter rose from region B is presented in Figure 8. It is interesting to note that contrary to Figure 7 we find here parts of it which belong to the gingko-leaf set (in black).

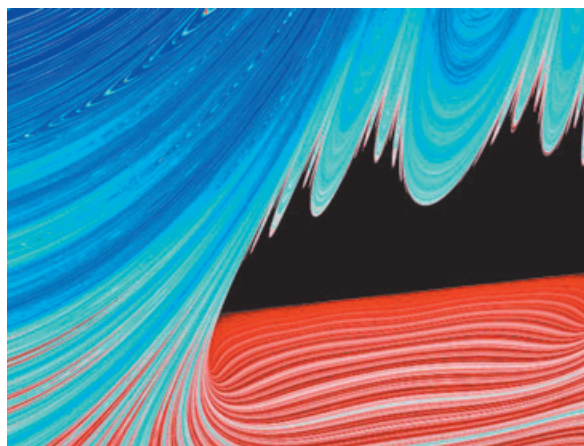


Figure 6. Color-coded range $a \in [-1.4366, -1.4360]$, $b \in [-0.0069, -0.0064]$ within region A.

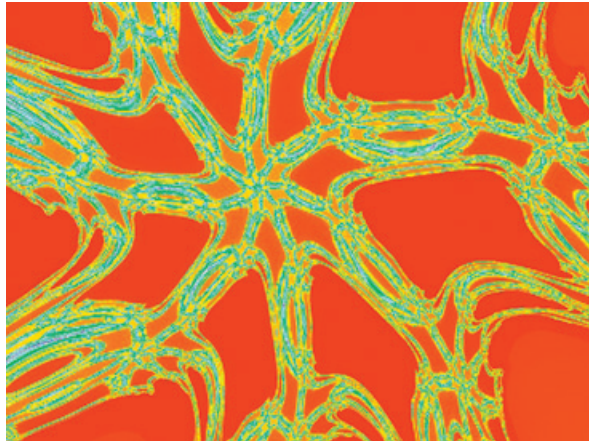


Figure 7. The winter rose in region B out of the gingko-leaf set with $a \in [0.4507, 0.4528]$, $b \in [-0.2148, 0.2132]$.



Figure 8. Winter rose in region B for $a \in [0.386232, 0.386246]$, $b \in [-0.135391, -0.135381]$; the black forms belong to the gingko-leaf set.

It remains unclear whether similar to the Mandelbrot set the isolated parts of the set are all connected with the main body by very thin fibres or not.

Miscellaneous

It is well-known [see e. g. Peitgen and Richter (1986)] that by changing the role of c and z in (1) we can assign each point of the complex plane a corresponding Julia set. The same is true for the gingko-leaf set. Especially for points from region A and B interesting figures are obtained. Without going into details we present two examples from region B in Figure 9.

I have called the left figure “throne of Cuauhtémoc” and the right figure “bad ghost”. Note that on both sides of the throne again winter roses occur.

Finally, let us demonstrate that by changing the gingko-leaf iteration only a little bit, we get a completely different set. By replacing (4) by

$$\begin{aligned} x_{n+1} &= x_n^2 - y_n^2 + a, \\ y_{n+1} &= 2x_n y_n + b. \end{aligned} \tag{5}$$

we obtain a set (Figure 10) which I call “ugly duckling”.

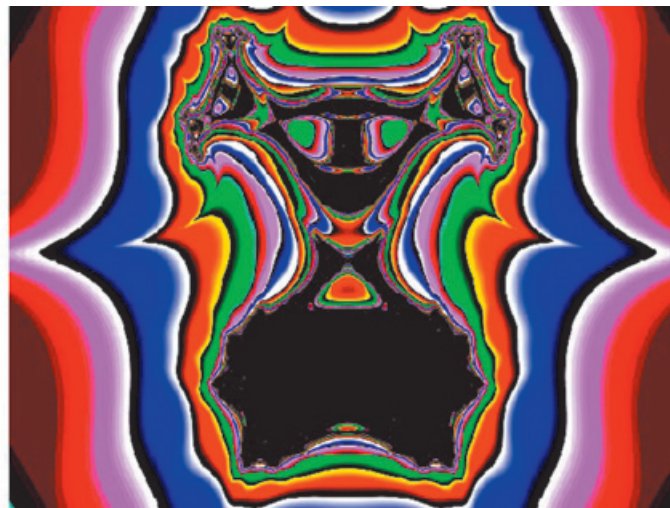
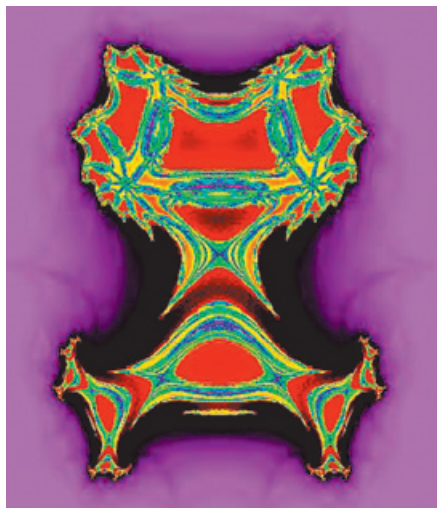


Figure 9. Left: “throne of Cuauhtémoc” is a Julia set from point $(0.4084, -0.1636)$; right: “bad ghost” is a Julia set from a point nearby.



Figure 10. Colour-coded inner structure of the set “ugly duckling” with Turbo Pascal.

Obviously, the symmetry concerning the x -axis is completely broken.

Conclusions

We have presented a less-known part of the enormously multiform world of fractals. It is not excluded, that the properties of the ginkgo-leaf set follow from already existing mathematical theorems about more general fractals. This might require closer examination. It is also not excluded that a similar kind of feedback mechanism, which produces the ginkgo-leaf fractal, is also responsible in the broadest sense for “producing” the nice ginkgo leaves in nature. At the same time a formal but pretty “connection” between the ginkgo and the Mexican winter rose is accomplished.

Hopefully, this article will attract attention of all people fascinated by the beauty of science.

Acknowledgements

A special word of thanks goes to Robert Sontheimer (Hohenstein/Germany) who modified his program Fractalizer for the investigation of the ginkgo-leaf set and carried out a lot of test calculations. Without his help this article would not have been possible in the present form.

I devote this article to the memory of my honoured former colleague Dr. Erhard Unterreitmeier (1939-1997), who encouraged me to publish the ginkgo fractal under the title “Ginkgo from Jena” already about 25 years ago. Additionally, I devote it to my mother Alice Malischewsky nee Auning (1903-1995), who followed my efforts about fractals with great interest.

Bibliography

- Angulo-Brown F., Ramírez-Guzmán A.H., Yépez E., Rudolf-Navarro A., Pavía-Miller C.G., 1998, Fractal geometry and seismicity in the Mexican subduction zone, *Geofísica Internacional*, 37, 29-33.
- Barnsley M.F., 1988, *Fractals everywhere*, Academic Press, San Diego.
- Dewdney K., 1985, Computer recreations, *Scientific American*, 250, 14-22.
- Dimri V.P., 2005, *Fractal Behaviour of the Earth System*, Springer, Berlin.
- Goethe J.W.v., 1819, *West-östlicher Divan*, Gothaische Buchhandlung, New edition by Deutscher Taschenbuchverlag, 2006, München.
- Mandelbrot B.B., 1967, How long is the coast of Britain? Statistical self-similarity and fractional dimension, *Science*, New Series, 156, 636-638.
- Mandelbrot B.B., 1977, *The fractal geometry of nature*, Freeman Company, New York.
- Nieto-Samaniego A.F., Alaniz-Alvarez S.A., Tolson G., Oleschko K., Korvin G., Xu S.S., Pérez-Venzor J.A., 2005, Spatial distribution, scaling and self-similar behavior of fracture arrays in the Los Planes Fault, Baja California Sur, Mexico, *Pure and Applied Geophysics*, 162, 805-826.
- Peitgen H.-O., Richter P.H., 1986, *The Beauty of Fractals*, Springer, Berlin.
- Rochon D., 2000, A generalized Mandelbrot set for bicomplex numbers, *Fractals*, 8, 355-368.
- Scholz C.H., Mandelbrot B.B., 1989, Introduction (special issue), *Pure and Applied Geophysics*, 131 (1-2), 1-4.
- Sontheimer R., 2007, www.fractalizer.de
- Taylor R.P., Sprott J.C., 2008, Biophilic fractals and the visual journey of organic screen-savers, *Nonlinear Dynamics and Life Sciences*, 12, 117-129.
- Turcotte D.L., 1989, A fractal approach to probabilistic seismic hazard assessment, *Tectonophysics*, 167, 171-177.